Stress-Transfer Modelling of Gold Systems at the Obuasi Gold Deposit, Ghana

CARDIFF UNIVERSITY
PRIFYSGOL CAERDYDD

A Thesis submitted to Cardiff University for the degree of Master of Philosophy

Angus Oliver Odling

School of Earth and Environmental Sciences

18th January 2022

Acknowledgements

Abstract

Coulomb stress transfer modelling has been applied to understand the dynamics of seismogenic hydrothermal mineral deposits and proposed as a tool for gold exploration. Spatial correlations between positive Coulomb stresses transferred by palaeoseismic sequences and gold resource distributions were interpreted to indicate that areas of elevated Coulomb stress promoted permeability-enhancing aftershock sequences. Despite a promising start, the technique has not been widely applied in exploration since the first studies almost two decades ago. This work further investigates the use of stress transfer modelling by applying it to a gold deposit with a complex structural and mineralisation history.

The supergiant Obuasi gold deposit (34Moz current resource) in Ghana experienced two stages of gold emplacement. In the first stage ($D2_{Ob}$), disseminated sulphide-hosted gold mineralization formed in large reverse fault and shear zones. The later $D5_{Ob}$ stage consisted of strike-slip faulting and reactivation of the $D2_{Ob}$ structures, emplacing predominantly free milling gold in low displacement fault-hosted quartz veins. Several stress transfer models of both stages with different levels of fault simplification were created to represent alternative approaches that a geologist might use as exploration matures. Correlation between positive Coulomb stresses induced during $D5_{Ob}$ and gold resources at Obuasi, which are focused on stepover structures and fault intersections, indicates that Coulomb stress-induced aftershocks could have exerted a control on mineralisation during $D5_{Ob}$. No link between positive Coulomb stresses and the gold distribution was found for $D2_{Ob}$. This stage may have involved the propagation of cyclical fault-valve behaviour along fault segments, and aftershocks did not control gold distribution. Post-$D2_{Ob}$ fault geometry modification may have made the geometry of this model not truly representative. To apply Coulomb stress transfer modelling successfully to complex multi-stage gold deposits, the mineralisation mechanism and fault geometry evolution must be constrained. For systems (typically strike-slip) where focused aftershock permeability controlled gold distribution, Coulomb modelling may be an effective tool for exploration. For mineralisation phases with different mechanisms, stress transfer modelling can provide insight into the fault dynamics but does not have a predictive capacity.

Table of Contents

List of Figures

List of Tables

Chapter 1.

Introduction

1.1 Background

Transient earthquake-driven processes have been established as important drivers in the formation of mineral deposits (Sibson 1987; Sibson 1996). Their study has significantly advanced understanding of fluid transport (Sibson 1981; Eisenlohr et al. 1989; Bosl and Nur 2002) and mineralisation distribution (Cox and Ruming 2004; Micklethwaite and Cox 2004; Micklethwaite and Cox 2006) and has yielded the stress transfer modelling technique that, when applied to deposits, has the potential to greatly inform exploration efforts. This thesis investigates the application of stress-transfer modelling at the Obuasi gold deposit as a method of predicting gold resource distribution.

Stress-transfer modelling (STM) involves the calculation of changes in Coulomb stress in rock mass surrounding a fault following a seismic event (King et al. 1994; Freed 2005). These calculations are then used to infer likely behaviour in rocks under the new stress conditions (Steacy et al. 2005a). Its application has been developing in contemporary earthquake research for over 20 years, principally to predict contemporary aftershock sequences as a means of hazard prediction and assessment (Toda et al. 2002; Lin and Stein 2004; Toda et al. 2005; Toda et al. 2008; Toda et al. 2011b; Toda et al. 2012; Mildon et al. 2016; Mildon et al. 2019; Hughes et al. 2020) or to investigate fault dynamics (Fagereng 2013; Hodge et al. 2018). The technique also enjoyed a period of favour within exploration geology following a number of publications in the mid-2000s (Cox and Ruming 2004; Micklethwaite and Cox 2004; Micklethwaite and Cox 2006), finding a strong correlation between the predicted distribution of stress-transfer induced aftershock sequences and gold in stepover zones at deposits in Western Australia. Following the publication of these papers, literature applying stress-transfer modelling in an exploration context has been limited and such as application to mining induced earthquakes (Kozłowska et al. 2015). This may be attributed to perceived limitations

in predictive capacity (Vearncombe and Zelic 2015), the wider usage of more comprehensive 3D numerical modelling (e.g. Potma et al. 2008) and a general lack of exposure to the technique within the professional exploration community.

However, Coulomb stress-transfer modelling may be exploration tool with underutilised potential. Key benefits of Coulomb STM are that with comparatively little training, time, and financial outlay, a geologist can produce clear graphical outputs that identify exploration targets at a given deposit rapidly and at a fraction of the cost of finite-element modelling. While more extensive modelling is invaluable when comprehensive models of fault systems are available, the question of why comparatively simple Coulomb modelling isn't an additional staple of the structural geologist's toolkit particularly in early exploration is unanswered. Here, this is investigated in the context of the supergiant Obuasi gold deposit, Ghana.

Seismic research has indicated since the mid 1960s (Chinnery 1963) that earthquakes induce changes in stress conditions not just at the tips of active faults, but also in the surrounding rock mass and on proximal faults. Later studies of contemporary off-fault aftershock sequences showed that aftershock distributions could be correlated with zones of increased shear (Das and Scholz 1981) and Coulomb (Stein and Lisowski 1983) stress calculated in surrounding rocks following an earthquake event. This became widely accepted within the seismological field following the publication of Stein (1999) in Nature. Earthquake activity driving gold deposition was postulated earlier, but was not linked to stress transfer (Sibson 1987; Sibson et al. 1988). In this literature, earthquakes were shown to be mechanisms which increase permeability, enabling gold-bearing fluid flux in areas where overpressured auriferous fluid is present at depth. Studying fault-hosted orogenic gold deposits, more recent research has proposed that many of the low-displacement faults and shear zones which host gold represent repeatedly activated aftershock structures, which could be modelled using stress-transfer techniques (Cox and Ruming 2004). Aftershock sequences form in association with larger crustal scale faults and shear zones, typical of orogenic gold deposits. Around this time, it had been established that aftershock sequence damage zones are much more favourable to fluid flow than simple mainshock locations with distributions of aftershocks linked to pore fluid pressure (Bosl and Nur 2002). The discovery of this

association formed the foundation of a new structural paradigm for the formation of orogenic gold deposits.

Cox and Ruming (2004) studied orogenic gold deposits in Western Australia and identified a link between contemporary seismic research and the processes which form orogenic gold deposits, a term which had been recently introduced, replacing the broader 'mesothermal' deposit type (Groves et al. 1998). Their research applied STM to fossilised fault systems, which established that ancient (>Ma-Ga BP) earthquake-aftershock sequences can be modelled using software designed for assessing contemporary seismic hazards. This gained traction following two further landmark papers (Micklethwaite and Cox 2004; Micklethwaite and Cox 2006). By modelling areas of elevated Coulomb stress, small increases in which can dramatically impact aftershock occurrence, the locations of mineralised small displacement faults can be linked to aftershock distributions using displacements on large, usually unmineralised, faults and shear zones. In this research, it was shown that mineralised Archean fault systems in the Yilgarn Craton exhibited excellent correlations with likely aftershock distributions as a result of mainshock events, particularly across underlapping fault stepovers. Finding this association with dilational jog structures, stress-transfer modelling reconnects with the earlier mineralising theories developed in the 1980s, which suggest that dilational jog structures are particularly favourable to gold mineralisation as a result of earthquake rupturing.

Since the mid 2000s and the establishment of the paradigm, some additional research into stress-transfer modelling in the context of gold mineralisation has been published, predominantly in continued study of stepovers in the Yilgarn Craton (Micklethwaite 2008; Micklethwaite et al. 2016) and an investigation of static-stress triggering of earthquakes in a South African gold mine (Kozłowska et al. 2015). Stress-transfer modelling in recent research literature has therefore diverged from resource-focused geology. This has been attributed to the modelling providing excellent understanding of local features and geometries but little in the way of a workable exploration model (Vearncombe and Zelic 2015). There may also be perceived difficulty in the application of stress-transfer modelling due to the 2D presentation of Coulomb stress-transfer results meaning that complex 3D

geometries are poorly represented, making precise ore shoot prediction effectively unachievable. Nevertheless, as an early aid to drill-site targeting, using Coulomb modelling has strengths, especially when used in conjunction with the modern exploration toolkit, as demonstrated in chapters 5 and 6.

This thesis demonstrates the application of STM for understanding the Paleoproterozoic Obuasi gold deposit of Ghana, owned and operated by AngloGold Ashanti. Gold at Obuasi is hosted in greenschist-facies metasediments (Junner 1932), which are favourable to brittle-ductile regime earthquake modelling, such as the modelling of Archean greenstone in the Yilgarn Craton (e.g. Micklethwaite and Cox 2004). The deposit underwent a multi-stage deformation history which is well constrained. The deposit is hosted in a system of well-mapped faults with indications of their kinematics, mostly available in published literature (Blenkinsop et al. 1994; Allibone et al. 2002; Perrouty 2012; Fougerouse et al. 2017; Oliver et al. 2020). Gold occurs in multiple forms, including a disseminated arsenopyrite-Au sulphide phase and notably as free gold in quartz veins (Fougerouse et al. 2017; Oliver et al. 2020), which are hosted in low displacement faults and fractures much like those first discussed as aftershock-activated features in the late '90s. From a kinematic perspective the deposit is comparable to studied systems from the Yilgarn, such as the St. Ives and Boulder-Lefroy faults, which were the basis for the prominent Coulomb stress-transfer modelling studies in the 2000s (Cox and Ruming 2004; Micklethwaite and Cox 2004; Micklethwaite and Cox 2006). Resource locations for the deposit are well constrained, meaning the predictive capacity of stress-transfer modelling can be tested with potential to identify further exploration targets.

The well-defined fault system at Obuasi makes stress-transfer modelling possible, but its complex geometries present challenges, because of the idealisation required to produce STM models. The region underwent multiple stages of significant deformation, and therefore fault, fold and fracture structures at Obuasi are complex. Representing structural intricacies such as these using planar fault complicates the modelling process and impacts confidence in results. This thesis therefore also presents an extensive investigation into the utility of stress-transfer modelling as an exploration tool, discussing both its potential and its limitations, in theory and in practicality, to assess whether the current lack of interest is justified.

1.2 Aims and Objectives

The principal aim of this study is to investigate the utility and capacity of stress-transfer modelling (STM) in predicting orogenic gold resource distributions, using examples from the Obuasi gold deposit. The research presented in this thesis is based on the hypothesis that supposed modelled aftershock sequence zones represent areas of high fracture permeability, enabling fluid flux, which can be taken as a proxy for predicting gold mineralisation. Assessing the utility of this theory in modern exploration is a secondary aim for this thesis. The third aim is to critically review the software available for performing STM, to provide greater insight into its ease of use, limitations and replicability of results achieved using STM software.

The following objectives have been achieved to complete the investigation:
1. Benchmarking available modelling software to ensure accuracy and reliability by reproducing published results from an existing paper with similar methods and aims to this thesis.
2. Investigating the available features and limitations of this software, particularly regarding the representation of curvature of faults using simple idealised models.
3. Applying stress-transfer modelling to the Obuasi fault system at various scales, investigating multiple stages of gold emplacement and the effectiveness of stress-transfer modelling in explaining the spatial distribution of mineralisation.

1.3 Context of the Obuasi gold deposit

The Obuasi gold deposit (formerly Ashanti) in Ghana is the largest discovered Palaeoproterozoic gold deposit in West Africa, the jewel in the crown of an intensely productive region for gold exploration, with Birimian greenstone belts across Senegal, Mali, Sierra Leone and Ghana hosting well in excess of 150Moz of gold (Markwitz et al. 2016). Commercially mined since 1897, there has been a past

production for the Obuasi deposit of ca. 32 Moz, with a current mineral resource of 34 Moz and an ore reserve of 5.86 Moz (Fougerouse et al. 2017; Oliver et al. 2020). Direct evidence for artisanal gold mining dates back to the 15th century, with miners targeting gossans for near surface gold bearing quartz veins (Fougerouse et al. 2017). Archaeological evidence for the region suggests gold may have been mined for millennia, although exact dating is impossible. The deposit is located 260km northwest of the coastal capital, Accra (Figure. 1.1; AngloGold Ashanti 2020b). The deposit extends around 8km along strike of the otherwise unmineralised Obuasi/Main Reef fissure and to depths of >1.6km. Active exploration is taking place at depth.
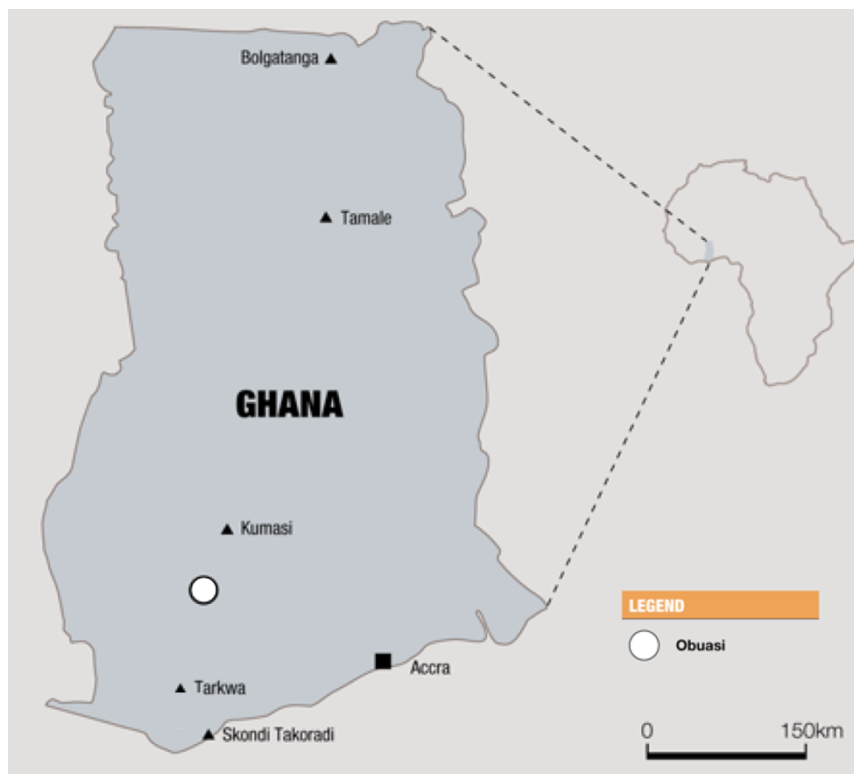
Figure 1.1. A sketch map indicating the location of the Obuasi deposit within Ghana, West Africa, roughly 60km south of Kumasi and 260km northwest of the capital city, Accra. Modified after futureofobuasi.com

Obuasi is experiencing a government supported renewal of operation. Production at Obuasi had declined in the late 20th century due to high operating costs, despite a retraction of a 35% government stake in 1994, from 55% to just 20%. The

introduction of a BIOX bio-oxidation plant in the same year did not improve the output enough to offset costs and production targets were missed for the following 20 years. Production was eventually wound down in 2014 and the mine was placed on care and maintenance in 2016. The Obuasi deposit is now in a redevelopment phase, where AngloGold Ashanti intend to extend the life of the historic mine for a further two decades, following a full hiatus in production from 2016. The first new gold pour at Obuasi was achieved on the 18th of December 2019 (AngloGold Ashanti 2020a), heralding an optimistic new future for a deposit that has been consistently productive but shy of economic targets for a long time. New mining techniques and recovery processes significantly underpin this improved outlook. Previous cut-and-fill stopes are being converted to mechanised open stoping to improve productivity, accompanied by significant processing plant upgrades. Upgrades are necessary as recovery is a particular challenge at Obuasi, due to gold occurrence in multiple milling habits and variable arsenic content. Obuasi is a deposit with significant arsenopyrite-hosted gold, which has caused issues for surrounding settlements in the past (Amasa 1975). Arsenic assessments are being conducted by local agencies in conjunction with AngloGold Ashanti to better tackle this issue (e.g. Nude et al. 2016).

1.4 Deposit Geology

Obuasi is located within the Archean-Palaeoproterozoic Leo-Man Shield, part of the southernmost portion of the West African Craton (WAC). A geological summary map for the West African Craton with located gold deposits, including Obuasi, is presented in Figure 1.2, modified from Markwitz et al. (2016). A key feature to note is the productivity of the Birimian greenstone belts, particularly the Ashanti belt. The West African Craton contains 153 named orogenic gold deposits according to the West African Mineral Deposit Database, which are hosted in a variety of lithologies including: intrusive- and extrusive-mafics, granitoids, metasediments, carbonates, and banded iron formations. Typical West African gold deposits exhibit strong quartz veining, which often hosts mineralisation. Greenschist metamorphic facies are the most common, with some deposits found in lower amphibolite facies.
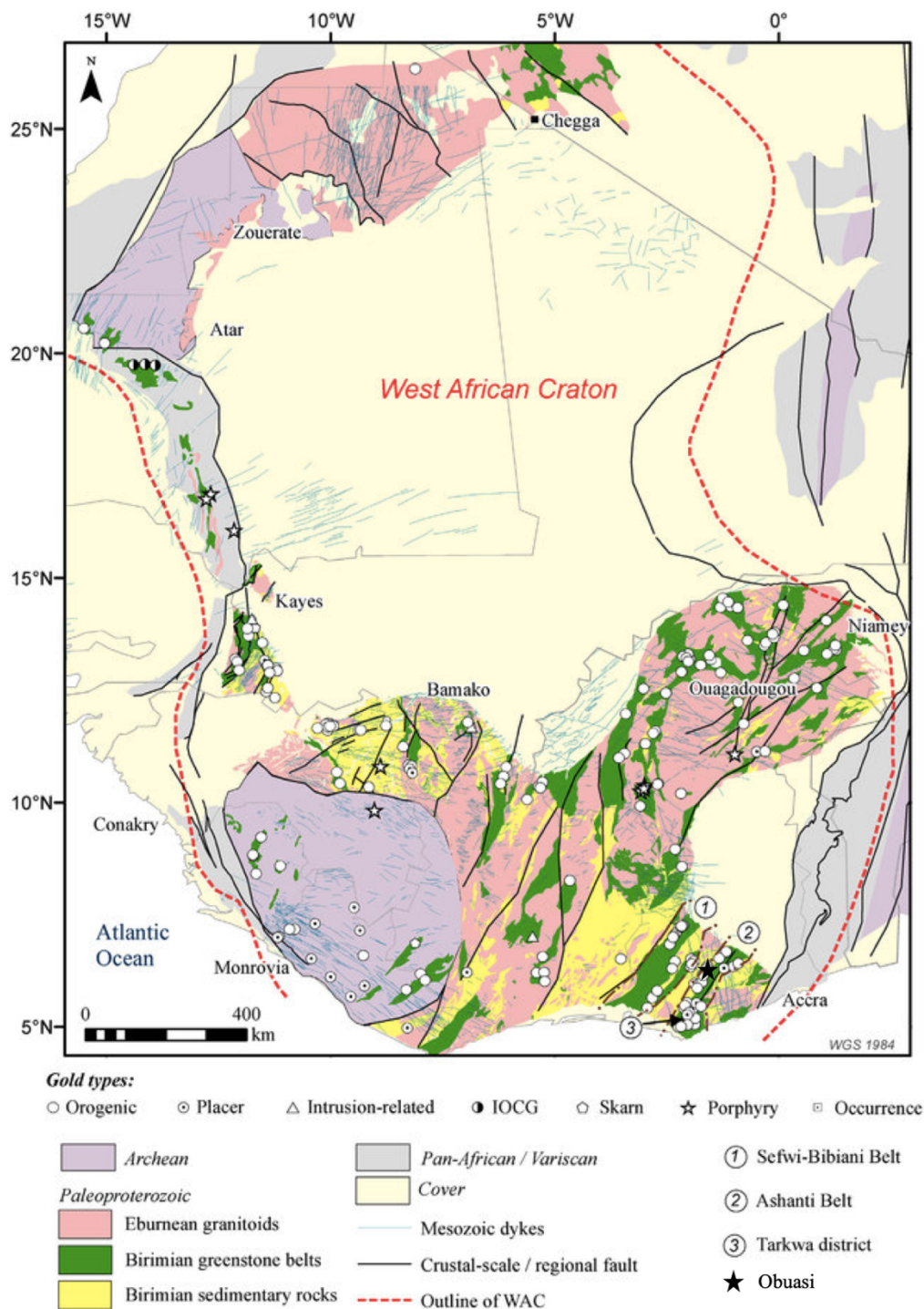
Figure 1.2. A generalised geological map of the West African Craton indicating the location of the major gold deposit types and locations, their relation to large scale structural features and locating the Obuasi deposit. Modified after Markwitz et al. (2016).

Much of the central WAC is dominated by the Neoproterozoic-Palaeozoic Taoudeni Basin cover (Peucat et al. 2005). What the Taoudeni Basin does not cover in the south of the WAC is predominantly gold bearing Archean and Palaeoproterozoic rock, principally found throughout Ghana, Senegal, Burkina Faso, Liberia, Ivory Coast and Mali. The Archean rocks of the southern WAC are termed the Kénema-Man domain, while the Palaeoproterozoic rocks are the Baoulé-Mossi domain, along with the associated Kédougou-Kénieba Inlier of Mali and Senegal (e.g. Gueye et al. 2013; Dabo et al. 2016).

The geology of SW Ghana can be split into 4 principal components:

1. The Archean basement gneisses of the Leo-Man Shield, which are not exposed in the Ashanti region and are not directly encountered in this research.
2. A series of NE-SW trending greenstone belts belonging to the Sefwi Group. Those around Obuasi include the Sefwi, Ashanti and Kibi belts, and are interpreted to have been emplaced between 2.25 and 2.17Ga. Initially marked by a period of volcanism, the first N-S regional compressional event, variably known as the Eburnean I (Allibone et al. 2002; Feybesse et al. 2006) orogeny or the Eoeburnean (Perrouty 2012) orogeny subjected the basalt suites to greenschist to amphibolite facies metamorphism, forming these belts.
3. The Sefwi Group greenstones are divided by sedimentary basins, the Sunyani, Kumasi-Afema and Comoé, deposited between 2.15 and 2.1Ga (Oberthür et al. 1998; Feybesse et al. 2006; Perrouty 2012). These are interpreted to have been initially deposited in a period of extension between the Eburnean I and II orogenies, which folded and inverted much of this sediment.
4. The Tarkwaian sediments, interpreted to be consistent with a syn-orogenic foreland basin related to the Eburnean II orogeny, were deposited ~2.132 and 2.097Ma (Oberthür et al. 1997). Four layers of variable conglomerates, sandstones and phyllites have been identified, the Kawere conglomerates, Blanket Conglomerates, Tarkwa phyllites (including the palaeo-placer Tarkwa gold deposit), and Huni series sandstones (Perrouty 2012).
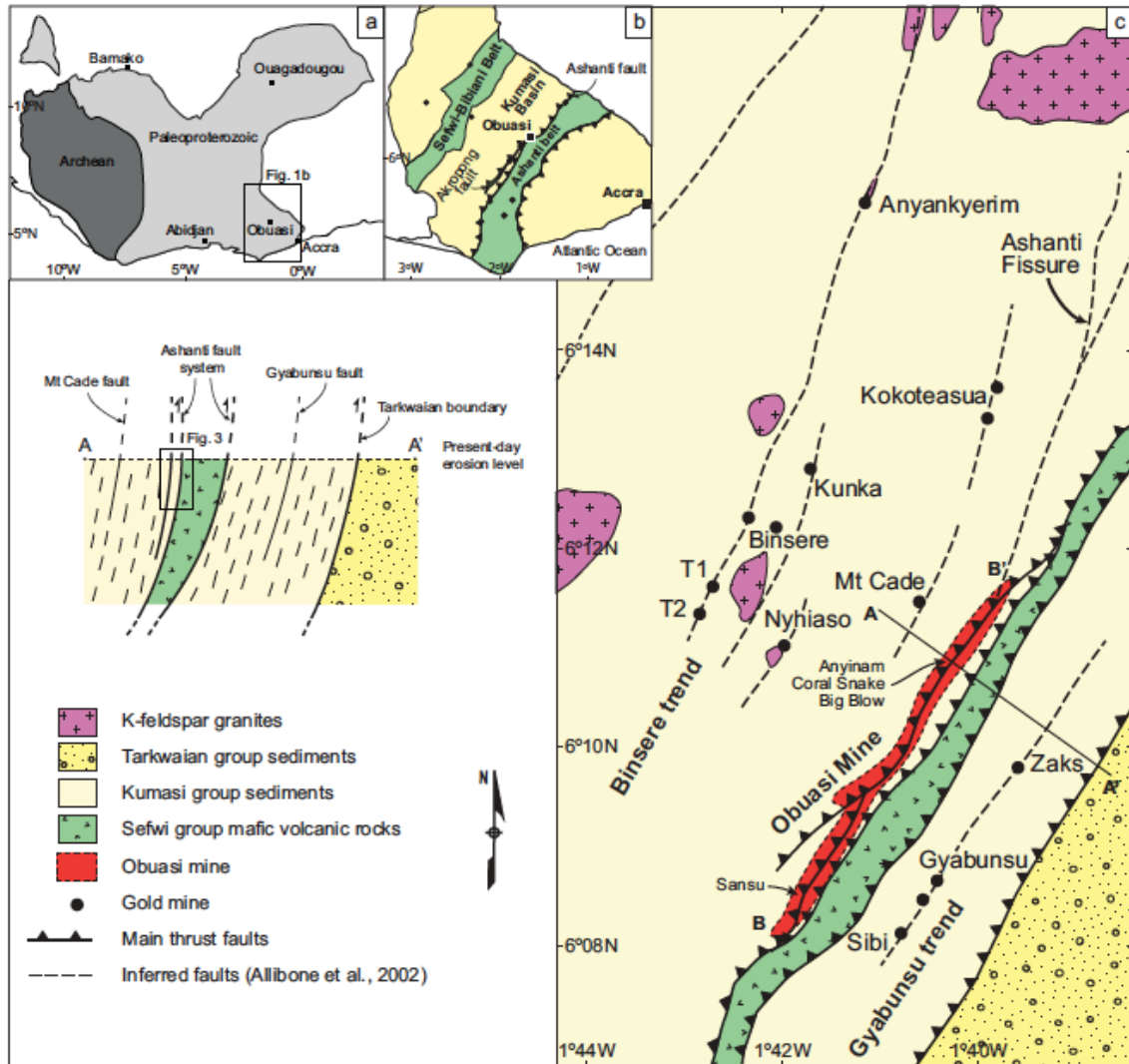
Figure 1.3. A. A schematic overview of the southern section of the West African Craton. B. The Birimian greenstone and sedimentary belts of the Obuasi region, with the major Ashanti and Akropong faults indicated. C. District geology for the Obuasi deposit, showing major rock units and structural trends as identified by Allibone et al. (2002). Strikes are consistently NE-SW for regional shear zones. An interpretation of these structure in cross section is presented, its location indicated on the district scale map. Source: Fougerouse et al. (2017)

The Obuasi deposit is addressed specifically in a number of papers (Eisenlohr and Hirdes 1992; Schwartz et al. 1992; Blenkinsop et al. 1994; Oberthur et al. 1995; Oberthür et al. 1997; Oberthür et al. 1998; Allibone et al. 2002; Perrouty 2012;

Fougerouse et al. 2016; Fougerouse et al. 2017; Oliver et al. 2020). It is hosted in the metasediments of the Birimian Kumasi basin, a combination of carbonaceous phyllites, volcanosediments, slates, greywackes and psammites, deposited between 2157 and 2125Ma (Oberthür et al. 1998; Feybesse et al. 2006; Perrouty 2012). These are interpreted as a turbidite sequence (Oberthur et al. 1995). The area also contains older (2187 to 2158Ma) Sefwi group metabasalts, mafic volcaniclastics, rhyolites and 'belt type granitoids' (Perrouty 2012). These are overlain by the sedimentary Tarkwaian Group of conglomerates, sandstones and phyllites, placed with detrital zircons to around ~2107 to 2102Ma (Oberthür et al. 1998; Oliver et al. 2020). The ore-bearing zone is crosscut by younger, unmetamorphosed and unmineralised dolerite dykes.

Gold at Obuasi is found in several forms (Oberthur et al. 1995; Fougerouse et al. 2016; Fougerouse et al. 2017). Disseminated arsenopyrite-hosted gold is common within the metasediments, and free gold is hosted in high grade quartz-carbonate veins. Blebs of electrum appear in late-stage veining, although the former two modes of occurrence are the economically important phases. The different ore characteristics are interpreted by some (Fougerouse et al. 2016; Fougerouse et al. 2017; Oliver et al. 2020) to be the result of multiple stages of gold emplacement, a hypothesis which deviates from the often discussed (e.g. Groves et al. 2019) single stage model. Earlier interpretations suggest a single mineralisation timing (Schwartz et al. 1992; Blenkinsop et al. 1994; Oberthur et al. 1995; Oberthür et al. 1998; Allibone et al. 2002), although this may have taken the form of a separated or evolving fluid. The refractory gold is interpreted in the recent literature to have been distributed in a first stage through the metasediments and then remobilised. Free gold in shear zone hosted quartz veins might have been emplaced in either stage, while electrum in late-stage veins appears independently to the shear zone hosted stage. The gold at Obuasi is, as in all orogenic deposits, structurally controlled and focused into ore shoots. In addition to structural control, Sefwi group mafic volcanics in the deposit add a lithological control on ore shoot geometry.

As an orogenic gold-type deposit, Obuasi exhibits most of the typical features of the deposit class such as host lithology, structural control, and late-orogenic tectonic regime during gold emplacement, which is important for this thesis. The term

'orogenic gold deposit' was proposed by Groves et al. (1998) to replace the 'mesothermal' (e.g. Sibson et al. 1988; Kerrich and Wyman 1990; Gebre-Mariam et al. 1995) classification widely applied to a class of deposit formed under greenschist to amphibolite facies metamorphism at 15-20km depth. Noting that deposits referred to as 'mesothermal' occurred across a wider range of temperatures and pressures than the descriptor implies, the unifying factor of formation under compressional to transpressional orogenic tectonics was used to rename the deposit class. Building upon the 'crustal-continuum model' (Groves 1993; McCuaig et al. 1993), the Groves-led research group has dominated publication of literature related to this deposit class for over 20 years (e.g. Goldfarb et al. 2001; Vielreicher et al. 2007; Goldfarb and Groves 2015; Groves et al. 2016; Groves and Santosh 2016; Groves et al. 2018; Groves et al. 2019). The orogenic descriptor was not immediately accepted (e.g. Cox and Ruming 2004) and while currently exceedingly popular it retains critics, particularly with regard to the weakness of the model in identifying a source for gold in the system (Tomkins 2013). The crustal-continuum model establishes an empirical descriptor for a deposit class formed of vertically extensive Au-dominant mineralisation zones, generally associated with crustal scale shear zones and with the most likely gold bearing fluid sources appearing to be metamorphic in origin. These fluids are most often interpreted to be low-salinity and CO_2 rich (e.g. Pitcairn et al. 2006; Phillips and Powell 2010). Because these conclusions remain broad and empirical, the benefits of the prolific Groves-led literature for exploration have been questioned (Gaboury 2019). In the context of this thesis, 'orogenic gold' as a deposit class descriptor is an adequate term. The principal benefit to Obuasi fitting this descriptor is that the theoretical precedent set using similar deposits in Western Australia (Cox and Ruming 2004; Micklethwaite and Cox 2004; Micklethwaite and Cox 2006) was useful in guiding the methods of this research.

1.5 Structural Evolution

The structural evolution of Obuasi is complex, especially as local deformation events relate to regional deformation events but do not directly correlate with them. Work by Oliver et al. (2020), contains a synthesis of the current understanding, using multiple previous structural studies of the area (e.g. Blenkinsop et al. 1994; Allibone et al. 2002; Perrouty 2013; Fougerouse et al. 2017) to form a general structural history of the region and then Obuasi specifically. This thesis uses the structural history described in Oliver et al. (2020), taking this as the most complete synthesis available in the literature.

The formation of the Ghanaian Palaeoproterozoic was extensively reviewed by Feybesse et al. (2006), who describe the accretion of the domain up to peak gold emplacement and its subsequent deformation. The formation of the province is discussed with gold distributions, palinspastic reconstructions and stress mapping undertaken for the area. The paper is a synthesis of numerous studies by the BRGM between 1987 and 2006 to better constrain the evolution of this extensively productive gold province.

The Palaeoproterozoic rocks of the Leo-Man Shield are interpreted to represent magmatic and tectonic accretion of proto-Ghana onto the Archean São Luis Craton by the compressional-transpressional Eburnean orogeny (2.13 Ga- 1.98 Ga). The formation of the province as presented by Feybesse et al. (2006) is summarised in Table 1.1.

Stage	Timing	Event
1	Siderian, ~2.35 Ga to 2.3 Ga.	Deposition of BIF-sequences and volcano-sedimentary rocks at the margin of the Archean São Luis Craton. Onset of magmatic and tectonic activity.
2	Eoeburnean, 2.25 Ga to 2.17 Ga.	Magmatic accretion, forming the Sefwi, Ashanti and Kibi belts.
3	2.16 Ga to 2.15 Ga.	Continental crust construction and thickening. Continued magmatism emplaces monzogranites within the crust.
4	2.15 Ga to 2.10 Ga.	Potentially extensional transition period from magmatic Eoeburnean accretion and Eburnean (orogenic) tectonic accretion. Sunyani, Kumasi-Afema and Comoé sedimentary basins formed, interpreted to have been foreland basins.
5	First Eburnean orogenic stage, 2.13 Ga to 2.10 Ga. (Feybesse D1)	Thrust tectonism, defined by a pervasive foliation related to the stacking of volcanic and sedimentary belts making up the Baoulé-Mossi domain.
6	Second Eburnean orogenic stage, 2.095 Ga to 1.980 Ga. (Feybesse D2-D3)	Transition from thrust tectonics to transcurrent tectonics. Termed D2-D3, where D2 marks the change in tectonic style and D3 the end of the orogen. Gold emplacement is attributed to this phase, marked by extensive folding.

Table 1.1: A table presenting a synthesis of the regional tectonic history of the Palaeoproterozoic Ghanaian province after Feybesse et al. (2006)*. Initiated by the break-up of the São Luis Craton, the region undergoes a depositional and accretional phase followed by the onset of the Eburnean Orogeny, which transitions from thrust to transpressional tectonics, during which time gold is emplaced.*

Feybesse et al. (2006) was a key paper in establishing a chronological model for the development of the mineralised domain containing Obuasi. Regional deformational events used for Obuasi specific literature vary in their labelling, depending on the age of the paper and varying confidence in evidence for deformational events. The classification used by Oliver et al. (2020), contains additional interpretations based on the work of McFarlane et al. (2019) using evidence from the Sefwi belt and both draw significant influence from work by Perrouty (2012), who presented insights into the timing of crustal growth and deformation from the entire Ashanti belt. Two main phases are defined, the Eoeburnean (2.19 Ga to 2.15 Ga) and the Eburnean (2.13 Ga to 2.07 Ga), defined by two separate periods of granitoid emplacement. The synthesis of local deformation events specifically affecting Obuasi described in Oliver et al. (2020), closely reflecting that described by Perrouty (2012) is shown in Table 1.2, with relation to the cratonic scale events of Feybesse et al. (2006) in Table 1.1.

Stage, (Stage name) (Oliver et al. 2020)	Timing	Event	Relation to cratonic stages of Figure 1.4 (Feybesse et al. 2006; Perrouty 2012)
1 (D1)	Eoeburnean, 2.155 Ga to 2.145 Ga.	N-S contraction and metamorphism.	3., 4.
2 (D2)	Eburnean, 2.135 Ga to 2.118 Ga.	NW-SE extension, basin formation.	Later than (Feybesse et al. 2006)
3 (D3)	Eburnean, 2.1 Ga to 2.095 Ga.	NW-SE contraction, basin inversion and metamorphism	Later than (Feybesse et al. 2006)
4 (D4)	2.095 Ga to 2.085 Ga	Sinistral wrenching resulting in folding and faulting	D2-3 of Feybesse et al. (2006), omits the NNW-SSE shortening attributed to this stage by Perrouty (2012).
5 (D5)	2.085 Ga onwards	Extension followed by further wrenching	Extends past (Feybesse et al. 2006), deviates from D5 and D6 of Perrouty (2012).

Table 1.2: A table presenting a synthesis of the regional tectonic history of the Obuasi deposit province after Oliver et al. (2020)*. The regional tectonic history roughly corresponds to the later stages of the regional tectonic history* (Feybesse et al. 2006; Perrouty 2012) *and to the onset of the Eburnean Orogeny, following as it transitions from thrust to transpressional tectonics.*

Oliver et al. (2020) synthesise this information (Figure 1.4). As noted by Vidal and Alric (1994), attempts to apply global interpretations from the WAC to specific Birimian units generally fall short, as local complexity, especially volcanism, make correlation challenging. An understanding the broad evolution of the craton is sufficient for context in this thesis, as the correlations available between regional and local deformation events provide enough information to conduct STM. The key stages associated with gold at Obuasi (using Oliver et al. 2020) at a regional scale

are accepted to be D3 and D4, the tail end of the Eburnean orogeny. This is consistent with the accepted timing of emplacement for typical orogenic deposits (e.g. Groves et al. 2019). The Oliver et al. (2020) synthesis of previous structural interpretations at Obuasi (Figure 1.4), provides the most complete picture of current understandings of the structural evolution at Obuasi used for this research. Five local deformation events are identified in this paper, taking place within regional D3 and D4 (the latter phase of the Eburnean orogeny and the shift to transpressional tectonics directly following).
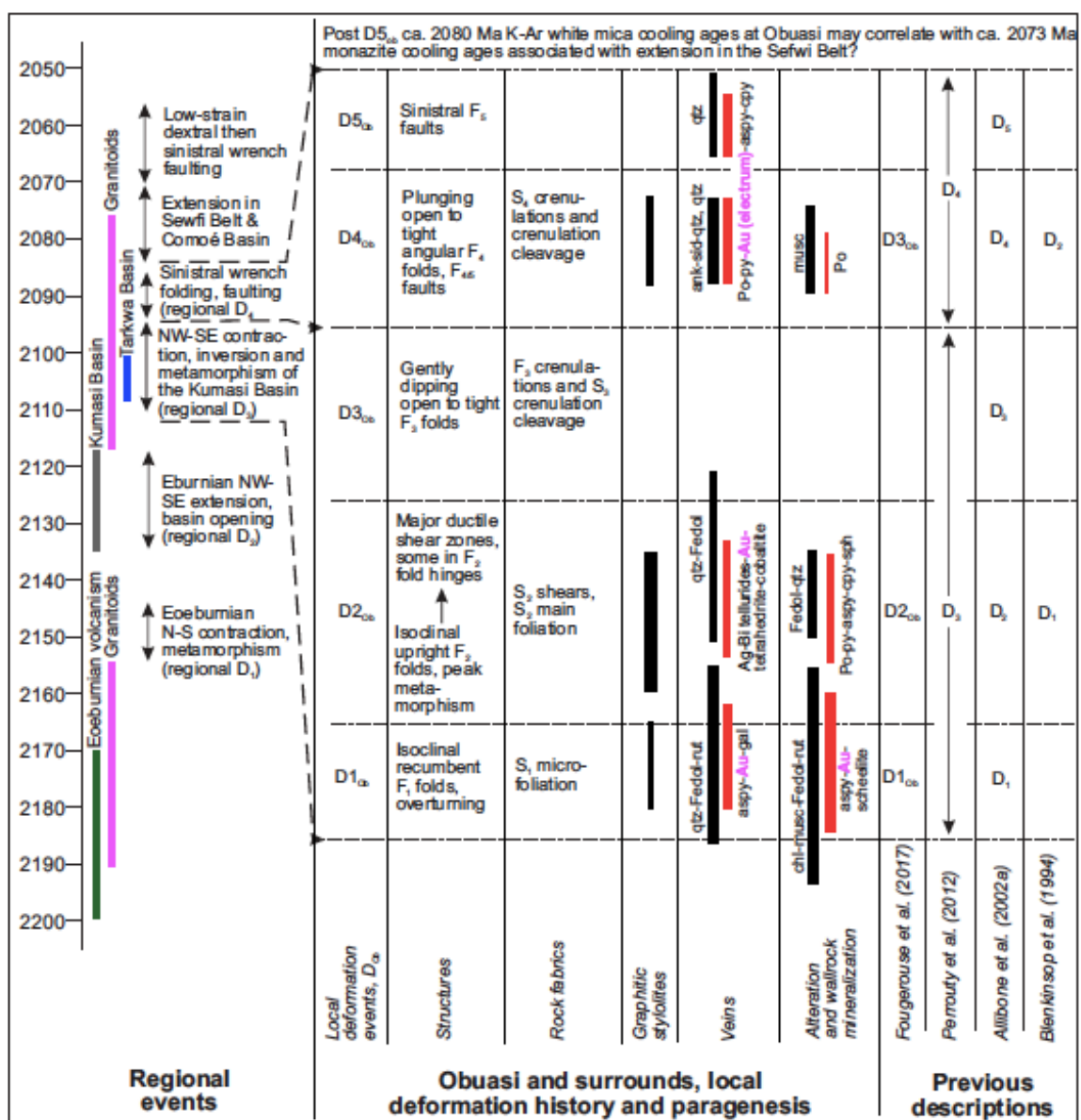
Figure 1.4. A synthesis of regional and local deformation events at Obuasi, including paragenesis and comparisons to previous studies. Source: Oliver et al. (2020)

The structural history of this deposit is a significant contributing factor to the complexity of mineralisation geometries. The local deformation events denoted as $D1_{Ob}$-5_{Ob}, Figure 1.4 (Oliver et al. 2020) are identified by distinct structures and fabrics. Many of these fabrics were identified in earlier studies (Blenkinsop et al. 1994; Allibone et al. 2002; Perrouty 2012) but were variously attributed to various deformation events according to the interpretations of each paper. Here they are labelled using the local D_{Ob} classification scheme, the most current interpretation. Fabric labelling relates to timing of the 5 local deformation events:

- $S1_{Ob}$ A microscopic, poorly preserved foliation.
- $S2_{Ob}$ Strong, generally bedding-parallel cleavage interpreted to match peak metamorphism, with dip varying from southeast to northwest.
- $S3_{Ob}$ Poorly preserved crenulation cleavage related to $F3_{Ob}$ folding.
- $S4_{Ob}$ Well preserved crenulation cleavage related to prominent $F4_{Ob}$ folding.

Details of the major structures at Obuasi that are presented as summaries in Figure 1.4 are:

- $F1_{Ob}$ Overturned isoclinal recumbent folding implied by $S1_{Ob}$ foliation. Orientation varies due to subsequent deformation (Allibone et al. 2002).
- $F2_{Ob}$ Isoclinal upright folding, visible only at microscopic scale in later fold hinges or at km scale with hinge zones heavily deformed. These are generally concordant with the northeast structural trend of the deposit.
- $F2_{Ob}$ Significant, large scale shear zone thrust faults striking northeast.
- $F3_{Ob}$ Poorly preserved, gently dipping open to tight folds. Their axial planes generally strike northeast and dip between 5º SE and 40ºNW (Blenkinsop et al. 1994; Allibone et al. 2002). The hinge tends to plunge NE, however SW plunges also occur (Allibone et al. 2002).
- $F4_{Ob}$ Meso- to macro-scale NE plunging open to tight folds, which are the most pervasive structure at the deposit. These trend east-west and plunge northeast (Allibone et al. 2002).
- $F5_{Ob}$ Well defined sinistral strike slip NE-SW to NNE-SSW trending faults.

Mineralisation at Obuasi appears in two major types, a sulphide-hosted mode disseminated within metasediments and a free milling mode associated with small-displacement quartz veins (Figure 1.7). The emplacement of these phases have been interpreted in multiple ways, but most recent interpretations (Fougerouse et al. 2017) suggest the different occurrences are related to an earlier $D2_{Ob}$ event for the sulphide and a later $D5_{Ob}$ event for the free milling gold. Some small blebs of electrum are also present but do not contribute significantly to the economic reserve. Mineralisation is associated with $D2_{Ob}$ shears, $D5_{Ob}$ strike-slip faults, and hinges and short limbs of $F4_{Ob}$ folds. Mineralised faults and shear zones are known locally as fissures. Examples of fissures are the Obuasi Fissure, Ashanti Fissure, 12/74, Cote d'Or and Main Reef. Some individual ore shoots are also named, e.g. Sansu, Old Chief and KMS. Ore shoots exhibit the strong structural controls typical of orogenic deposits and are generally concentrated where $F4_{Ob}$ fold hinges overprint $D2_{Ob}$ shear zones. In the northwest of the deposit, $D5_{Ob}$ become much more prevalent as a structural control, with gold found in late sinistral faults rather than the large thrust faults that define the majority of the deposit southeast.
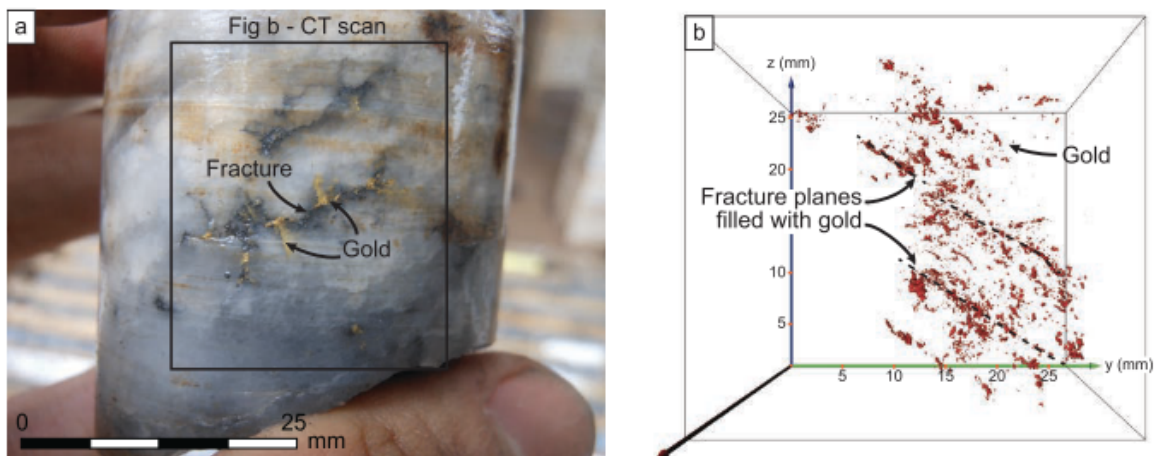
Figure 1.5. Free milling gold in fracture planes in quartz hand specimen, from Figure 12 of (Fougerouse et al. 2017)*. The original caption reads: "a. Hand specimen of quartz hosting visible gold in fractures. b. Isosurfaces showing the three-dimensional gold distribution of gold particles as obtained using high-resolution X-ray computed tomography. Gold fills and defines fracture networks in the quartz vein."*

1.6 Obuasi Grid North

Some deposit specific literature (e.g. Allibone et al. 2002; Oliver et al. 2020) makes reference to Obuasi or Mine Grid North. As is common practice for mines, professionals at Obuasi use a mine-specific map orientation, making deposit-specific maps more compact. Obuasi Grid North, denoted as N(OG) in this thesis, is oriented on a bearing of 296° relative to True North. This is graphically indicated in Obuasi-specific figures and orientations are quantified in text. Any orientations not quantified as Obuasi Grid (OG) should be assumed to relate to True North.

True North

Obuasi Grid North

296°
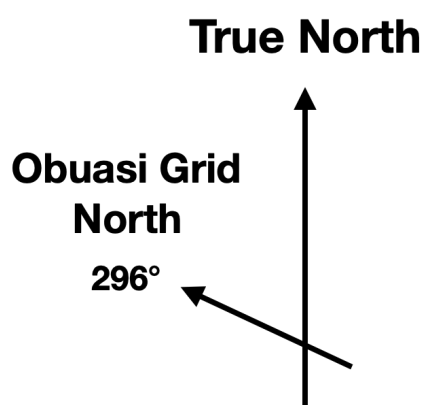
Figure 1.6. Map orientations at Obuasi

1.7 Development of STM

The framework of key concepts that lead Micklethwaite and Cox (2004; 2006) have also been used to guide the methods and conclusions of this research, which builds heavily on earlier work by Sibson. King et al. (1994) demonstrated that following a mainshock event on a strike-slip fault system Coulomb failure stress in the surrounding rock is changed, which can trigger aftershock sequences and potentially new earthquakes. This transferred static Coulomb stress exerts a first order control on the distribution of aftershock sequences (Stein and Lisowski 1983), and these aftershocks enhance permeability in fault systems, allowing for redistribution of fluid on a crustal scale. This was correlated to ancient mineralisation in Western Australia

by Micklethwaite and Cox. After mainshock rupture arrest in strike-slip systems, static stress is concentrated across fault stepovers, making the jogs zones of high fluid flux. When the fluid is gold-bearing, ore shoots are formed, after the theory established in Sibson (1987). This process is the fundamental to this thesis, using predicted zones of high Coulomb stress transfer as a proxy for areas of high ancient fluid flux and a predictor for areas of strong mineralisation.

Deviating from the situation described by Micklethwaite and Cox (2004; 2006), the interpreted multiple stage gold-emplacement at Obuasi places an additional, earlier period of gold deposition during compressional regional tectonics, where the region was dominated by crustal-scale reverse faults. This is investigated in conjunction with strike-slip behaviour.

1.8 Thesis Layout

To achieve the overall aim, this thesis is structured as a series of linked investigations which address individual objectives.

Objective 1:
Benchmarking available modelling software to ensure accuracy and reliability by reproducing published results from an existing paper with similar methods and aims to this thesis.

Chapter 2 presents the modelling methods used, reviewing the theory of Coulomb STM technique and benchmarking against Micklethwaite and Cox (2006), which was used as the methods of this investigation are closely inspired by that study. This was also important because this thesis aims to suggest why the Coulomb stress-transfer technique has not seen widespread application in published economic geology literature and existing methodologies needed to be corroborated by replication to be reapplied with confidence.

Objective 2:

Investigating the available features and limitations of Coulomb 3.3 software, particularly regarding the representation of curvature of faults using simple idealised models.

A brief investigation into representing curvature in Coulomb is conducted in Chapter 3, due to the structural complexity of fault planes at the target deposit. Functionality within Coulomb 3.3 allow planes to be represented as slips on point sources, which are suggested to help represent complex fault geometries. An idealised case trial taking reference from material in Mildon et al. (2016) was used to assess the suitability of this function, helping to establish the methodology taken forward for the full Obuasi investigation.

Objective 3:

Applying stress-transfer modelling to the Obuasi fault system at various scales, investigating multiple stages of gold emplacement and the effectiveness of stress-transfer modelling in explaining the spatial distribution of mineralisation.

The full investigation into Obuasi is divided into two sections, the first, Chapter 4, isolating the later generation (syn-transpressional Obuasi D5 tectonics) strike-slip only Ashanti Fissure, and the second, Chapter 5, addressing the entire mineralised fault system during two local tectonic regimes (compressional Obuasi $D2_{Ob}$ and transpressional $D5_{Ob}$). The investigations closely follow the methodologies of Cox and Ruming (2004); Micklethwaite and Cox (2004); and Micklethwaite and Cox (2006).

An additional investigation is conducted in Chapter 6 into fault-valve behaviour on the Obuasi fault system and its impact on the distribution of gold during $D2_{Ob}$.

Chapter 2.
Modelling Methods

2.1 Coulomb stress transfer modelling

Many contemporary applications of Coulomb failure stress and the triggering of earthquakes are based on the theoretical foundation established by King et al. (1994). Confined rocks in laboratory conditions fail according to the Coulomb criterion, corroborating field observations made in earlier studies (e.g. Jaeger et al. 1979). The Coulomb stress triggering hypothesis infers that an earthquake event permanently deforms the crust and as a consequence alters the stress state on faults nearby. King et al. (1994) show that positive changes in Coulomb stress increase the likelihood of aftershocks on nearby faults, using contemporary seismic events on the San Andreas fault system. Areas of negative stress change following fault slip were shown to have low occurrence of aftershocks, while areas which received an increase of over 0.5 bar of Coulomb stress contained the significant majority of recorded aftershocks.

The mathematical foundation for modelling the effect of a slip in an elastic half-space is set out by Okada (1992). A positive Coulomb stress change of 0.5 bar or greater is enough to trigger a significant number of aftershocks (King et al. 1995). The foundation for static stress changes inducing aftershocks with relation to seismicity and seismic hazards was then strongly established at the turn of the century (King et al. 1995; Harris 1998; Stein 1999; Freed 2005; Steacy et al. 2005a). Conventionally when discussing stress transfer in a half space, papers use the strike, dip, rake convention after Aki and Richards (1980).

Modelling Coulomb stress transfer following a slip event numerically requires rock mechanics and stress state variables:

1. Shear stress change
2. Normal stress change
3. Effective coefficient of friction

These are applied using the Coulomb failure criterion:

$$\Delta\sigma_f = \Delta\tau_s + \mu' \left(\Delta\sigma_n\right)$$

The Coulomb failure criterion resolves change in Coulomb failure stress, $\Delta\sigma_f$, where a positive change brings a plane closer to failure. Change in shear stress, $\Delta\tau_s$, is positive when in the slip vector rake direction and change in normal stress, $\Delta\sigma_n$, is positive if the fault is unclamped. μ' represents the effective coefficient of friction for the fault. Mildon et al. (2019) allude to the possibility of calculating Coulomb stress changes which incorporate pore fluid pressures, where ΔP represents change in pore fluid pressure:

$$\Delta\sigma_f = \Delta\tau_s + \mu' \left(\Delta\sigma_n + \Delta P\right)$$

Version 3.3 of Coulomb available for this study has no capacity to incorporate pore fluid into calculations, so by necessity has been omitted, following the practice of Mildon et al. (2019) and using their justification.

2.2 Coulomb 3.3

Coulomb 3.3 (Lin and Stein 2004; Toda et al. 2005) was designed by the USGS for use in earthquake, tectonic and volcano-focused research (e.g. Toda et al. 2002; Toda et al. 2005; Manga et al. 2009; Toda et al. 2011b; Bie and Ryder 2014; Mildon et al. 2016; Mildon et al. 2019; Hughes et al. 2020). The open-access program has been used in many academic contexts, but the application of this program to economic geology has been generally focused on the mineralising aftershocks theory discussed above.

The software, which is hosted within the MATLAB programming and numeric computing platform, calculates Coulomb stress transfer using the following input parameters:

1.   Regional stress orientations, defined as sigma 1, sigma 2 and sigma 3. A stress gradient can be applied.

2.   Rock mechanics data (Poisson's ratio, Young modulus E, friction coefficient).

3.   Geometries of faults, defined by start and finish x-y coordinates for the top of the fault element, top depth, bottom depth and dip.

4.   Slip vectors, which input as reverse and right lateral. Negative values denote reverse and left lateral slips.

5.   Grid format, which includes x-y extent and grid spacing which defines the resolution.

6.   'Kode', which defines modelling style. Kode values are: 100- whole fault movement. 200- tensile displacement, strike-slip. 300- tensile displacement, dip-slip. 400- point source modelling. 500- point source, inflation or deflation.

7.   Calculation depth, which cannot coincide with the base of fault elements.

Fault planes in Coulomb 3.3 are either 'source' and 'receiver' faults. A source fault has some slip, while receiver faults do not. Calculations of imparted stress can be made on user specified receiver faults, on optimised faults (sinistral/dextral strike slip, thrust and normal) which are derived from the regional stress conditions specified by the user or on all optimised faults which includes every strike and dip for each square of resolution, which is defined by the calculation grid interval. In addition to calculating Coulomb stress transfer, deformation, strain and seismic moment calculations are also available within the package. Coulomb 3.3 models can be constructed and edited using in-program input windows or by directly editing an input file (e.g. Figure 2.2) within MATLAB. Directly editing the input file is significantly faster and easier to troubleshoot for models containing multiple faults, making this the preferred method for this study. Table 2.1 shows the abbreviations used in a Coulomb input file, exemplified in Figure 2.1.

Code	Input file parameter
PR1/PR2	Poisson's Ratio
E1/E2	Young Modulus
FRIC	Coefficient of internal friction
DEPTH	Calculation depth
#fixed	Number of fault elements
S1/S2/S3: DR DP IN GD	Sigma 1/2/3: Direction (strike) Dip Intensity Gradient
#reg1 #reg2 XSYM YSYM	Legacy features, not required for modelling

Table 2.1. Table of abbreviations used in Coulomb 3.3 input file

```
 1   Micklethwaite & Cox 2006
 2   Benchmarking
 3   #reg1=  0  #reg2=  0  #fixed=   7  sym=  1
 4    PR1=      0.250     PR2=      0.250    DEPTH=     10.000
 5     E1=    7.000e+05   E2=    7.000e+05
 6   XSYM=       .000    YSYM=       .000
 7   FRIC=        0.400
 8   S1DR=       60.000 S1DP=        0.000 S1IN=       100.000 S1GD=       365.000
 9   S2DR=       90.000 S2DP=       90.000 S2IN=        30.000 S2GD=       290.000
10   S3DR=      150.000 S3DP=        0.000 S3IN=         0.000 S3GD=        21.500
11
12     #   X-start     Y-start     X-fin      Y-fin    Kode  rt.lat    reverse   dip angle     top       bot
13   xxx xxxxxxxxxx xxxxxxxxxx xxxxxxxxxx xxxxxxxxxx xxx xxxxxxxxxx xxxxxxxxxx xxxxxxxxxx xxxxxxxxxx xxxxxxxxxx
14    1   2.7330      4.6150     4.1810     9.0680  100 0.3330     0.0000     90.0000     2.0000   15.0000
15    2   4.1810      9.0680     4.1090    11.1310  100 0.3330     0.0000     90.0000     2.0000   15.0000
16    3   4.1090     11.1310     5.4480    16.5250  100 0.3330     0.0000     90.0000     2.0000   15.0000
17    4   6.3170     17.7190     8.1630    21.8460  100 0.2500     0.0000     90.0000     2.0000   15.0000
18    5   8.1630     21.8460     8.0180    25.6470  100 0.2500     0.0000     90.0000     2.0000   15.0000
19    6   8.0180     25.6470     8.4520    26.4800  100 0.2500     0.0000     90.0000     2.0000   15.0000
20    7   8.4520     26.4800     8.3080    28.8690  100 0.2500     0.0000     90.0000     2.0000   15.0000
21
22       Grid Parameters
23    1   ------------------------- Start-x =        0.0000000
24    2   ------------------------- Start-y =        0.0000000
25    3   ------------------------- Finish-x =      10.0000000
26    4   ------------------------- Finish-y =      30.0000000
27    5   ------------------------- x-increment =     0.1000000
28    6   ------------------------- y-increment =     0.1000000
```

Figure 2.1. An example Coulomb 3.3 input file. Lines 1&2 title of file, 3-10 rock mechanics and stress conditions 12-20 fault element geometries, 1 line per fault with start and finish X-Y coordinates, dip angle, slip movement (m) and fault depth extent, 22-28 grid area, X-Y extent, increment defining calculation resolution

2.3 Benchmarking

The aim of benchmarking is to establish the most accurate and best possible application of software (Daneva 1996). In the context of Coulomb 3.3, this stage helped to develop familiarity with the program and its input system and improve the reliability of original research results by minimising human error. This aim was achieved by replicating results from existing research (Micklethwaite and Cox 2006). Additionally, when selecting the paper to replicate, it became apparent that across the economically focused literature (e.g. Cox and Ruming 2004; Micklethwaite and Cox 2004; Cox 2005; Micklethwaite and Cox 2006; Micklethwaite 2013; Kozłowska et al. 2015) and even literature published by the program's developers (e.g Toda et al. 2005; Toda et al. 2008; Toda et al. 2011b), researchers often failed to include all the input parameters used to create modelling results. This meant that many of the results were not replicable using the published material, and this is the reason that benchmarking in this chapter is necessary. All input parameters are available in this thesis via the original input files (Appendix I).

In a series of papers investigating gold deposits in the Kalgoorlie greenstone belt of Western Australia Cox and Ruming (2004) and Micklethwaite and Cox (2004),(2006) demonstrate that static-stress controlled aftershocks exerted a control on the distribution of gold mineralisation, due to the permeability enhancement and fluid transport that can occur during aftershock sequences. The section of Micklethwaite and Cox (2006) regarding the Black Flag Fault was selected for benchmarking. The Black Flag Fault is located in the Mount Pleasant Goldfield and is hosted within the Kalgoorlie greenstone terrane (Eisenlohr et al. 1989; Micklethwaite and Cox 2004). The system, a classic Yilgarn Craton orogenic gold deposit, was selected as favourable to aftershock-based modelling due to its dilational jog structural setting. Gold is hosted in small-displacement veins, which are small sections in a larger strike-slip system (Micklethwaite and Cox 2004). The Black Flag mineralised faults are generally <1.0km in length, with variable orientations with relation to the associated larger unmineralised faults, and exhibit 1-100m maximum offsets. They are hosted within an understepping, hard-linked dilational jog (stepover). The study achieved good correlations between zones of positive Coulomb stress, resolved on

dextral strike-slip receiver faults, and areas of mineralisation in a resource model. This correlation is interpreted to support the theory that zones of calculated positive Coulomb stress correspond to areas of ancient aftershock sequences, related to larger slips on the Black Flag fault system and controlled by the stepover structure. The aftershock sequences are interpreted to have enhanced permeability across the stepover, resulting in preferential gold mineralisation. The aim for this thesis is to test whether similar correlations can be made for the Obuasi deposit using similar methods.

2.4 Methods

To replicate the results of Micklethwaite and Cox's (2006) investigation on the Black Flag Fault, published results for which are shown in Figure 2.3, as many of the input parameters as available were collated and used to reverse-engineer the model used for the original study. Using ImageJ, a free Java based image processing package (Abràmoff et al. 2006; Rasband 2015), measurements of the Black Flag Fault surface traces used for this model were extrapolated to x-y coordinates. The reference figure, Figure 2.2, was published in a format that allows fault traces to be accurately replicated for the extent shown in Figures 2.2B-2F, with fault elements outside of the sampled area estimated for the model from the larger extent provided in Figure 2.2A, the resolution of which prevents reproduction to the same accuracy.
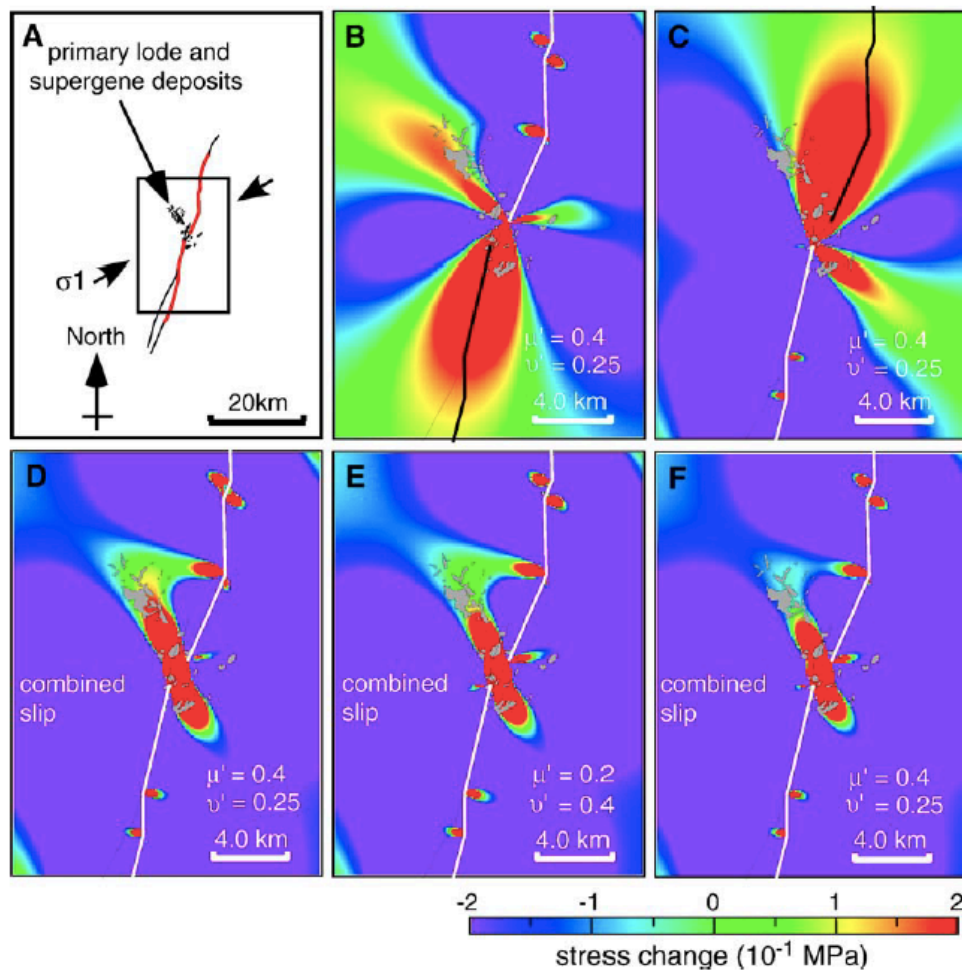
Figure 2.2: The original Figure 5 from Micklethwaite and Cox (2006), elements of which have been directly replicated in this chapter. The original caption reads: 'Calculations of Coulomb failure stress change for optimally oriented faults (dextral strike-slip faults). Results are compared from fault slip on the two major segments of the Black Flag fault (white lines) with the distribution of fault-hosted gold deposits (grey polygons) in the Mt Pleasant goldfield. (A) Model setup. (B) Static stress change from slip on northern segment. (C) Static stress change from slip on southern segment. (D) Combined-slip stress change (resulting from slip on both fault segments). An excellent correlation exists between the combined-slip static stress change and the distribution of mineralization. (E) Model with lower value of apparent friction. The distribution of positive static stress change is not significantly affected by variations in this parameter. (F) Model with low Poisson's ratio appropriate to dry mafic rocks. The distribution of positive static stress change is not significantly affected by variations in this parameter.' Micklethwaite and Cox (2006)

It is stated in the original paper that for Black Flag, faults dip vertically from 2 km to 15 km depth and were sampled at 10 km, although due to the lack of horizontal displacement and purely dextral strike-slip movement results are similar at any calculation depth. It is also stated that 1m of dextral strike-slip movement was modelled on both the northern and southern segments. Through trial and error, it was ascertained this means that 1m total slip was modelled, i.e., 1m of slip divided evenly between all the fault elements making up each segment. Rock mechanics values were applied using those of the original paper (Micklethwaite and Cox 2006).

To replicate Figure 2.2 B, C and D, 1m of total slip was modelled on the northern and southern segments separately, to represent B and C respectively. For the northern segment, four fault elements were present, meaning slip was evenly distributed at between them, at 0.25m apiece; a similar procedure was applied to the three fault elements of the southern segment in 2.2C. A 'combined-slip' model was run, which incorporated 1m total slip on both segments, north and south, reproduced Figure 2.2D. This was resolved on optimised dextral strike-slip faults, as specified by Micklethwaite and Cox. The type of receiver fault stress was resolved on was provided in the figure caption. A colour-dropper function in ImageJ was used to match the colour gradient as accurately as possible, using hex codes and the colourbar editor in Coulomb. This included editing the intensity of gradient between the extremities and centre point.

2.5 Results

A close match was achieved between the results in Figure 2.2 and the benchmarking copy made in Coulomb 3.3. These results, with comparison to their original counterparts are shown in Figure 2.3. Figure 2.3A shows just slip on the northern segment, 2.3B on just the southern segment and 2.3C shows the combined slip, which emulate B, C and D of Micklethwaite and Cox's (2006) Figure 5. The match is sufficiently close to say that the results are repeatable but on close inspection is not an exact match. This confirms that with enough input parameters provided in the

original work, results are replicable to an acceptable level, but exact replicas are unlikely.
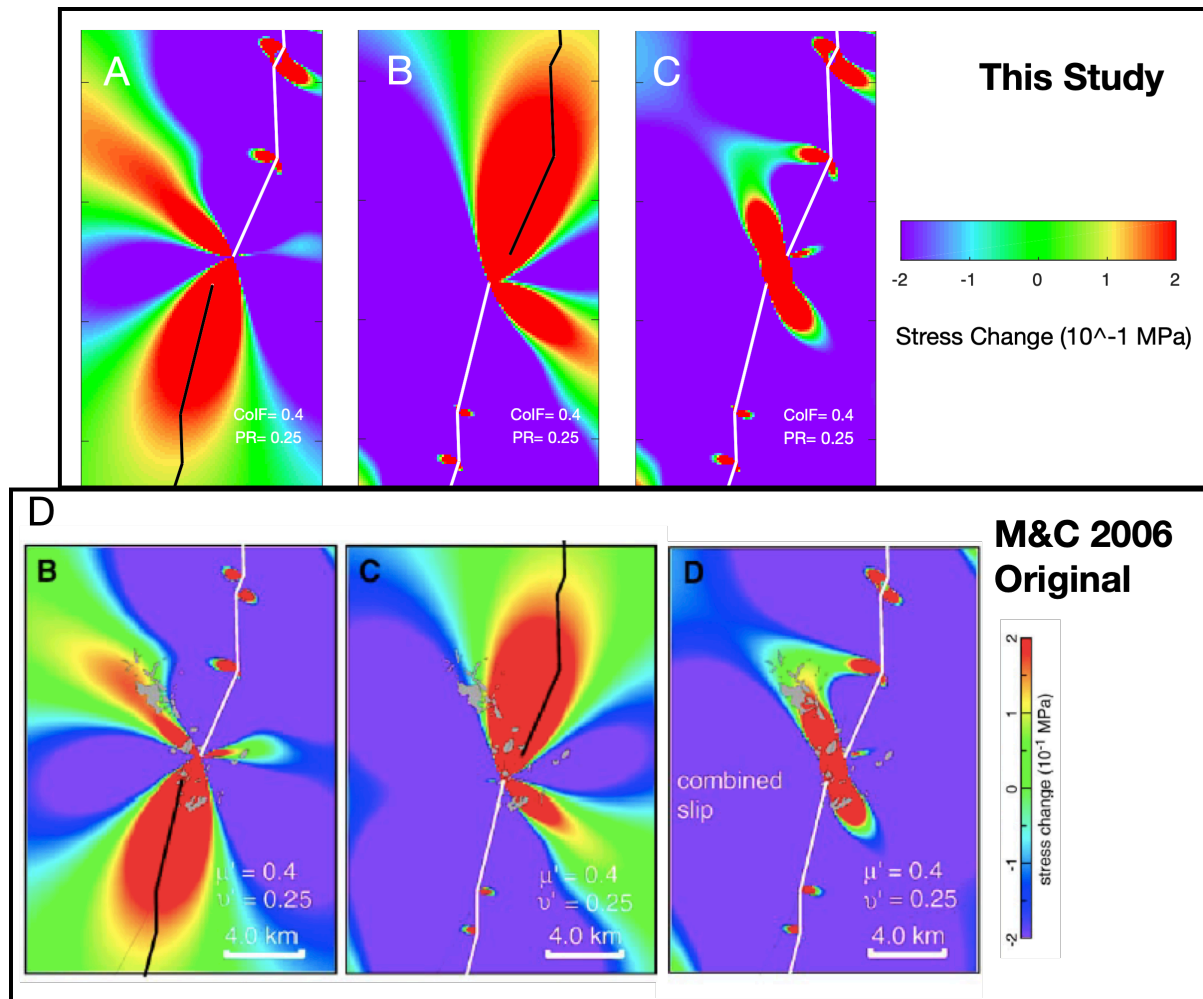
Figure 2.3: Static stress changes figures replicated from Micklethwaite and Cox (2006). A. shows static stress change on the northern segment, equivalent to M&C (B.). B. static stress change on the southern segment, equivalent to M&C (C.). C. combined-slip stress changes, equivalent to M&C (D.). D. (inset, from Micklethwaite and Cox (2006) Figure 5:) the original figures that have been replicated.

2.6 Discussion

The results presented above show that benchmarking was successful. An existing result from published literature was replicated, which establishes confidence for the further investigation.

The results in this chapter are sufficiently close to the original figure to indicate that the original model setup was adequately replicated. The lack of an exact match is most likely because the exact fault element geometries used by Micklethwaite and Cox (2006) cannot be accurately extrapolated further than the bounds of Figure 2.2 B-F but have an effect on the patterns of static Coulomb stress change observed within the cropped bounds. It is evident from the benchmarking input used to produce Figure 2.4A that the graphical outputs used by Micklethwaite and Cox (2006) have been cropped to achieve the originals shown in Figure 2.2. This is also evident because if the extents of the fault elements were to stop at the bounds of B-F, lobate patterns of Coulomb stress from the terminations of each of the fault segments would be observed.

Not knowing the exact number of fault elements used affects the way 1m of total slip is divided between fault elements. For example, in Figure 2.3A, the northern segment has been represented by 4 fault elements, meaning each element is assigned 0.25m of dextral strike-slip movement (See Figure 2.1 input file). As the southern segment has been represented with 3 elements, each is assigned 0.333 m of movement. Not knowing the total number of fault elements means these might not be the same values assigned in the original paper. The results achieved suggest good approximations were made, but this cannot be confirmed without seeing the original file. Using software like ImageJ significantly improves the accuracy of recreating a model in this manner. However, it cannot be guaranteed that each fault element is replicated exactly due to the inexact pixel resolution and ambiguity in start and end points. Small inaccuracies such as this impacted the final result, although the general replication is accurate enough to be deemed successful.

This investigation raises some crucial points for the accuracy, replicability and reliability of further Coulomb stress investigations. The difficulty encountered in obtaining input parameters from many published works highlights the need to include all input parameters, if necessary as a supplementary file, so that all input parameters are clear and fault elements are provided, which eliminates the problem of cropping figures.

In addition to publishing the input file, the type of optimally oriented fault used to resolve Coulomb stresses onto is an important choice which should be justified in text. Resolving on different optimised fault types, shown in Figure 2.4, significantly impacts the calculated patterns of Coulomb stress. In this example, the original result for optimised strike-slip faults has been contrasted with resolution on optimised thrust faults. The results for optimised thrust faults would have shown much less meaningful correlation for the original paper and would have been an unlikely fit considering the original stress conditions, making the conclusions of the paper difficult to justify. Micklethwaite and Cox (2006) selected different optimised faults in their investigations, which could be interpreted to match original stress conditions, using only dextral strike-slips on the Black Flag Fault but both thrust and strike-slip faults on the Playa-Lefroy.
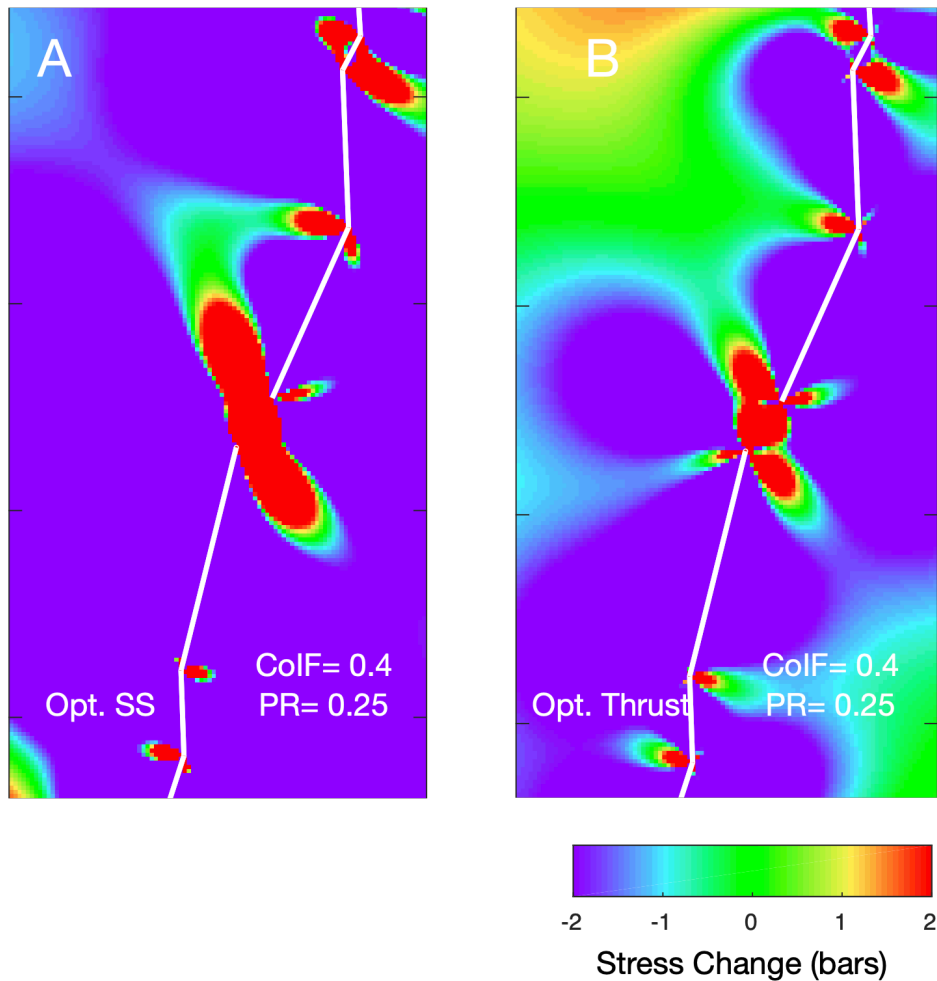
Figure 2.4. Static stress changes figures reproduced in this study based on Micklethwaite and Cox (2006) to show the importance of choosing appropriate types of optimised faults. A. shows combined-slip static stress change resolved on optimised strike-slip faults. This is the result achieved in the original study B. shows the same combined-slip static stress change but resolved on thrust faults. There is a significant difference between the Coulomb stresses calculated in the two figures. Their inputs were identical except for the type of receiver faults, which illustrates the importance of correctly interpreting which faults are present in the study area.

The benchmarking process has raised important considerations for creating an optimised workflow. Calculations for Coulomb 3.3's 'optimally oriented faults' run an exceedingly slow search through all orientations (dip and strike) of faults within the grid, which could take upwards of 24 hours to complete on an average workstation, particularly at resolutions of 100m in search areas spanning tens of kilometres. An

appropriate choice of specified receiver faults based on regional stress saves significant processing time.

The colour scheme for representing Coulomb stress changes has a significant effect on the clarity of the result. For example, calculating Coulomb stresses between the range of 2 and -2 bars (Micklethwaite and Cox 2006) with a colourbar that grades through blue-white-green at the 0 mark-to red at 2 is potentially less clear than one which puts white at the centre when glancing at figures. The effect of this is demonstrated in Figure 2.5. As 0.5 bar of elevated Coulomb stress is considered to be enough to correlate to increased aftershock incidence (King et al. 1994), the clarity of the colour scheme is significant. Clarity in this area is also important when considering some readers may be colour blind and read gradation trends more easily than specific colours.
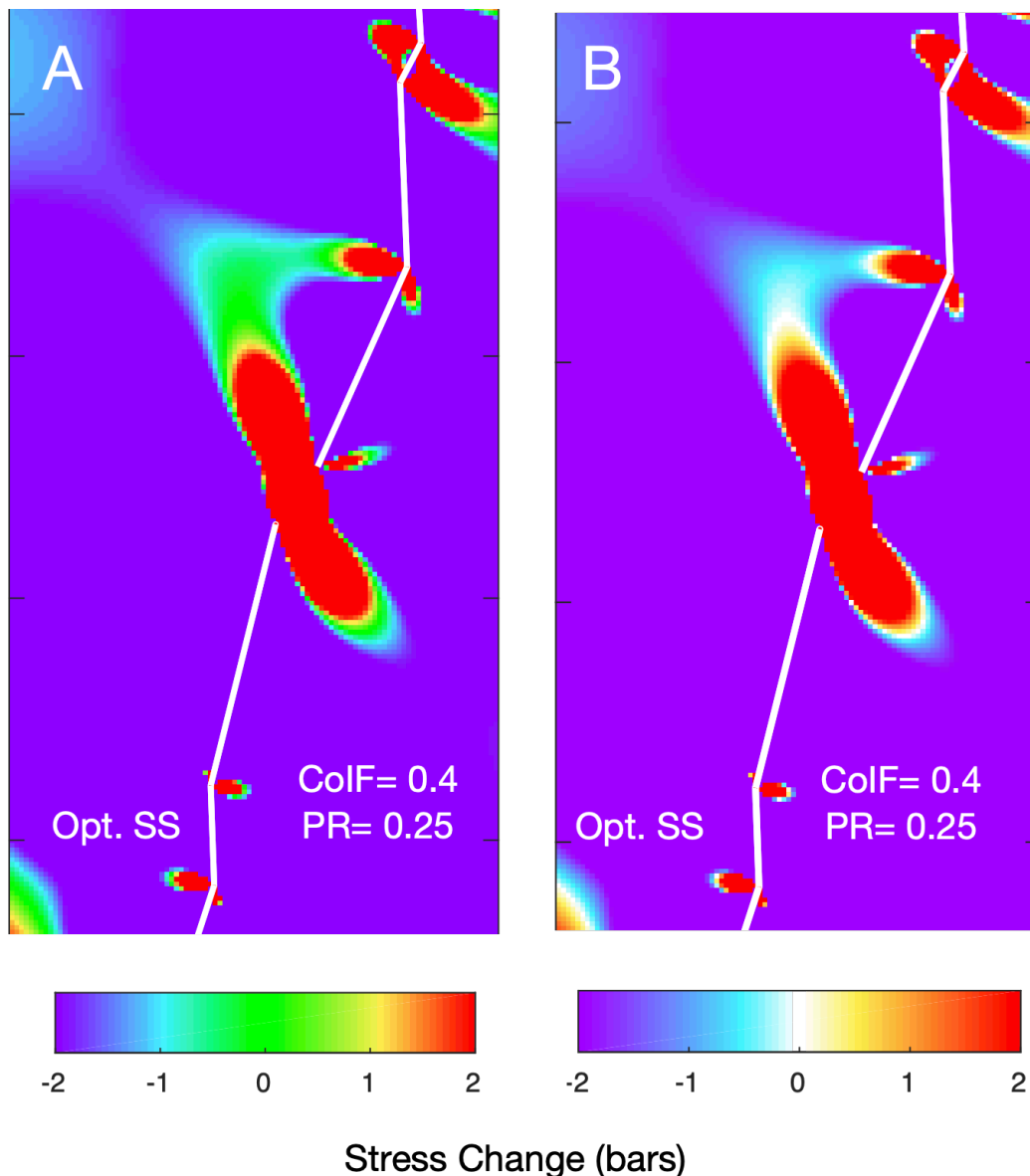
Figure 2.5: A comparison of colourbar gradient choices, showing the impact of choosing appropriate gradient settings. A. A reproduction using the original colourbar of (Micklethwaite and Cox 2006) *with a green value for 0 bars. B. An altered colour bar using white as the 0 bar value.*

2.7 Conclusions

This chapter establishes that application of Coulomb 3.3 is accurate for subsequent modelling of Obuasi and highlights the need for clarity for published literature to be replicable. An acceptable replication of an original Micklethwaite and Cox (2006) figure has been achieved, however the process suggests that research in this field

should include details of fault geometry, rock mechanics, regional stress, slip event and inputs specific to Coulomb 3.3 such as grid spacing, calculation depth and receiver fault type. The most appropriate way to achieve this is by including an input file as supplementary data, which eliminates doubt on parameters and provides exact geometry. An efficient and accurate workflow has been set, including choosing appropriate receiver faults for figures and colourbar gradations which allow for the clearest possible interpretations.

Chapter 3.

Representing Curvature with Point Sources in Coulomb 3.3

3.1 Introduction

Modelling slip on faults in Coulomb 3.3 requires a seismic source fault, which imparts stress due to a slip. Each user-defined fault in Coulomb 3.3 must be a rectangular surface of constant dip. This format is a constraint from the design of the software package, and makes the program simpler to input models for, an alternative being the more complex triangular mesh (e.g. Meade 2007). Multiple rectangular planes can be added to a model with or without slips meaning a slip event can be modelled using multiple source faults to better represent the real fault geometry. These rectangular planes must have horizontal top and bottom edges.

These geometric constraints result in under- and overlapping when using multiple planes to represent curvature of a larger fault or fault system. This effect is illustrated in Figure 3.1, which shows a detailed reconstruction of a section of the Obuasi fault system, including along strike and down dip fault curvature. Overlap and underlap is present here where fault panels do not join continuously. Because it is well established that variable geometry along-strike on faults in Coulomb models is important to accuracy in results (e.g. Parsons et al. 1999; Steacy et al. 2005; Bie and Ryder 2014; Mildon et al. 2016; Mildon et al. 2019), considering the level of simplification in representation of the Obuasi fault system with respect to curvature and overlap is important. This chapter aims to investigate how best to approach this challenge using idealised control models, and to establish which method of modelling available in Coulomb 3.3 is most appropriate for modelling Obuasi.
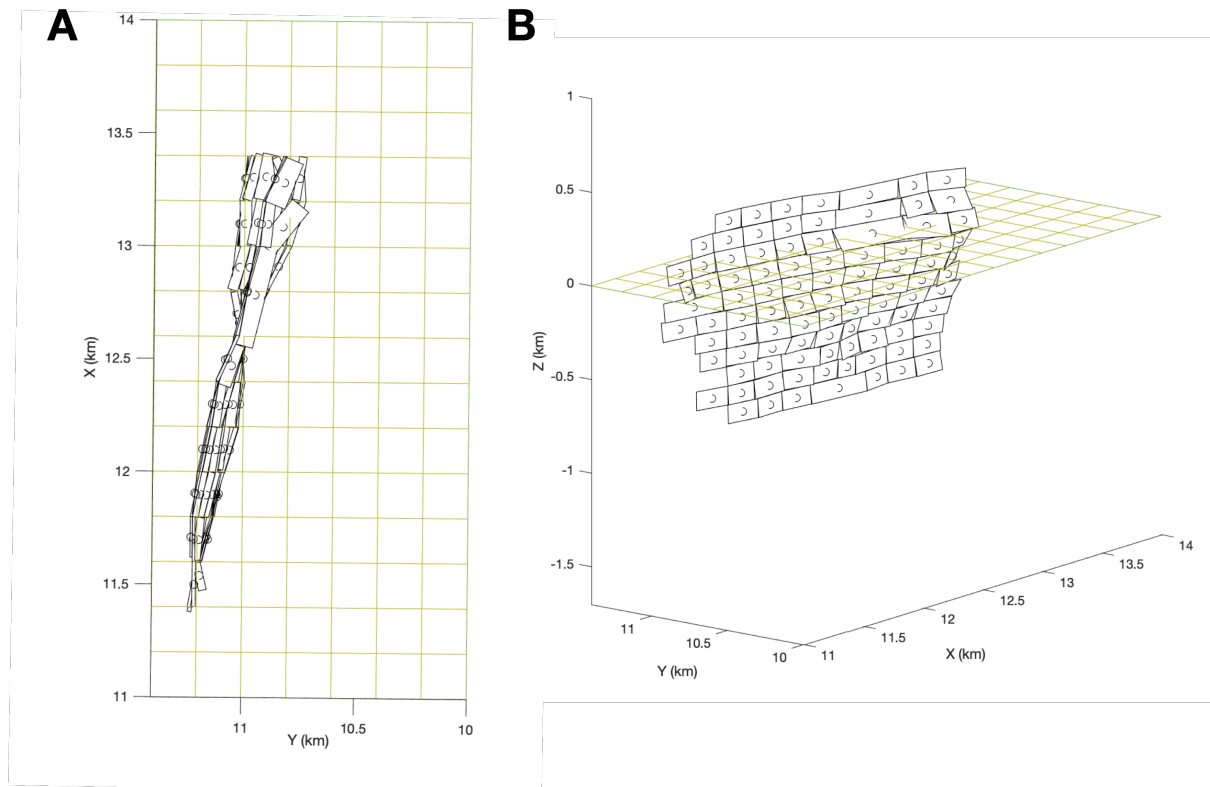
Figure 3.1: A curved section of the Obuasi fault represented in Coulomb 3.3 using rectangular fault element planes viewed from above (A) and oblique (B). Overlap and underlap occur on the edges of the fault panels.

Coulomb 3.3 can model events of uniform slip across an entire plane, a method called Kode 100 in the manual (Toda et al. 2011a), and can alternatively model slip events as a point source, located at the centre of the assigned plane (Kode 400). The vector of the point source is defined by the strike, dip, and rake values of the plane it is central to. Other Kode functionalities, discussed in Chapter 2, are not appropriate in this application. In the user guide to Coulomb (Toda et al. 2011a), it is suggested that point shear sources, Kode 400, can be used to model curved faults (Figure 3.2). Because the design of Coulomb 3.3 uses rectangular input planes, Toda et al. (2011a) state that modelling using point sources could solve the issue of under/overlap causing stress anomalies.
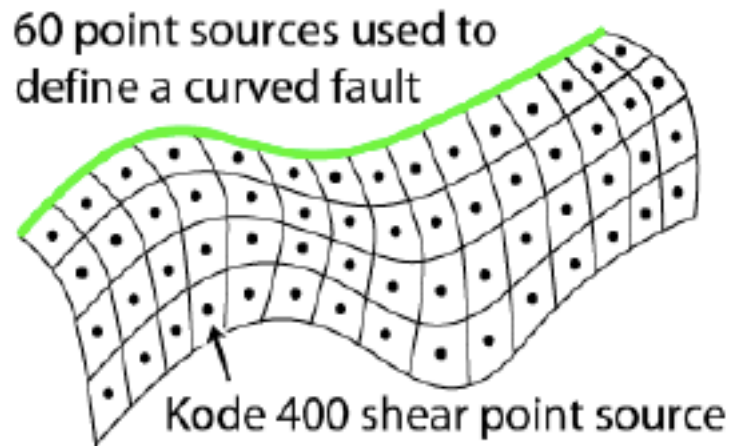
Figure 3.2: Using point sources to model curved fault surfaces in Coulomb 3.3
Source: Toda et al. (2011)

To address potential underlap/overlap of variable fault geometries, Mildon et al. (2016) conducted a test which is included as a supplementary file (Figure 3.3). This showed that spurious stress changes are observed above the fault when fault elements in Coulomb 3.4 (a later version available only to the researchers) under or overlap. The final methodology chosen by Mildon et al. (2016) meant underlap and overlap had no impact on the study, because the spurious stress signals were not encountered when resolving stress directly on receiver faults. However, in this thesis stress will be resolved on optimised faults, meaning the spurious stresses identified by Mildon et al. (2016) above fault elements could impact CST results modelled at Obuasi. The tests for Mildon et al. (2016) were set up using idealised normal faults and modelled using Kode 100 (whole-fault movements). Mildon et al. (2016) also conclude that stresses away from the modelled faults are unaffected by the anomalous values observed at over/underlaps.
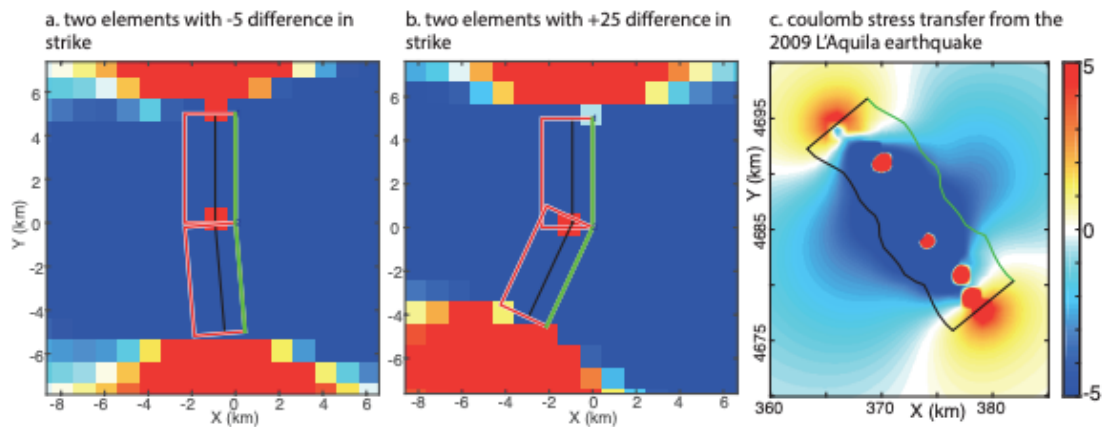
Figure 3.3: Mildon et al. (2016) *test file results. Original caption reads: "Testing for spurious stress signals due to underlap/overlap of adjacent elements. The spurious stress manifests as a red patch directly above the area of underlap/overlap. (a) Elements with a difference in strike of -5 creating underlap with a single spurious stress value. (b) Elements with a difference in strike of +25 creating overlap with a single spurious stress value. (c) Paganica (source) fault for the L'Aquila 2009 event, 374 elements (not shown individually). Green line is the surface projection, the black line is the depth extent. Spurious positive stress patches are seen directly above the fault, but the far field stress is comparable to a planar model. Hence the spurious stress signals do not affect the far field stress field and will not affect the Coulomb stress resolved directly onto receiver faults." Source:* Mildon et al. (2016) *supplementary file.*

Using calculations which apply uniform slip distribution across the fault, a whole fault movement, is well established in literature (e.g. Chinnery 1963; King et al. 1994), This approach has produced positive results (e.g. Cox and Ruming 2004; Micklethwaite and Cox 2004; Micklethwaite and Cox 2006), particularly in the context of fault stepovers, where stress is focused into dilational jog structures.

Modelling Coulomb stress from point sources is less common in published literature, relating mostly to small magnitude induced seismicity (e.g. Orlecka-Sikora 2010; Kozłowska et al. 2015). However, Kozłowska et al. (2015) suggest in the context of small-magnitude induced seismicity, point source modelling performs better than whole-fault modelling.

With the aim of establishing the most appropriate settings in Coulomb 3.3 for this thesis and to illustrate the direct effect of modelling using Kode 400 vs Kode 100, a control model without under or overlap was constructed using a single idealised fault. This is modelled as a whole fault using Kode 100 and 400, and again as a series of five adjacent fault elements occupying the same space as the original idealised fault, to imitate the patch-method of Mildon et al. (2016). Once the effect of point source modelling was established on the control, whether models using point sources could eliminate the effects of underlaps and overlaps and still accurately model slip events was investigated. To achieve this the Kode 100 results of the supplementary investigation of Mildon et al. (2016) have been replicated and contrasted with original CST modelling using Kode 400. This consolidates the benchmarking achieved in Chapter 2 in addition to illustrating the impact of using Kode 400 point source modelling.

3.2 Methods

Modelling using Kode 100 is conducted using the method described in Chapter 2, inputting source faults with a slip vector. Modelling using a Kode 400 point source uses potency (dyne cm^3) rather than slip (m), as point sources have no area. The Kode 400 input file is otherwise unchanged.

$$slip\ potency = \frac{seismic\ moment}{shear\ modulus}$$

Slip potency, or geometric moment, can be derived using the seismic moment, which Coulomb 3.3 automatically calculates for a Kode 100 input using fault area A, slip distance D, Young Modulus E and Poisson's Ratio PR.

Shear modulus G is calculated using the Young Modulus and Poisson's Ratio:
$$G = \frac{E}{2(1 + PR)}$$

Seismic moment Mo is derived using fault area, slip distance and shear modulus:
$$M_o = A \times D \times G$$

Some of the parameters for Coulomb modelling introduced in Chapter 2 are available in text (Mildon et al. 2016), but fault geometries and calculation depth were interpreted from the output figure. Regional stress orientation is not required in this setup, as Coulomb stresses are calculated using the automatic specified receiver fault function in Coulomb 3.3. The coefficient of internal friction is provided, but other rock mechanics data was inferred, using data from the Coulomb user manual (Toda et al. 2011a)

3.2.1 Kode 100/400 Control

For testing the effect of Kode 100 compared to Kode 400 a single idealised 10km long fault extending to 5km depth was constructed, with strike/dip/rake of 180°/65°/-90° after Aki and Richards (1980). This is based on the original test fault of Mildon et al. (2016) and is shown projected in 3D in Figure 3.4. A typical internal friction coefficient of 0.4 (King et al. 1994; Mildon et al. 2016) has been chosen for this experiment (Appendix I).
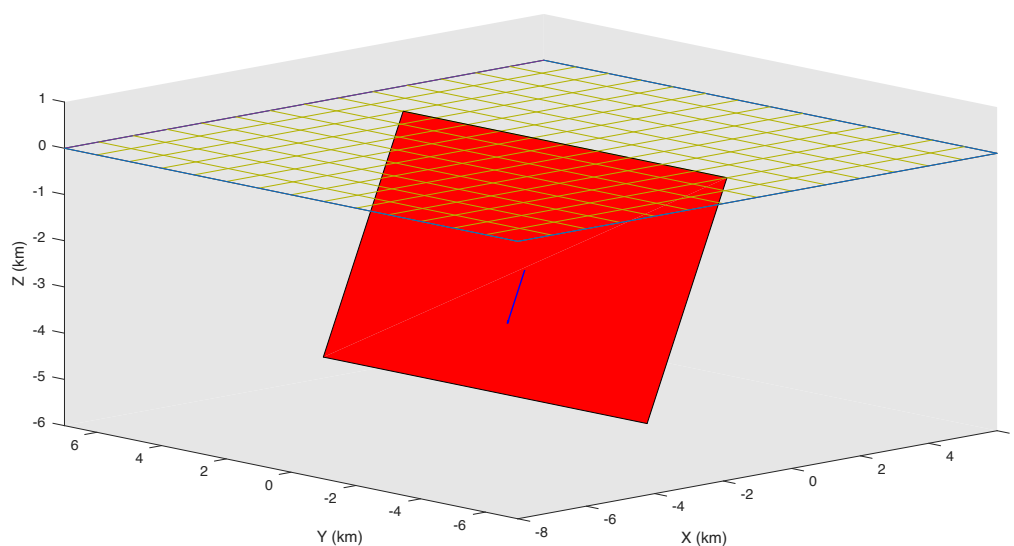
Figure 3.4: A single 10km fault element dipping 65° in Coulomb 3.3.

Rock mechanics estimates used are Young's Modulus E = 8x10^5 bars or 80 GPa and Poisson's ratio = 0.25, which gives a shear modulus of 32 GPa, 3.2x10^5 bars or

3.2x10^{11} dyne cm^{-2}.This is incorrectly calculated in the Coulomb 3.3 user manual as 3.3x10^{11} dyne cm^{-2} (Toda et al. 2011a), which is the value of shear modulus used by King et al. (1994) on the Landers slip. A seismic moment of 3.53x10^{25} dyne-cm is calculated within Coulomb for a 2m normal slip on the 10km long fault element using Kode 100. Using a shear modulus value of 3.3x10^{11} dyne cm^{-2} (King et al. 1994), slip potency for this fault represented by a point source is (-)1.07x10^8 m^3, a negative value used to represent normal slip in Coulomb 3.3.

To demonstrate the effect of representing one main fault with multiple point sources in the manner described by the manual, (Figure 3.2; Toda et al. 2011a), this 10km fault element is split into 5 adjacent 2km long elements, each slipping with 2m of normal slip. In Kode 400 the slip potency for each element is 2.14x10^7 m^3.

3.2.2 Underlap and overlap in Kode 100/400

The supplementary investigation of Mildon et al. (2016) shown in Figure 3.3 was replicated by combining interpretations of the graphical output and information provided in text. The two setups both comprise two 5km long, 5km depth fault elements, modelled at 2km depth. One fault in each was offset, by -5° to create underlap in the first and by +25° to create overlap in the second.

Numerical details for rock mechanics input parameters, regional stress fields and fault geometries have not been provided in the supplementary document of Mildon et al. (2016), but estimations for these values were made using the graphical output, investigative Coulomb models, and the assumption that calculations for stress were resolved on specified receiver faults, which are calculated independently from an assigned regional stress. It was found that the specific x-y axes start and end points made a significant impact on the resulting figures due to the calculation resolution being defined by the grid spacing. Offsetting the x-y start points from those provided in the original figures resulted in different stress patterns being generated. A normal slip of 2m on these models at a calculation depth of 2km, resolved on Coulomb's default specified faults was obtained through trial and improvement.

For this chapter the colourbar used in Mildon et al. (2016) has been retained, reproduced using ImageJ to extrapolate RGB decimal codes. Because the original figure (Figure 3.4) applied a colourbar scale range from -5 to 5 bars, this has also been retained.

3.3 Results

3.3.1 Kode 100/400 Control

The Coulomb stress transfers calculated on the control model setups are shown in Figure 3.5. Changing the type of modelling has a clear impact on the patterns of CST calculated, shown in the comparison of Figure 3.5A and B, and the comparison of 3.5C and D. Positive CST is observed at the margins of the fault when modelling a whole fault movement, e.g. 3.5A, 3.5C, but is seen from the centre of the fault when using a point source, creating patterns similar to those of Coulomb modelling of normal faults made using earthquake point source hypocentres (e.g. Nostro et al. 2005). The spatial pattern of the stress is consistent across both modelling types.
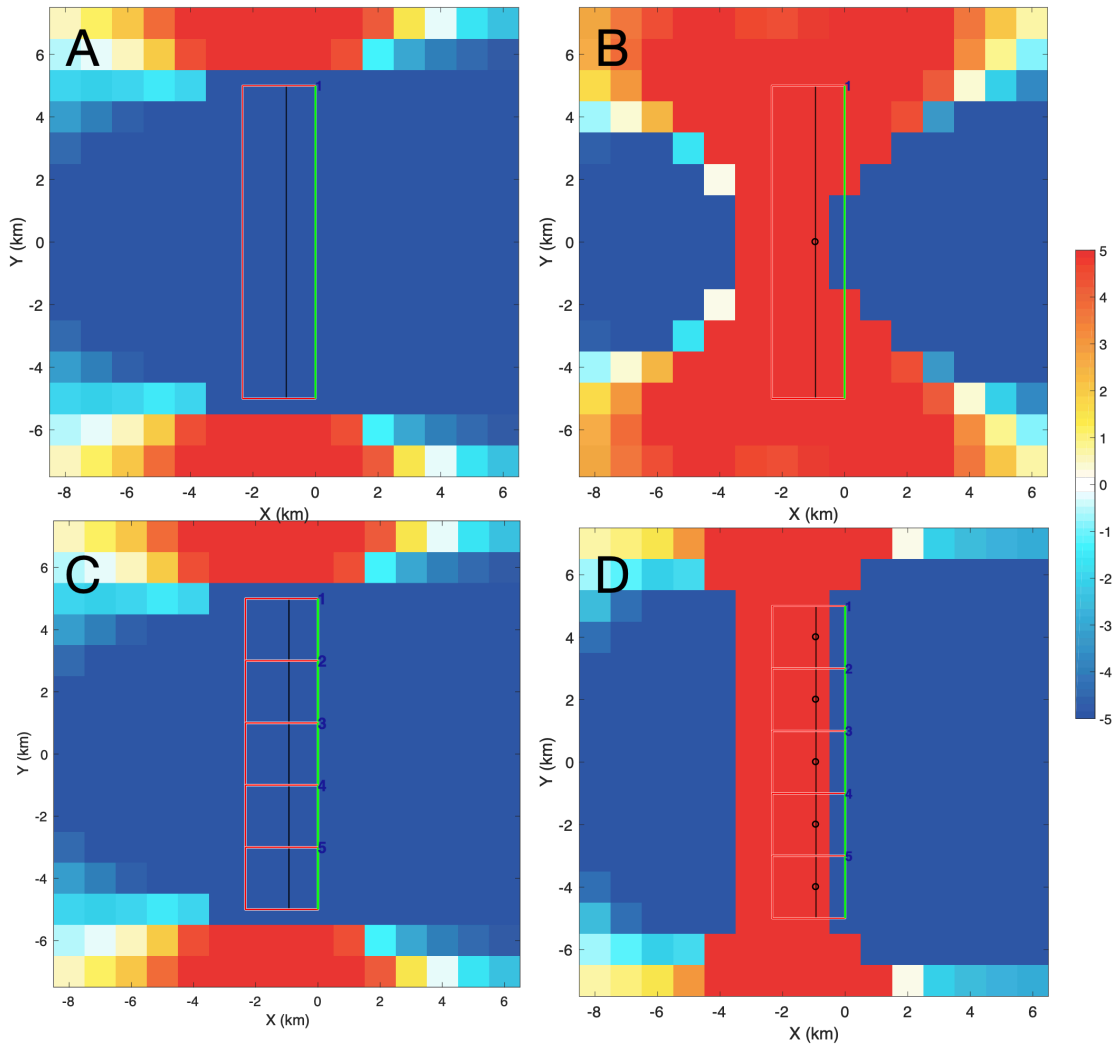
Figure 3.5: A control fault illustrating the difference between modelling Coulomb stress transfer after a 2m slip on a 10km long, 5km depth normal fault using Kode 100 and 400 at 2km depth. A. 1 fault element, Kode 100. B. 1 fault element, Kode 400. C. 5 fault elements representing the original single fault, Kode 100. D. 5 fault elements, Kode 400. C. and D. illustrate how Coulomb stresses can be calculated when faults are split into smaller elements, which will be used when modelling the complete Obuasi fault. Coulomb stress in bars.

Splitting the fault into adjacent panels with no curvature has no effect on the calculated CST when modelling using Kode 100. The Coulomb stresses calculated in Figure 3.5A are identical to those of 3.5C. By contrast, splitting one point source

representing a 10km fault into 5 smaller point sources returns different CST patterns after a slip event, illustrated in 3.5B and 3.5D.

3.3.2 Underlap and overlap in Kode 100/400

A close approximation of the model demonstrating the anomalous values produced by underlapping and overlapping faults of Mildon et al. (2016) was reached (Figure 3.6). The CST values calculated in this study do not exactly match the Mildon et al. original, however appear very close in distribution and magnitude.
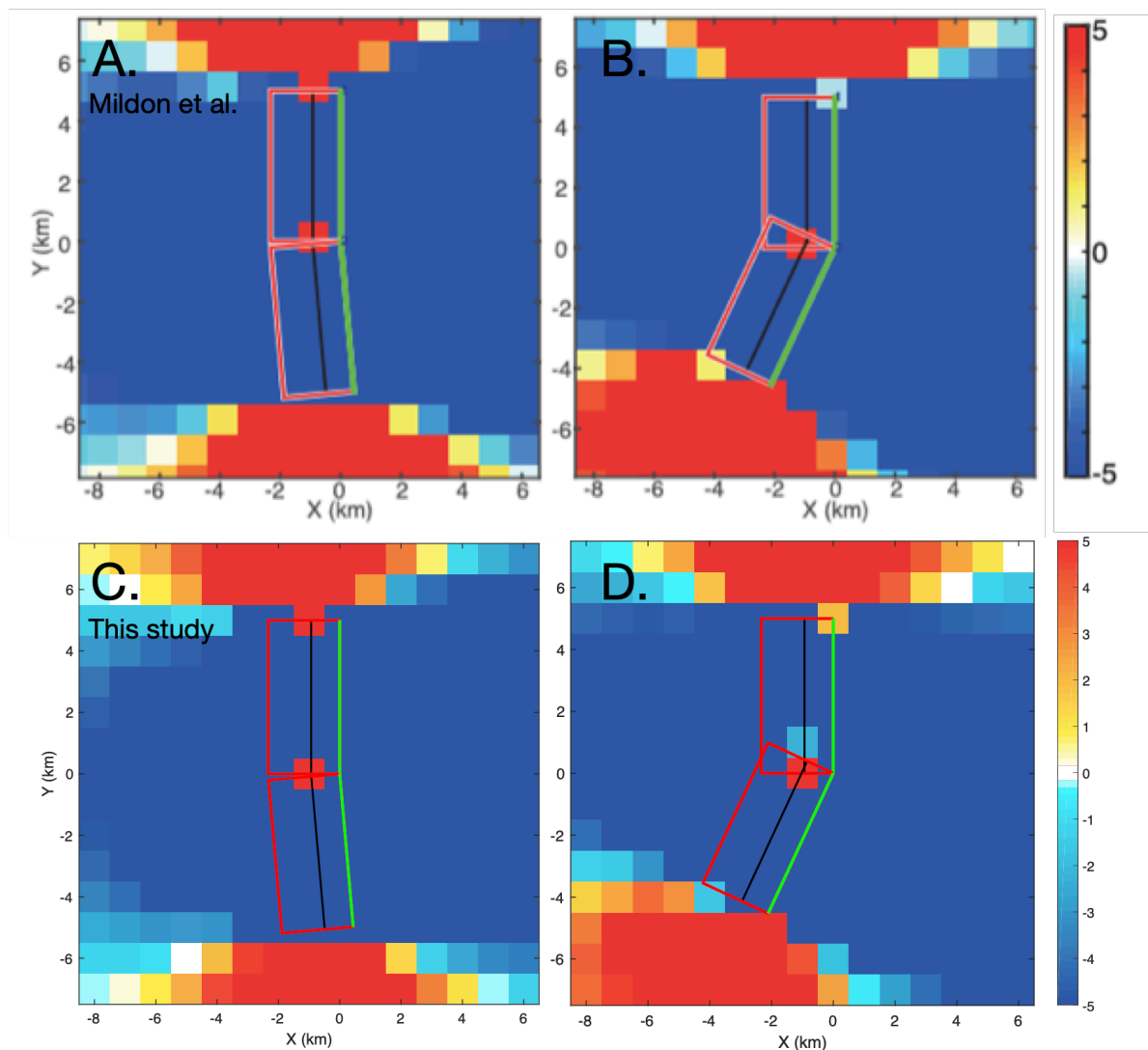
Figure 3.6: A comparison of the Mildon et al. (2016) original results and those achieved replicating the model using the available values in this study. A/B: Mildon et al. original results. C/D: This study. Coulomb stress in bars.

Critically, the anomalous values that appear directly on the overlap and underlaps noted in the original study are present in the replicated model, allowing for comparison with Kode 400 modelling (Figure 3.7).
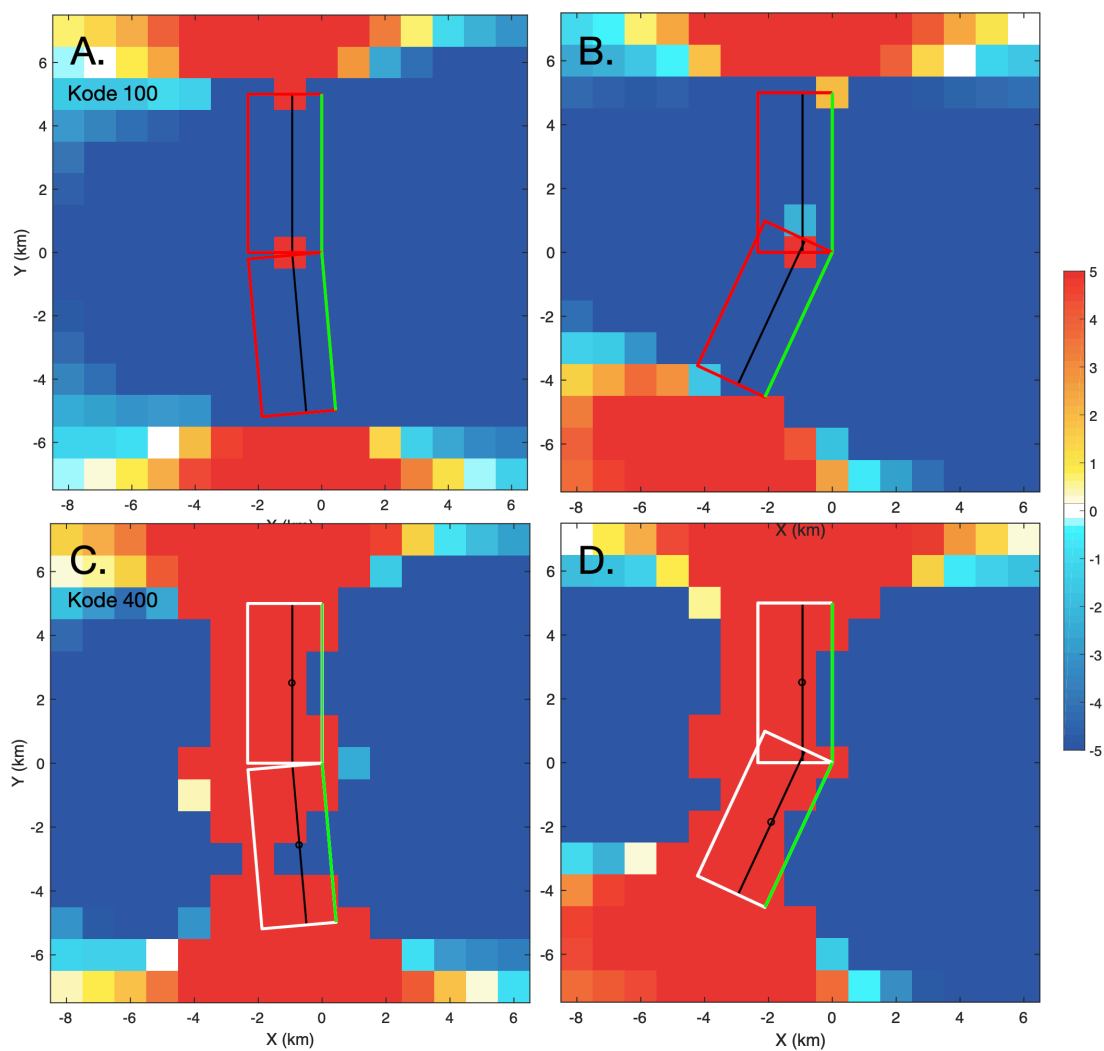
Figure 3.7: A comparison of modelling underlapping and overlapping faults using Kode 100 (A,B) and 400 (C,D). The small anomalous values identified using Kode 100 are replaced larger regions of positive Coulomb stress centres around the point sources representing faults in Kode 400. Coulomb stress in bars.

A clear difference in the calculation of CST is evident when using Kode 400, with much larger regions of positive stress being calculated on and around the fault, centred on the point sources. The stresses further away from the modelled faults

(>1km from the fault planes) is however similar for both Kode 100 and Kode 400 calculations.

3.4 Discussion

The idealised modelling conducted in this chapter shows that using whole fault movements or point sources can provide significantly different calculations of CST, particularly in the rock mass proximal to the source fault. The anomalous values which appear when faults overlap in Kode 100 were shown to be replaced by larger zones of Coulomb stress when modelled using point sources. The anomalous values would not likely arise from a continuous curved fault, however curvature will impact the distribution of stress in the rock. As shown in the control model, Figure 3.5, point sources are treated in Coulomb 3.3 as individual seismic hypocentres, transferring stress to the surrounding rock mass, resulting in positive stresses calculated directly on the fault. By contrast, joined fault elements in Kode 100 are treated as one continuous fault, meaning small underlaps and overlaps only generate small, isolated positive CST values proximal to the fault, which have been dismissed previously as anomalous (Mildon et al. 2016).

Natural faulting contains slip gradients, which are typically linear (Scholz and Lawler 2004), tapering to 0 at the fault edges .Therefore, real world faulting is likely to lie somewhere between the Kode 100 and Kode 400 styles. Coulomb 3.3 has an additional functionality to add slip taper into a Kode 100 based model, which is shown in Figure 3.8. When considering real world faulting, using nested tapered fault elements is likely the closest representation available in Coulomb 3.3. However, due to the method by which tapered slips are calculated, tapering cannot be calculated for a model with multiple source faults, such as the models used in Cox and Ruming (2004), Micklethwaite and Cox (2004), and Micklethwaite and Cox (2006), or the models which will be applied for Obuasi. Manually calculating tapered slips would be possible but impractical, defeating the aim of providing rapid and easy to produce modelling for exploration.
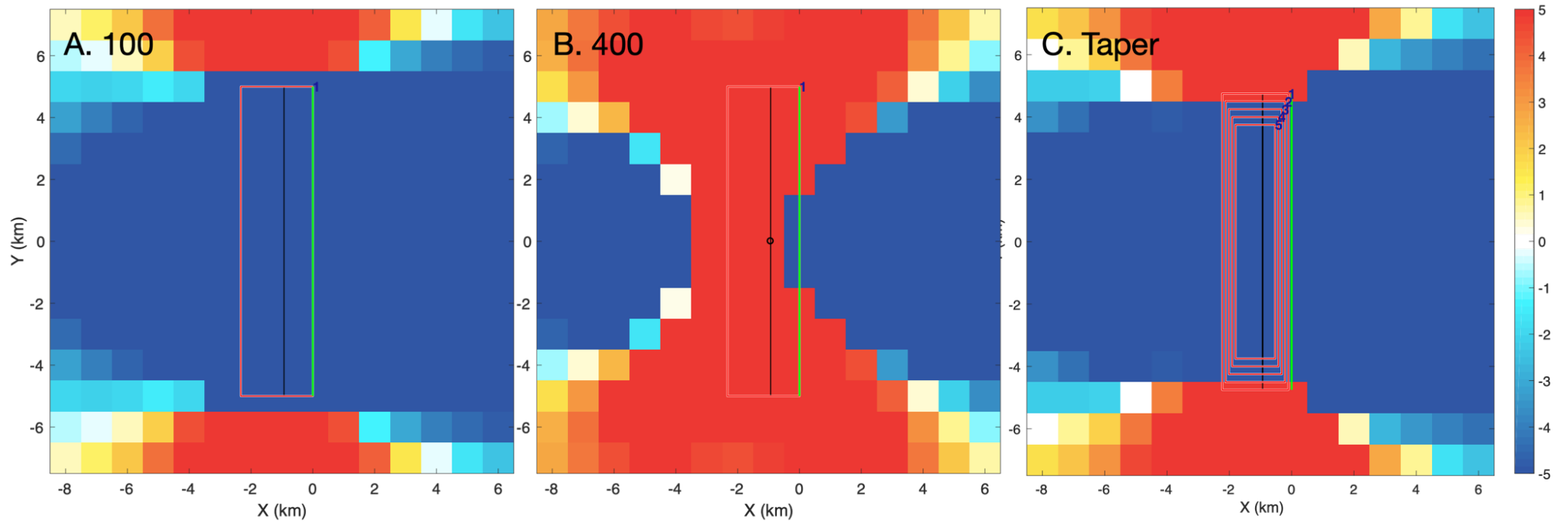
Figure 3.8: The tapered slip calculation feature of Coulomb 3.3. A. Kode 100 10km normal fault modelled at 2km depth. B. Kode 400 10km fault modelled at 2km depth. C. Tapered slip 10km fault, with fault subdivided into 5 nested panels. Total moment is equal to those of A and B. Coulomb stress measured in bars.

The stresses >1km away from the faults in each of the calculations shown in this chapter remains generally uniform, with positive CST north and south, and negative CST east and west. The tapered slip example shown in Figure 3.8 more closely resembles the results of the Kode 100 model than the Kode 400. In the context of further modelling in this project, modelling at scales where the stress over the fault has less impact on predicting zones of aftershocks in stepovers and underexplored off-fault areas, Kode 100 modelling is the more appropriate choice, particularly as modelling Obuasi involves large scale hypothetical ancient slip events, without available data from the site defining slip gradients.

These results also suggest that modelling using Kode 400 does not provide a direct solution to modelling curved faults in the manner described by the manual for the application required in this project. Rather than clearing up potentially anomalous values, applying the point source method to a complex surface such as the example presented in Figure 3.1 models a series of isolated hypocentres, which is further from real-world fault mechanics than the simplification provided by whole-fault movements.

3.5 Conclusions

The most comparable style of modelling to real-world faulting is applying tapered slip to a Kode 100 model. However this is impractical to use modelling Obuasi or in wider application as it cannot be applied to multiple fault planes automatically, requiring complex and time consuming manual calculation instead. Kode 100 modelling creates small anomalous values which may not be representative of a continuous curvature but are a closer approximation than representing a curved plane with multiple minor hypocentres, Kode 400. Stress calculations away from the fault system are generally unaffected by which method is used, but the choice remains important because mineralisation tends to be closely associated with fault systems. For the remainder of this investigation, Kode 100 calculation will be applied.

Chapter 4.

Mineralised Stepovers: The Ashanti and Insintsium Fissures

4.1 Introduction

A preliminary investigation into the application of the stress-transfer technique at Obuasi is conducted in this chapter, aiming to test whether results for a small, late-stage dilational jog within the Obuasi fault system conform to expected results of stepover based modelling (e.g. Cox and Ruming 2004; Micklethwaite and Cox 2004; Micklethwaite and Cox 2006). The Ashanti and Insintsium Fissures in the north of the deposit are selected for this purpose.

At the Obuasi deposit there are two principal generations of large, mineralised faults and shear zones. These are earlier $D2_{Ob}$ thrust faults and later $D5_{Ob}$ sinistral strike-slip faults (Allibone et al. 2002; Oliver et al. 2020). The $D2_{Ob}$ thrusts generally exhibit a sinistral strike-slip $D5_{Ob}$ re-activation. Many smaller low displacement faults and tension veins are associated with these deposit-scale structures, and host much of the mineralisation. These are unnamed and absent on maps or sections, but are identified in Allibone et al. (2002) and are represented by the optimised receiver faults in stress transfer modelling conducted in this chapter. $D2_{Ob}$ is accepted to have occurred under a NW-SE contractional regime, which then evolved to the transpressional NNW-SSE regime for $D5_{Ob}$. Mineralisation timing is debated (Oberthur et al. 1995; Allibone et al. 2002; Fougerouse et al. 2017), but gold is generally interpreted to have been initially emplaced during $D2_{Ob}$ with either a new depositional event during $D5_{Ob}$, remobilisation of the original gold during the later phase, or some combination of the two.

Most of the mineralised fissures at the Obuasi mine were formed as thrusts in $D2_{Ob}$ and reactivated later; the Ashanti fissure is unusual in that it was formed during $D5_{Ob}$ and was principally strike-slip (Allibone et al. 2002; Oliver et al. 2020). It also contains two mineralised, hard-linked, under-stepping dilational jogs, mapped and

defined by Allibone et al. (2002). These conditions, as established in early theory (Sibson 1987) are well suited to mineralising fluids from aftershock sequence driven permeability. Coseismic Coulomb stress transfer has been shown to exert a controlling influence on the shaping of hard linkages (Hodge et al. 2018).

Isolating the step-overs of the Ashanti fissure (Allibone et al. 2002) provides a single deformation stage test of the aftershock-driven mineralisation distribution hypothesis. This was achieved by measuring surface traces and cross sections from Oliver et al. (2020) and simplifying the fault geometries to rectangular elements. This closely emulates the model-building of previous Coulomb stress transfer models (e.g. Cox and Ruming 2004; Micklethwaite and Cox 2004; Micklethwaite and Cox 2006). Micklethwaite et al. (2016) establish that underlapping stepovers analogous to those on the Ashanti Fissure in the Yilgarn Craton host greater quantities of gold than overlapping stepovers. Coulomb modelling strongly suggests that the extent of damage and therefore permeability enhancement across an underlapping stepover is much greater than at overlapping stepovers, making them particularly favourable to aftershock-driven permeability (Micklethwaite 2013). This chapter models the occurrence of this kind of damage zone at the Ashanti Fissure and neighbouring Insintsium Fissure stepovers.

4.2 Methods

The Ashanti and Insintsium Fissures are two mineralised subvertical sinistral strike-slip faults at the northern end of the mineralised Obuasi fault system, with an approximately 1.5km long mineralised segment, although the Ashanti fissure extends further north of the deposit. The mapped extent of the Insintsium Fissure (Oliver et al. 2020) is small, approximately 500m along strike, however its linkage to the Ashanti Fissure hosts significant gold (Figure 4.1). These faults have been simplified to sub-vertical rectangular planes, dipping 88° SE, consistent with cross-sectional geometries supplied by Oliver et al. (2020). The geometry was not simplified to vertical faults in order to show the impact of the reverse component. Vertical Coulomb models do not show any Coulomb stress change associated with reverse

slip. The hard linkage shown on maps for these stepovers has been omitted following the methods of Micklethwaite and Cox (2006).

A NNW trending compressional regional stress, with sub-horizontal $\sigma1$ and $\sigma3$ has been used after Fougerouse et al. (2017), with correction for Obuasi Mine Grid.
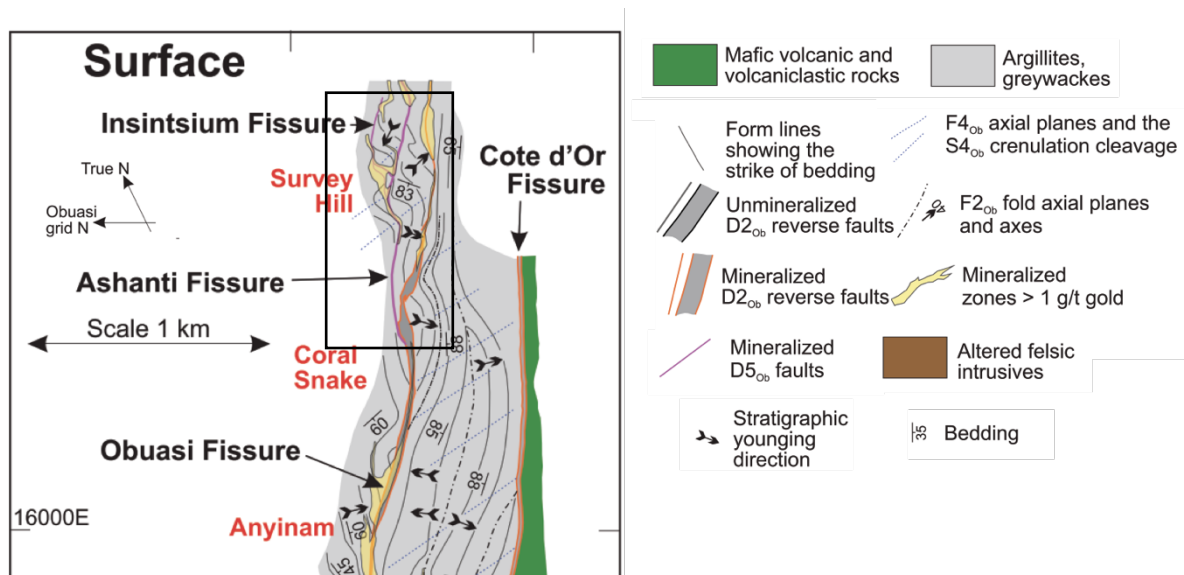
Figure 4.1: Ashanti and Insintsium Fissure surface traces at northern end of Obuasi Fault system, with mineralised zones shown as polygon outlines.
Two stepover bends can be observed, one on the Ashanti Fissure and another on the smaller Insintsium. Mineralisation appears to be focused on these locations, particularly where the Ashanti Fissure links to the Insintsium. The modelled area is indicated in black.
Edited after Oliver et al. (2020)*.*

Curvature along strike has been represented by 3 pivot points along the length of the Ashanti fissure. Representing curvature in fault traces by introducing strike changes is important (Mildon et al. 2016; Mildon et al. 2019), but can introduce potentially spurious values near to the fault. The Insintsium Fissure, which does not show much strike variability, has been represented as a single plane. All planes begin at 200m above sea level and extend down to -250m, based on cross sections (Oliver et al. 2020). Calculation depth is set at -100m, which is mineralised on the Ashanti fissure (Allibone et al. 2002; Oliver et al. 2020). CST results vary minimally with depth in models with subvertical strike-slip faults such as this.

The first stage of experimentation models a single sinistral movement on all of the fault elements, using the combined-slip method described by Micklethwaite and Cox (2006). Fault-scaling relationships (e.g. Torabi and Berg 2011) have been used to decide on 0.01m of sinistral movement of the fault system, amounting to an Mw 3.67 event. This is resolved as CST using Kode 100 onto optimised strike-slip, thrust and normal faults, as $D5_{Ob}$ thrust and normal faulting associated with the Ashanti Fault is recorded by Allibone et al. (2002) in addition to the predominant strike-slip regime. The resolution is gridded into 100m sections. For the coefficient of internal friction, a value of 0.4 is recommended in the Coulomb user guide and by Micklethwaite and Cox (2006) for applications in fluid saturated rock. To investigate the effect of the coefficient of internal friction on CST, the experimental setup for optimised strike-slip faults is repeated three times, with values of 0.2, 0.4 and 0.8, representing the typical outside bounds for rocks after Byerlee (1978).. The Coulomb developers mention that they apply coefficients of internal friction of 0.2 for low friction major transform faults and 0.8 for continental thrust faults, meaning the ranges shown in this chapter cover extreme cases for illustration purposes. The impact of fluid saturation on this model is ignored, as Coulomb 3.3 cannot account for fluid pressure, and data is not available in literature for Obuasi.

Gently SW plunging slickenlines identified by Allibone et al. (2002) on NE striking late stage sinistral faults such as the Ashanti Fissure imply that movements were largely strike slip, with a small reverse dip slip component. To investigate the effect of combination strike and dip slip fault movements, a small reverse component was added, as an additional 10% of the strike slip motion.

4.3 Results

Results for a sinistral combined strike-slip movement, resolved on optimised strike-slip, thrust and normal faults (Figure 4.2) show a concentrated zone of positive Coulomb stress appears in the centre of both stepovers, combining to form a larger area of general positive Coulomb stress, surrounded by shadows of negative Coulomb stress. Resolving using different receiver fault styles does result in minor variation in the concentration of positive CST, however this is consistently focused across the stepover in each.
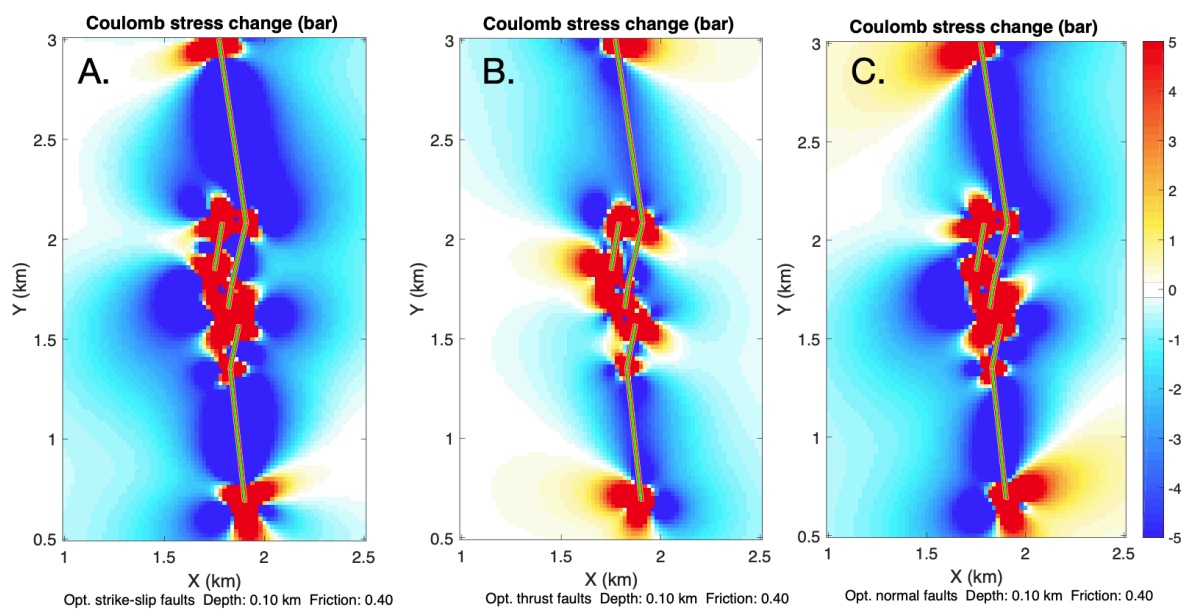
Figure 4.2: The calculated Coulomb stress transfer for a 0.01m sinistral slip on the Ashanti and Insintsium Fissures, resolved on optimised strike slip (A.), thrust (B.) and normal (C.) faults. In all cases, a concentration of positive Coulomb stress is focused at the stepover zones between the Ashanti and Insintsium Fissures, associated with fault curvature points and terminations. Young Modulus 8MPa, NNW contractional stress regime.

Pivot points along the faults show areas of positive Coulomb stress in addition to those calculated at fault terminations. In the central region, the curvature represented by these pivot points appears to contribute to the positive stress zone across the stepovers.
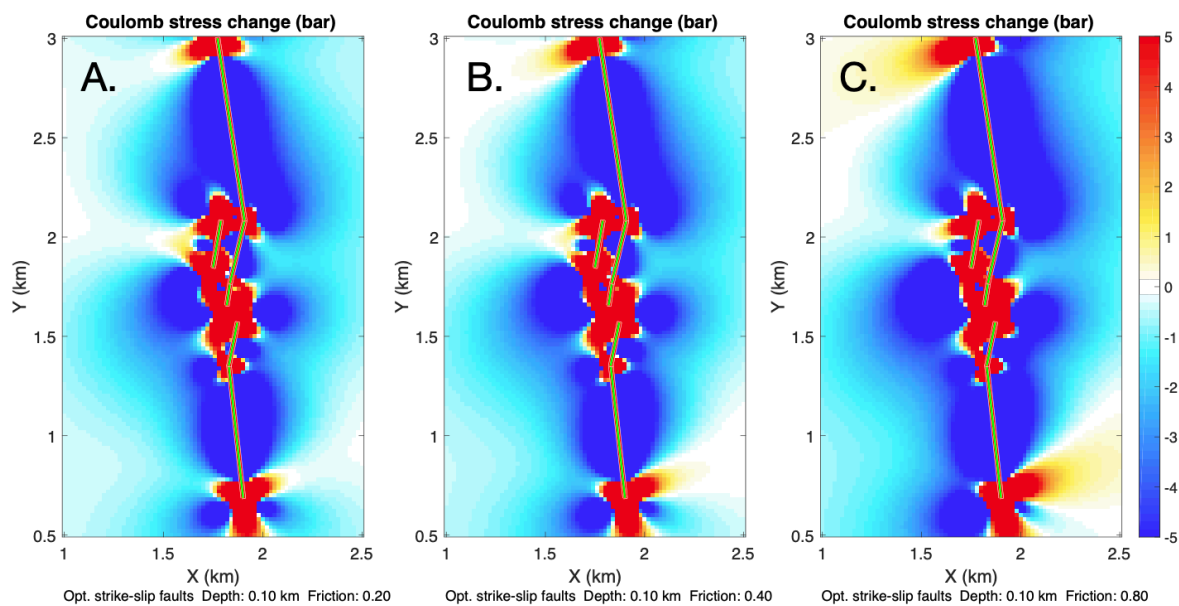
Figure 4.3: The effects of increasing the coefficient of internal friction within a model setup. (A.) 0.2, consistent with a low friction major transform. (B.) 0.4, a value consistent with a locally scaled strike-slip fault. (C.) 0.8, analogous to continental thrust faults. With increasing coefficient of internal friction, both positive and negative Coulomb stress changes are affected over a larger area, however the overall geometry remains similar.

Changing the coefficient of internal friction, Figure 4.3, affects the distribution of Coulomb stresses resolved, with Coulomb stresses being modelled with higher values at greater distances from the source faults as the friction coefficient increases, from Figure 3A to Figure 3C. The positive stress observed across the stepover zone is consistent regardless of coefficient of internal friction.

The result of adding a small component of reverse movement to this model has a limited impact on the stepover centred zone. The impact is noticeable in the effect of increasing Coulomb stress close to zero in the footwall when resolving for thrust faults and the hanging wall for normal faults.
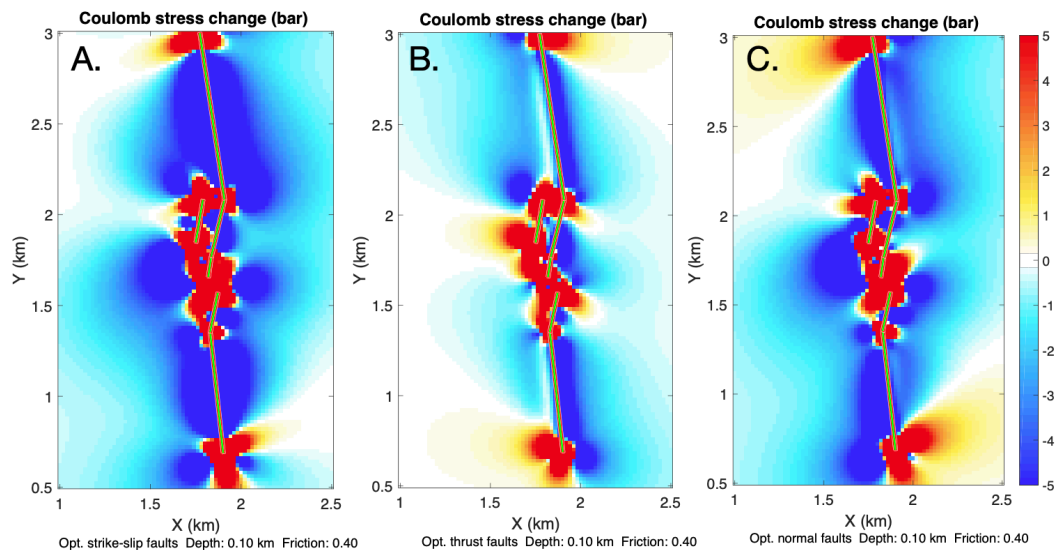
Figure 4.4: The calculated Coulomb stress transfer for a 0.01m sinistral, 0.001m reverse oblique slip on the Ashanti and Insintsium Fissures, resolved on optimised strike slip (A), thrust (B) and normal (C) faults. In all cases, a concentration very similar to the results of Fig 2. of positive Coulomb stress is focused at the stepover zones between the Ashanti and Insintsium Fissures, associated with fault curvature points and terminations. 4A. and 2A. appear almost identical, but stress patterns in the foot (B) hanging (C) walls are slightly different, where reductions to 0 in areas of previously negative Coulomb stress are visible in this figure. Young Modulus 8MPa, NNW contractional regime.

4.4 Discussion

The results achieved at Obuasi are comparable with previous work (e.g. Micklethwaite and Cox 2004; Micklethwaite and Cox 2006; Micklethwaite et al. 2016). The results suggest that for the late stage fluid emplacement, strike-slip $D5_{Ob}$ deformation and associated aftershock driven permeability was a first order control on fluid flow. This is a positive step towards modelling the larger extent of

mineralised fissures, suggesting that their $D5_{Ob}$ reactivation probably enabled fluid movement, regardless of whether this was new fluid or remobilised gold emplaced earlier. There is a correlation between the sketched high-grade mineralisation polygons seen in Figure 4.1 and areas of positive Coulomb stress from the static stress change calculations in Figure 4.2, regardless of which fault type the stresses have been resolved onto. Gold concentrations are greater in the centre of the stepover, consistent with seismically driven permeability enhancement. This implies that stepover geometry is an important control in the distribution of fluid flux at the Ashanti and Insintsium faults, (Sibson 1987; Micklethwaite 2013; Micklethwaite et al. 2016).

Simplifications to the fault geometry have been made for this model. All planes have the same constant dip, and curvature has been reduced to 3 changes in strike along the Ashanti fissure. This is consistent with the scale of simplification made in previous Coulomb stress transfer studies, in both economic (e.g. Micklethwaite and Cox 2006) and other studies (e.g. Mildon et al. 2016) where faults have variable strikes. Simplifying the fault geometry produces figures with more generalised outputs, which reduces the specificity of targeting for mineralisation prediction. As fault system curvature influences the distribution of static stress, representing curvature with the minimum number of individual planes to retain simplicity was a major consideration. There is some difference in surface trace geometry for the fissures between Allibone et al. (2002) and Oliver et al. (2020). The fault trace geometry from the more recent study has been used here, particularly as this study provides high quality cross sections.

Applying a 10% reverse slip component, following the description of a slight plunge observed in slickenlines in Allibone et al. (2002) produced an positive stress change in the foot wall resolving on reverse faults and in the hanging wall for normal faults. This produced a change of nearly 5MPa, which is enough to significantly impact likelihoods of aftershocks (King et al. 1994). Some mineralisation is observed in halos along the length of the fault, much closer than at the broader stepover damage zone. Small elements of reverse motion could potentially account for this. Changing the coefficient of internal friction has minimal effect on CST. A value of 0.4, which is suggested for faulting on crustal scales, will be used from here.

4.5 Conclusions

Underlapping stepovers of the Ashanti and Insintsium Fissures host mineralisation (Allibone et al. 2002; Oliver et al. 2020). Stress transfer modelling of these structures under $D5_{Ob}$ conditions show areas of positive CST correlating with areas of high gold grade on the fissures. Aftershock sequences are inferred to have allowed for fluid transport and deposition of gold during $D5_{Ob}$ on these structures. Changing the coefficient of internal friction has a small effect of the spatial distribution of Coulomb stresses, increasing the extend of positive CST regions as the coefficient increases. A value of 0.4 will be applied for the remainder of the thesis.

Chapter 5:

Stress-Transfer Modelling of the Obuasi Deposit- $D2_{Ob}$ & $D5_{Ob}$

5.1 Introduction

The previous chapter has shown that the mineralised aftershock domain hypothesis after Micklethwaite and Cox (2006) works at Obuasi, however the extent of this initial study covers a limited section of the whole deposit and only during the $D5_{Ob}$ sinistral strike-slip displacement. Most mineralised faults within Obuasi are dual-stage $D2_{Ob}$ thrust faults, later reactivated with sinistral strike-slip motion during $D5_{Ob}$. Therefore, this section identifies stepover geometries within the entire deposit extent to investigate the impact of hypothesised static stress transfer at this scale. Modelling is applied to $D2_{Ob}$ and $D5_{Ob}$ individually, to investigate the efficacy of the method in correlating with existing resource indications at both stages.

The majority of identified ore shoots at Obuasi are within thick portions of $D2_{Ob}$ shears (Oliver et al. 2020), $F4_{Ob}$ fold hinges overprinting $D2_{Ob}$ shears, and within the short limbs of $F4_{Ob}$ folds. Stepover structures and flexures of the Ashanti and Insintsium Fissures host significant mineralisation. Across the larger deposit extent, there are other ore shoots that exhibit similar strike variation with mineralisation. The GCS ore shoot is hosted in a significant flexure point, both along strike and down-dip. The Anyinam ore shoot is located on the elbow of a much gentler along-strike bend, and the KMS/Justice ore shoots are associated with minor flexure on the Obuasi Fissure formed during $D4_{Ob}$ folding. Gold hosted between the Sansu and Rusty Monkey sections of the deposit also occurs in close proximity to a change in geometry which appears to be stepover-like in nature. In addition to gold associated with strike variation, there is also concentration of ore at fissure intersections, shown in Figure 5.1.

While stepover and flexure geometries strongly correlate with ore shoot locations, significant gold endowment exists in shoots which do not appear to be linked to any

flexure, termination or stepover geometry. The Obuasi deposit is structurally complex and there is uncertainty surrounding timings and modes of major mineralising events (Allibone et al. 2002; Fougerouse et al. 2017; Oliver et al. 2020). Several structural and chemical factors are relevant in addition to zones of aftershock-enhanced permeability which may govern the formation and location of ore shoots, particularly related to the $D2_{Ob}$ and $F4_{Ob}$ structures discussed above. Applying stress transfer modelling to the Obuasi fault system during $D5_{Ob}$ explores seismicity as a further focusing control related to fault bends and stepovers, with aftershock sequence permeability enhancement as a mechanism to explain elevated fluid flux in these locations. Gold emplacement during $D2_{Ob}$ is considered in relation to high angle-reverse fault fluid overpressure cycles (Sibson et al. 1988).

One of the aims for this thesis is to investigate Coulomb 3.3 as a tool for the exploration geologist, particularly during early stage exploration. In this stage, subsurface fault geometries may not be well constrained and the geologist making a Coulomb model may make assumptions. The first models for both mineralisation stages in this chapter represent what a geologist in this position might choose as a simplification. These models are then developed into more representative ones based on published geometries, illustrating the importance of obtaining and applying accurate structural data.

5.2 Methods

D5$_{Ob}$ represents a period of post-basin inversion in which deposit geometries are assumed to be largely the same as their modern appearance. A ductile-to-brittle transition occurred at Obuasi (Allibone et al. 2002), with D5$_{Ob}$ as brittle deformation. The first sections of this investigation, models 1, 2 and 3, concentrate on the sinistral strike-slip reactivation of existing faults as a mineralisation event, targeting stepover or stepover-like geometries inferred from surface mapping, following the methods established in Chapter 3. The modelling is conducted in three stages, starting with a very generalised model using vertical faults (after idealised Andersonian strike-slip faulting), then incorporating the observed dip from sections. The third model incorporates what has been termed the GCS flexure, a large down-dip variation shown in sections (Oliver et al. 2020). Effects of the small reverse component in the sinistral strike-slip D5$_{Ob}$ fault movements as discussed by Allibone et al. (2002) are then investigated in a similar manner to Chapter 4.

D2$_{Ob}$ is interpreted as the end of basin inversion and thrust fault propagation. This event correlates to the generally expected kinematic timing for gold emplacement (Groves et al. 1998) and is cited as a major gold mineralisation stage (Fougerouse et al. 2017; Oliver et al. 2020). Theoretically, this event is expected to be the major contributor to the exceptionally large gold endowment of Obuasi. Because this event may have provided the majority of gold eventually remobilised during D5$_{Ob}$, a repeat of the experimental setup has been made for the earlier NW-SE contractional event, however instead of initially simplifying to vertical faults for an idealised strike-slip environment, the faults have been generalised to an idealised high-angle reverse setting (models 4a, 4b c.f. Sibson et al. 1988). The D5$_{Ob}$ Ashanti Fissure has been removed from D2$_{Ob}$ models. Similarly, working from Oliver et al. (2020), the GCS flexure is linked to D4Ob folding, and therefore would not have been present during D2$_{Ob}$. Because of this, a variable dip and depth model without down-dip flexure has been chosen to represent a closer approximation of the fault system during D2$_{Ob}$ (models 5a, 5b). The Justice Fault is interpreted to have been active during D2$_{Ob}$, exhibiting sinistral transfer fault behaviour (Oliver et al. 2020). This has been

included for models 4 and 5. The models used in this chapter are summarised in Table 5.1.

Model	Tectonic Regime	Geometry	Slip
1	$D5_{Ob}$ NNW, NE(OG) regional compression, vertical sigma 2	Vertical $D2_{Ob}$ and $D5_{Ob}$ fault elements	Strike-slip
2a		Variably inclined (Oliver et al. 2020) fault elements, excluding down dip flexure at GCS	Strike-slip
2b			Strike-slip, reverse component
3a		Variably inclined (Oliver et al. 2020) fault elements, including down dip flexure at GCS	Strike-slip
3b			Strike-slip, reverse component
4a	$D2_{Ob}$	70° inclined $D2_{Ob}$ only faults	Reverse
4b			Reverse, Justice Fault strike slip
5a		Variably inclined (Oliver et al. 2020) $D2_{Ob}$ fault elements	Reverse
5b			Reverse, Justice Fault strike-slip

Table 5.1: A summary table of the models used in Chapter 5.

5.2.1 $D5_{Ob}$ Vertical Model (Model 1)

The first model simplifies the Obuasi deposit to Andersonian strike-slip vertical faults, using geometry mapped at surface (Fig. 5.1A; Oliver et al. 2020), extending to a depth of 2km. For a geologist applying STM to a new prospective gold system where fault surface traces are identified but subsurface geometries are poorly constrained, indications of strike-slip movement would justify simplifying faults in the model to vertical. Model 1 represents a geologist taking this approach, although the geometries of Obuasi are significantly better constrained.

As with preceding studies (Micklethwaite and Cox 2004; Micklethwaite and Cox 2006), hard linkages have been omitted from these structures. A 3D rendering and

plan view of this model is shown in Figure 5.1 (B, C). Faults shown in red in the 3D rendering are elements which move, while the Justice Fault is shown in white. Three distinct stepovers have been identified on the Ashanti Fissure, over the GCS ore shoot zone and between the Sansu and Rusty Monkey ore shoots, which are labelled in Figure 5.1. Curvature of the fault has been simplified to a minimal number of pivot points, most prominently in the west (OG) of the deposit, which are situated at key mineralised pivot points from the deposit, such as the Anyinam, Tom Collins and Akuasso Abrasso ore shoots, also labelled. The F Fissure and 12/74 Fissure have also been included in the model. Physical property input parameters were chosen appropriate to the rock type and tectonic environment: Young Modulus of 80 GPa, coefficient of internal friction 0.4, Poisson's Ratio of 0.25.
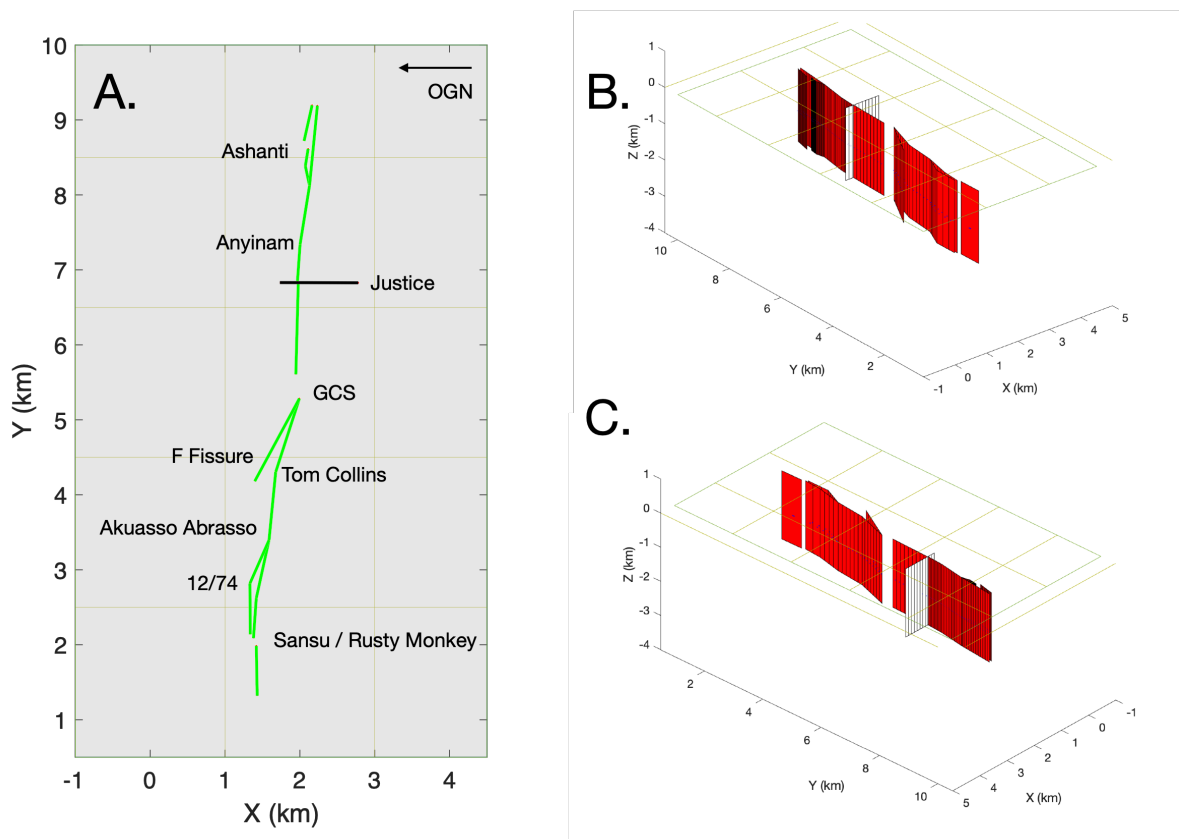
Figure 5.1: A. Plan view of fault elements in simplified vertical Obuasi extent. Black fault represents the crosscutting Justice Fault, while stepovers (shown as gaps) are labelled at the Ashanti Fissure, GCS Flexure and between the Sansu and Rusty

Monkey pits. Along-strike variation occurs at the Anyinam, Tom Collins and Akuasso Abrasso sections of the Obuasi Fissure. Additional elements for the F and 12/74 Fissures have been added. Obuasi Grid North indicated with arrow. B. & C. show 3D renderings of this fault system, looking (Obuasi Grid) SE and NW respectively. Axes provide scale, but do not correlate to an existing grid system.

Fault length versus displacement scaling relationships as reviewed by Torabi and Berg (2011) assert that earthquake rupture events for strike-slip faults of ~8km length have displacements of between ~0.05 and ~0.8m. A sinistral movement of 0.1m has been applied to every fault element in the fault system, following the combined slip method of Micklethwaite and Cox (2006), excluding the cross-cutting Justice fault, which is marked in black. As with earlier D5$_{Ob}$ modelling, this setup applies a NNW regional stress compression, after Fougerouse et al. (2017), with sub-horizontal $\sigma 1$ and $\sigma 3$. Details of input parameters and stress fields are included in Appendix I. The modelled stresses are resolved on optimised strike-slip, thrust and normal faults, on a 100m surface grid.

As discussed in Chapter 4, Allibone et al. (2002) cite evidence for small components of reverse movement during D5$_{Ob}$. Adding reverse slip to vertical Coulomb models does not change the calculated CST.

5.2.2 D5$_{Ob}$ Variable Dip Model- excluding GCS flexure (Model 2)

To represent the multiple generations of faults and shears at Obuasi which vary in both dip and depth, modifications have been made to the dips and depths of the fault elements shown in Figure 5.1. The surface trace, number of fault elements used, and their strike variations are retained. The Obuasi (becoming at depth the Main Reef) Fissure dips ~70° OGN at the OGE end of the deposit, extending to around 2km depth with mineralisation. Moving along the deposit Obuasi Grid east to west, the fissure becomes closer to vertical, and the mineralised extent becomes shallower, to around 500m depth at Sansu. At the Sansu end of the deposit, the Obuasi fissure becomes subvertical and eventually reverses to dip ~85° OG S. In the centre of the deposit, the GCS flexure adds significant complexity down-dip. This

model generalises the GCS flexure to one average down dip value for centrally located fault elements. Figure 5.2 presents a plan view and 3D rendering of this model (model 2a), where boxes represent the extent of dipping elements when viewed from above. Dip estimations are taken from Figure 5 of Oliver et al. (2020).
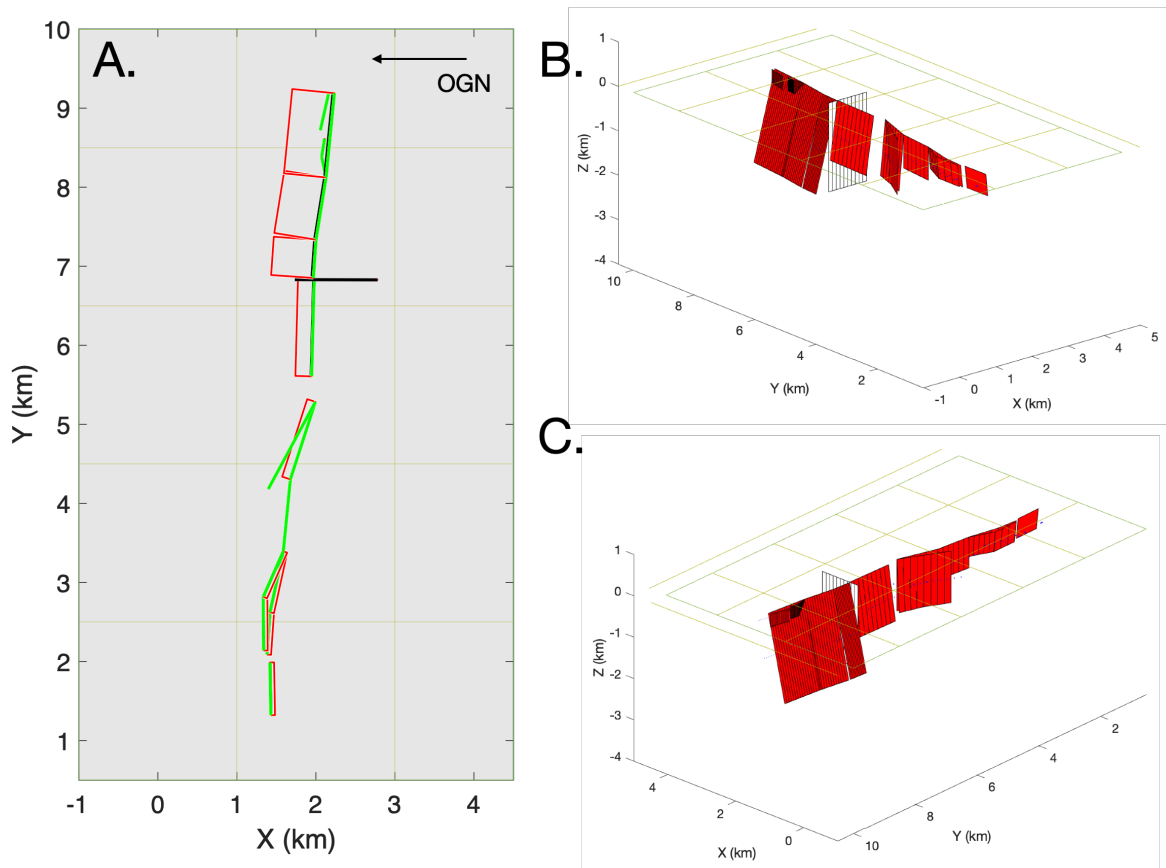
Figure 5.2: A. Plan view of fault elements in variable dip and depth Obuasi extent, where red panels show dipping fault elements. Black fault represents the crosscutting Justice Fault. Obuasi Grid North indicated with arrow. B. & C. show 3D renderings of this fault system, looking (Obuasi Grid) SE and SW respectively.

A modelled 0.1m sinistral strike-slip movement under $D5_{Ob}$ stress was applied in the same manner as the vertical extent setup seen in Figure 5.1. This was modelled at 100m, 500m and 1000m depths, which correlate roughly to productive ore zones as indicated in Oliver et al. (2020), to show stress variation relative to down dip fault system geometry for this, model 2a.

For model 2b, an additional 10% reverse slip component was modelled, sampled at 100m depth. All other input parameters were unchanged, as with model 1. Due to the varying dips and depths of fault elements for this model, reverse slip impacts CST and so is presented in the results. Both investigations are resolved on optimised strike-slip, thrust and normal faults.

5.2.3 D5$_{Ob}$ Variable Dip Model- including GCS flexure (Model 3)

Representing down-dip fault orientation variation in Coulomb 3.3 is achieved using additional fault element panels, the tops of which directly correlate to the bottoms of the elements above, located using x-y coordinates. The effects of variations down-dip are shown by sampling at various depths for model 2a and 2b. In these models, the GCS down-dip flexure has been simplified and incorporated using additional fault elements which alter dip values with depth, shown in Figure 5.3 (model 3). The surface trace is identical to that shown in Figures 5.1. & 5.2., with the 3 additional fault elements visible in plan view. This geometry has been inferred from Oliver et al. (2020) Figure 5, and represents the prominent GCS flexure section of the deposit, retaining down-dip simplification in the majority of the deposit.
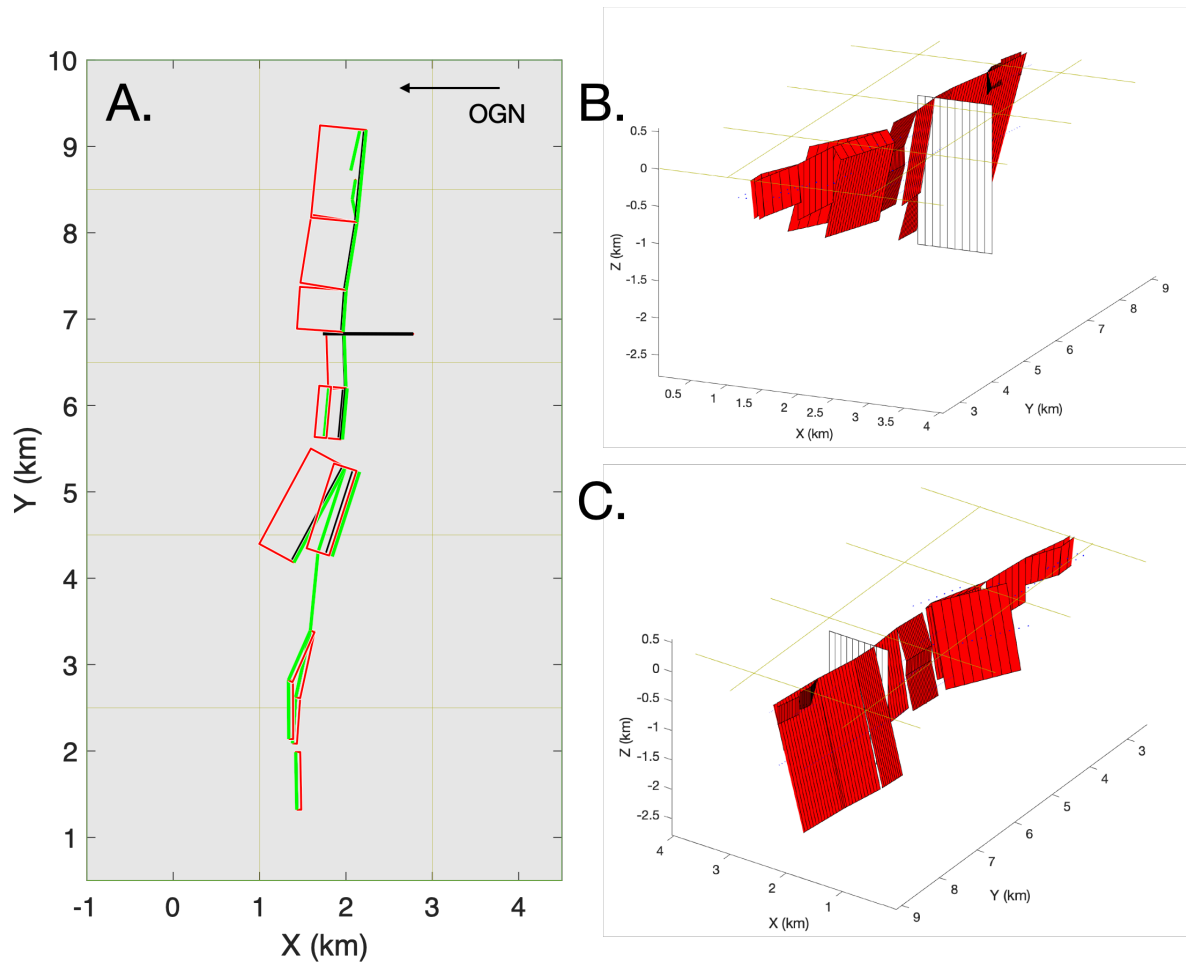
Figure 5.3: A. Plan view of fault elements in variable dip and depth Obuasi extent including GCS flexure, where red panels show dipping fault elements. Black fault represents the crosscutting Justice Fault. Obuasi Grid North indicated with arrow. B. & C. show 3D renderings of this fault system, where flexure can be observed on two central fault panels. The renderings are oriented (Obuasi Grid) NE and SW respectively.

Sample depths of 100m, 600m and 1000m have been analysed for each of the three optimised fault types, which are taken at each down-dip change of geometry to show the effect of modelling down-dip flexure. The non-geometric input parameters have been retained, as above. A further 10% reverse slip component (model 3b), as with models 1 & 2b, has been analysed at 100m depth, and additionally at 600m depth to

investigate the change down-dip. 600m depth has been used because CST cannot be calculated in Coulomb 3.3 at depths where fault elements terminate.

5.2.4 D2$_{Ob}$ High-Angle Reverse Model (Model 4)

Models for D2$_{Ob}$ (models 4 and 5) omit structures associated with later deformation stages. The Ashanti Fissure is removed, and the stress field orientation is changed. For model 4, the typical 70° dip for fault-seal behaviour high-angle reverse faults has been used (Sibson et al. 1988). D2$_{Ob}$ is characterised by a NW-SE compressional regime, with sub-horizontal σ1 and sub-vertical σ3 (Oliver et al. 2020). The other model input parameters, such as physical properties and depth extents have been retained from the previous models. Figure 5.4 shows the model 4a, which includes the Justice Fault. Oliver et al. (2020) state that it is likely Justice was present during D2$_{Ob}$, possibly as a 'transfer-like break' structure, to which Allibone et al. (2002) attribute a sinistral sense of movement. Along strike variations at Anyinam, Tom Collins and Akuasso Abrasso, and the F and 12/74 Fissures are retained.
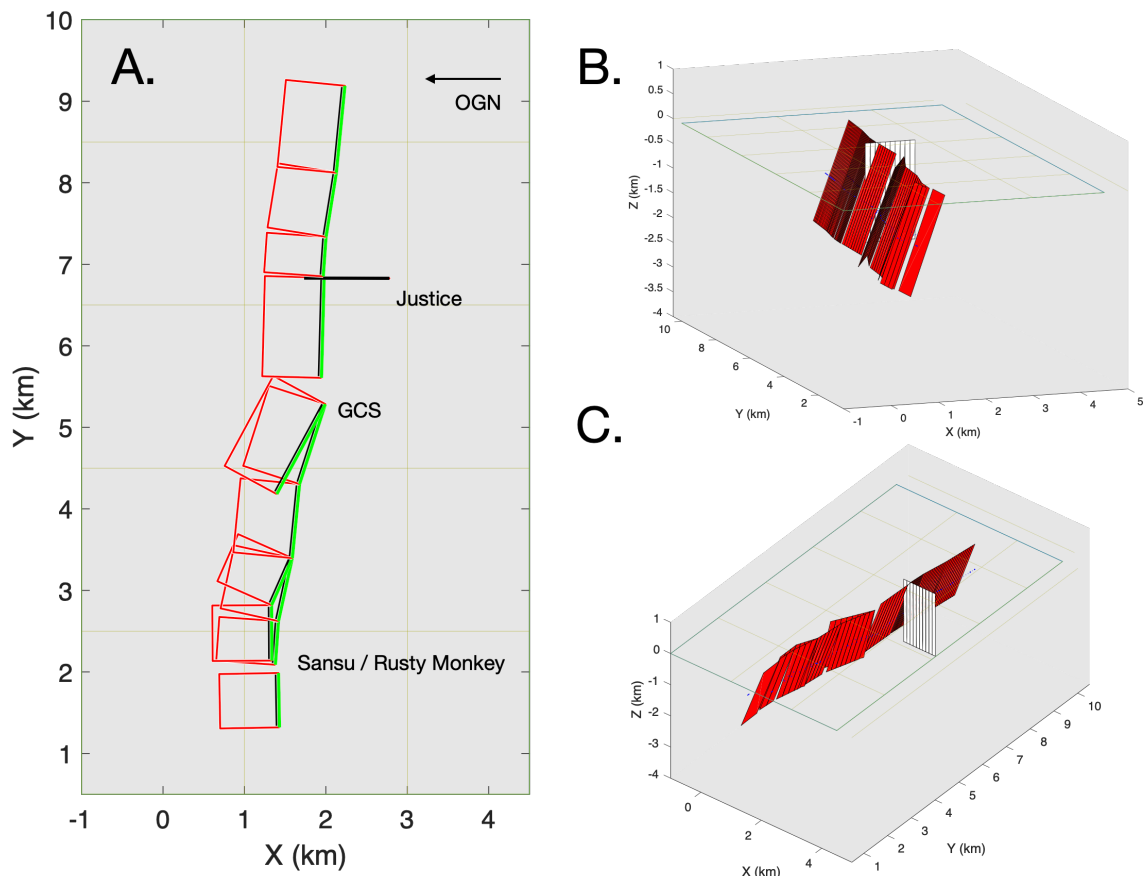
Figure 5.4: A. Plan view of high-angle reverse fault elements generalised to 70°, where red panels show fault element dip. Black fault represents the crosscutting Justice Fault. Obuasi Grid North indicated with arrow. B. & C. show 3D renderings of this fault system, viewing (Obuasi Grid) SE and NE respectively.

In this model, where fault elements have variable strikes but constant non-vertical dips, underlap and overlaps occur at each boundary. Sampling at 100m depth minimises the lateral extent and therefore impact of these gaps, but there is a possibility that anomalous values can be generated. Using fault scaling relations (Torabi and Berg 2011), a 0.1m reverse movement was chosen, applied to all fault elements except the Justice Fault, in the combined-slip method. This is resolved on optimised strike-slip, thrust and normal faults. Following this, to investigate the effect of Justice as a transfer-like fault, a 0.05m sinistral strike-slip movement was modelled on the Justice Fault in addition to the 0.1m reverse slip on all other fault elements (model 4b).

5.2.5 D2$_{Ob}$ Variable Dip Model (Model 5)

As with model 2, model 5 uses dips and depths simplified from Oliver et al. (2020) excluding down-dip flexure, shown in Figure 5.5 (Model 5a). The Ashanti Fissure and D4$_{Ob}$ GCS flexure are not represented. The D2$_{Ob}$ regional stress (Oliver et al. 2020) is applied.
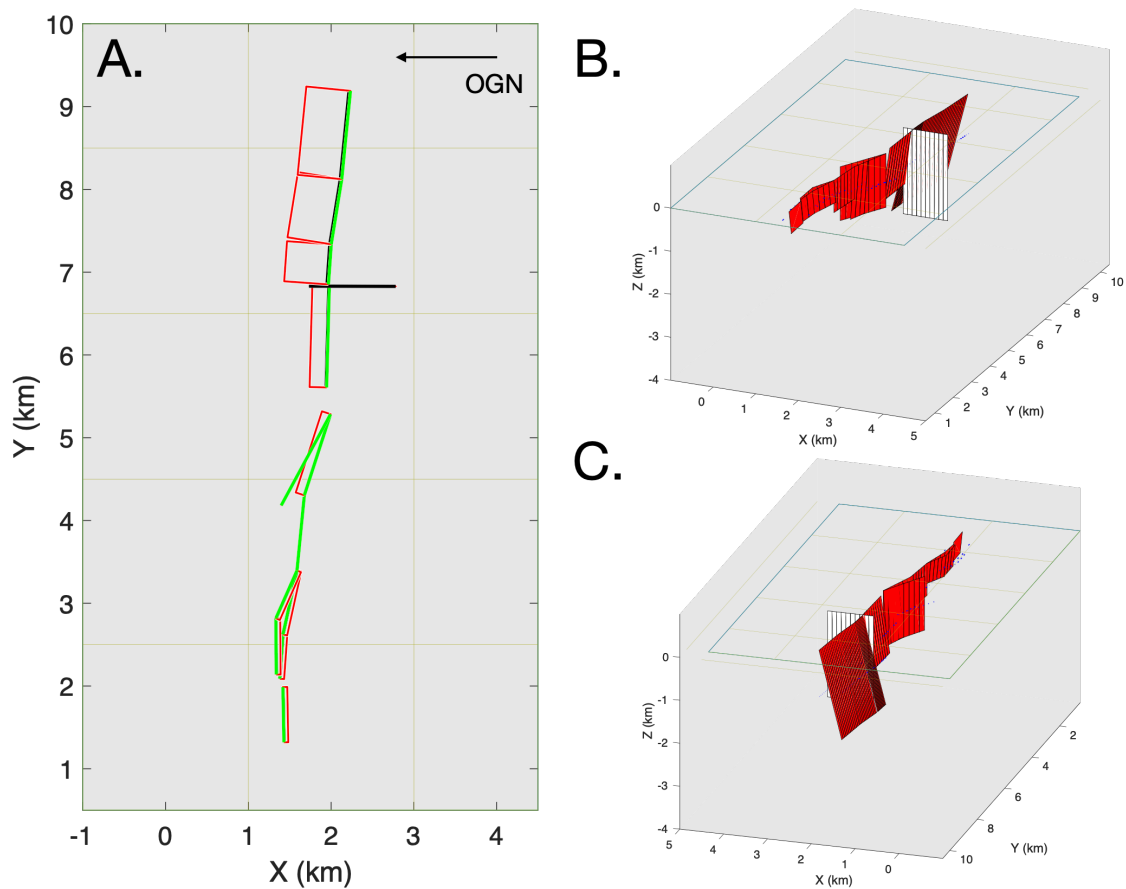
Figure 5.5: A. Plan view of variable dip and depth fault elements, where red panels show fault element dip. Black fault represents the crosscutting Justice Fault. Obuasi Grid North indicated with arrow. B. & C. show 3D renderings of this fault system, viewing (Obuasi Grid) NE and SW respectively.

A reverse movement of 0.1m was modelled using the combined slip method at depths of 100m, 500m and 1000m, using D2$_{Ob}$ regional stress (see Appendix I), resolved on optimised strike-slip, thrust and normal faults. This was then repeated to include 0.05m of sinistral strike-slip transfer behaviour on the Justice Fault, at 100m depth (model 5b).

5.3 Results

5.3.1 D5$_{Ob}$ Vertical Model (Model 1)

Model 1 produces positive Coulomb stresses across the Ashanti, GCS and Sansu/Rusty Monkey stepovers, with additional regions of calculated positive CST associated with along-strike fault curvature at Anyinam, Tom Collins and Akuasso Abrasso. Coulomb stress patterns calculated at 100m depth, resolved on optimised strike-slip, thrust and normal faults are shown in Figure 5.6 (model 1). The general distribution of positive stress shadows is largely as expected for strike-slip regime stepovers (e.g. Micklethwaite and Cox 2004; Micklethwaite and Cox 2006), with lobate positive stress shadows emanating from fault terminations and to a lesser extent from points of curvature on each fault. The calculated patterns vary in orientation with relation to which type of optimised fault has been selected.

Stress patterns in Figure 5.6A (optimised strike-slip faults) and 5.6C (optimised normal faults) show similar distributions to one another, in both geometry and extent. Positive stress shadows extend in lobes striking OG SE-NW from the Sansu/Rusty Monkey and GCS stepovers, and remain proximal to the fault between these points, above where the 12/74 Fissure re-joins the Obuasi Fissure. At the Ashanti stepover, positive stress shadows extend OG North and East. 5.6C shows slightly more extensive Coulomb stress shadowing, particularly at greater distance and from the fault terminations. Small positive Coulomb stresses are calculated at the intersection of the Justice Fault, and a curving band of elevated Coulomb stress, less intense than at stepover points curves around the OG South of the Justice Fault.
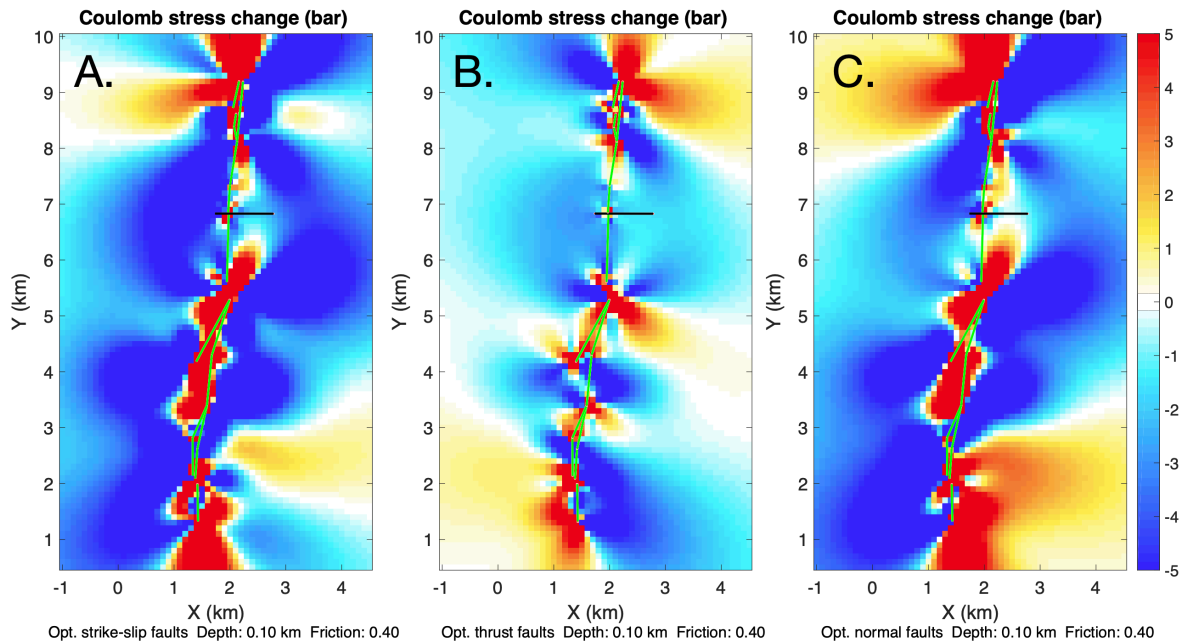
Figure 5.6: Coulomb stress change patterns at 100m depth for 0.1m sinistral strike-slip movement on a simplified vertical model of the Obuasi fault system, resolved on optimised strike-slip (A), thrust (B.) and normal (C.) faults.

Figure 5.6B, showing stress resolved on thrust faults, shows smaller positive stresses, in the Ashanti, Sansu/Rusty Monkey and central GCS sections of the deposit, but extending Obuasi Grid NE-SW, a reversal of the general lobate pattern of Figures 5.6A and 5.6C. Positive stresses generally remain proximal to the fault, particularly in Figures 5.6A and 5.6C, extending less than 500m from the fault centre for most of the fault system extent. Larger stress shadows are observed at the terminations of the faults OG East and West. As with the results of all vertical fault modelling discussed in Chapter 4, adding a 10% (0.01m) reverse slip component produces output figures identical to those without a reverse slip-component.

5.3.2 D5$_{Ob}$ Variable Dip Model- excluding GCS flexure (Model 2)

Along strike variation in dip and vertical extent produces more complex CST patterns. Because fault interactions change down dip, Coulomb stress patterns also vary with depth. This is shown in Figure 5.7, which illustrates sampling at 100m, 500m, and 1000m depth on model 2a.

Concentrations of positive Coulomb stress appear in similar locations to those modelled when using purely vertical fault elements, i.e., across stepover gaps and proximal to the faults, with some lobate patterns emerging, although these are generally smaller. A similar pattern observed to model 1: stresses resolved on strike-slip and normal faults are similar, and contrast with those on thrust faults . Comparing Figures 5.6A, B and C, with 5.7A, B and C, all calculated at 100m depth, the most notable difference between the patterns is the lateral extent of Coulomb positive stress. For the vertical model (model 1), a positive static stress zone of up to ~800m width along the fault is observed. This reduces to a maximum of ~500m for the variable dip and depth model (model 2). The switch between OG SE-NW lobe orientation for Figure 5.7A and C compared to NE-SW(OG) orientation for Figure 5.7B is observable, as with the results of model 1. The effect of strike variability at Anyinam, Tom Collins and Akuasso Abrasso is greater for model 2 than model 1. Greater degrees of positive Coulomb stress are calculated around the Justice Fault, with the curved band emanating from the GCS flexure point being much more pronounced.

The stress changes with depth in this model are less pronounced between the calculations at 100m and 500m depth, which both appear closer to fault elements and stepovers than in Figure 5.6, than those calculated at 1000m depth on model 2a. Many of the fault elements at the Obuasi Grid western end of the fault do not extend to this depth based on the available sections, which results in a broader zone of general positive Coulomb stress underlying the west (OG) of the deposit.

Figure 5.7: Coulomb stress change patterns at 100m (A,B,C), 500m (D,E,F) and 1000m (G,H,I) depth for 0.1m sinistral strike-slip movement on a variable dip and depth model of the Obuasi fault system, excluding the GCS flexure, resolved on optimised strike-slip (A,D,G), thrust (B,E,H) and normal (C,F,I) faults.

Adding a 10% reverse slip component to non-vertical fault elements (model 2b) has an observable but small impact on the static stress changes induced for model 2a. At 100m depth, the calculated stress patterns for model 2b are shown in Figure 5.8. In detail areas of positive Coulomb stress track across further towards the Obuasi Grid South, by a maximum of 100m, but the reverse slip does not change the distribution across stepovers.
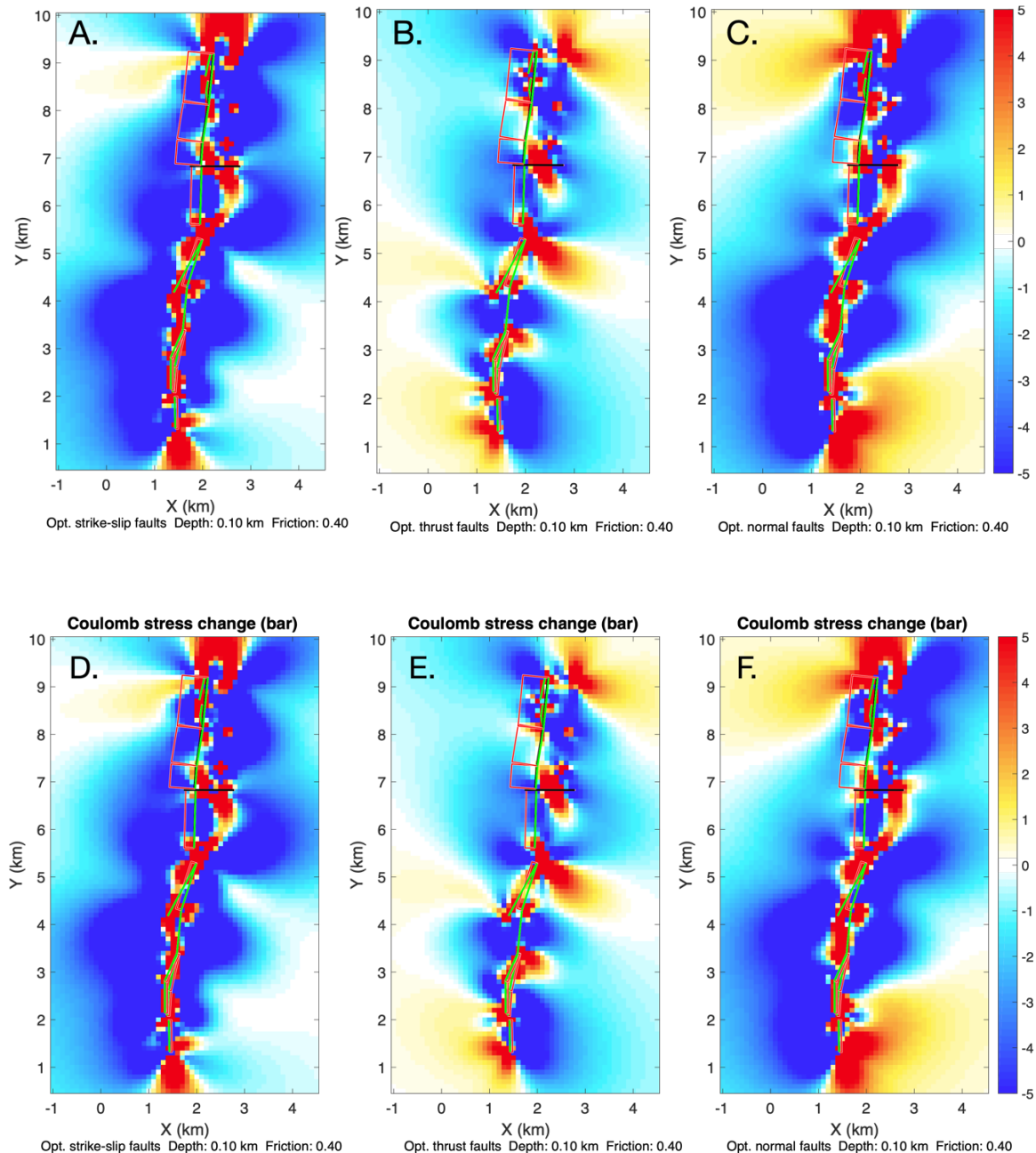
Figure 5.8: Coulomb stress change patterns at 100m depth for 0.1m sinistral strike-slip movement (A, B, C) and with an additional 0.01m reverse component (D, E, F) on a variable dip and depth model of the Obuasi fault system, resolved on optimised strike-slip (A, D), thrust (B, E) and normal (C, F) faults.

5.3.3 D5$_{Ob}$ Variable Dip Model- including GCS flexure (model 3)

The results from model 3a (including the down-dip GCS flexure) at 100m, 600m, and 1000m are shown in Figure 5.9. Incorporating the down-dip geometry creates noticeably larger regions of positive Coulomb stresses across the GCS flexure region, extending much further from the stepover. The more lobate structures observed in earlier models at the GCS stepover combine to a larger continuous zone of positive static stress change. This effect is visible across all sampled depths and is particularly pronounced between the GCS stepover and the Justice Fault, where an intensification of the zone of positive Coulomb stress, which already intensified from model 1 to 2, is observed. Distally from the flexure, where the fault elements are the same as those for model 2, the Coulomb stresses are very similar to those of model 2.
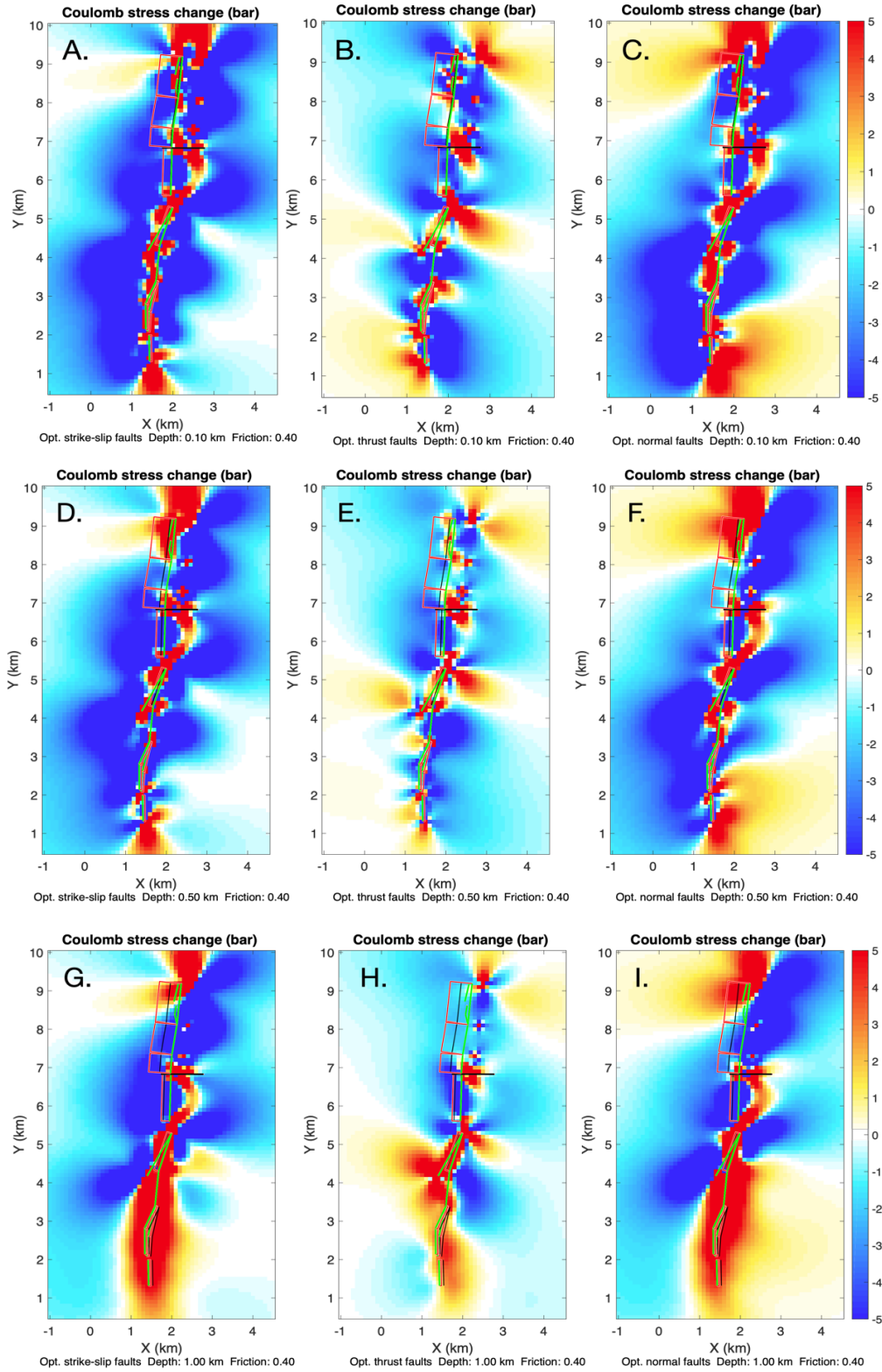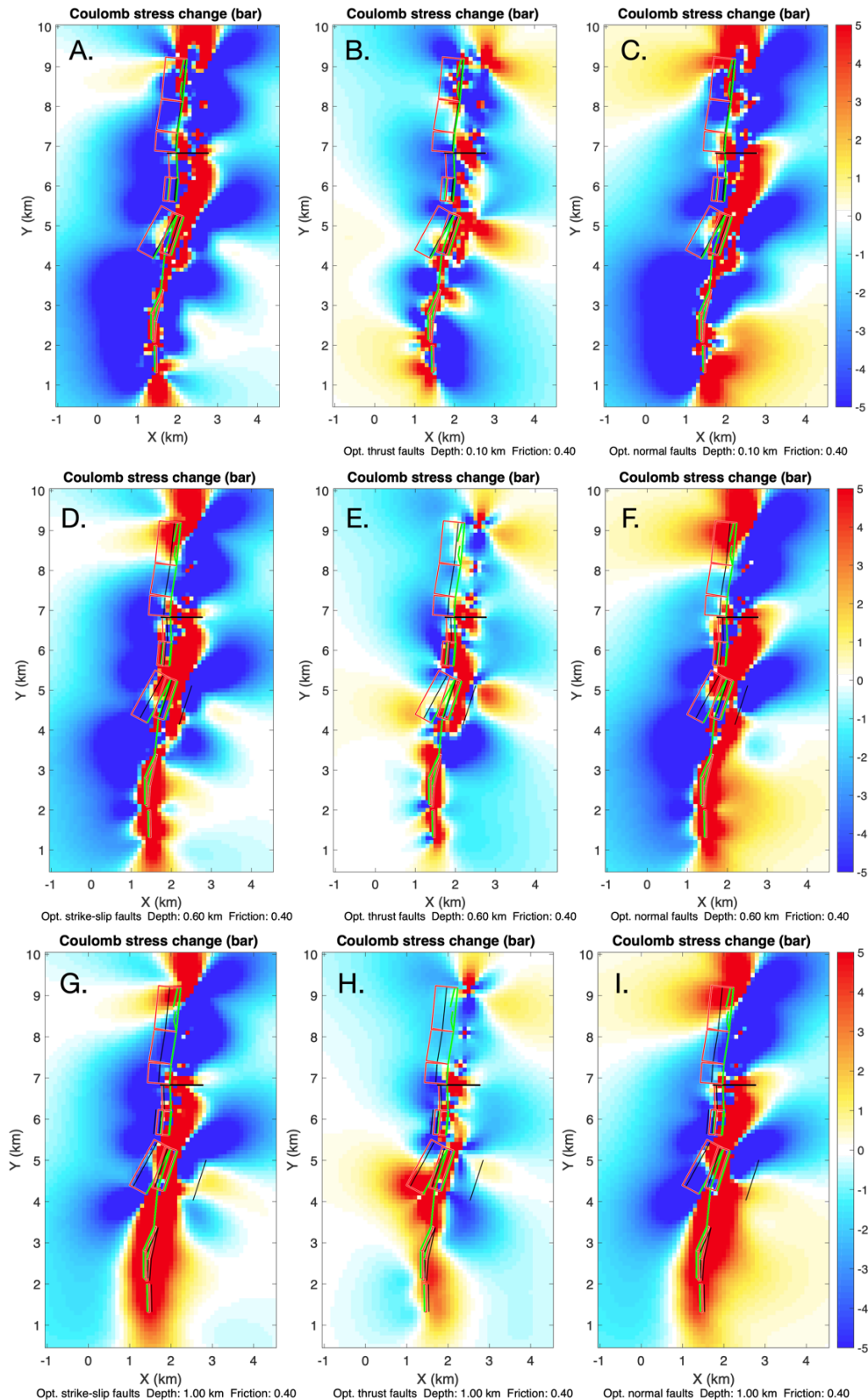
Figure 5.9: Coulomb stress change patterns at 100m (A,B,C), 600m (D,E,F) and 1000m (G,H,I) depth for 0.1m sinistral strike-slip movement on a variable dip and depth model of the Obuasi fault system, including the GCS flexure, resolved on optimised strike-slip (A,D,G), thrust (B,E,H) and normal (C,F,I) faults.

Results from the addition of 10% reverse slip across variable down-dip geometry, are seen in Figure 5.10 (model 3b). As with the added reverse slip results for model 2b, Figure 5.7, the general pattern of Coulomb stresses look very similar to those without a reverse component. A small shift of positive Coulomb stress towards the hanging wall is observed when resolved on thrust faults and the footwall when resolved on normal faults.
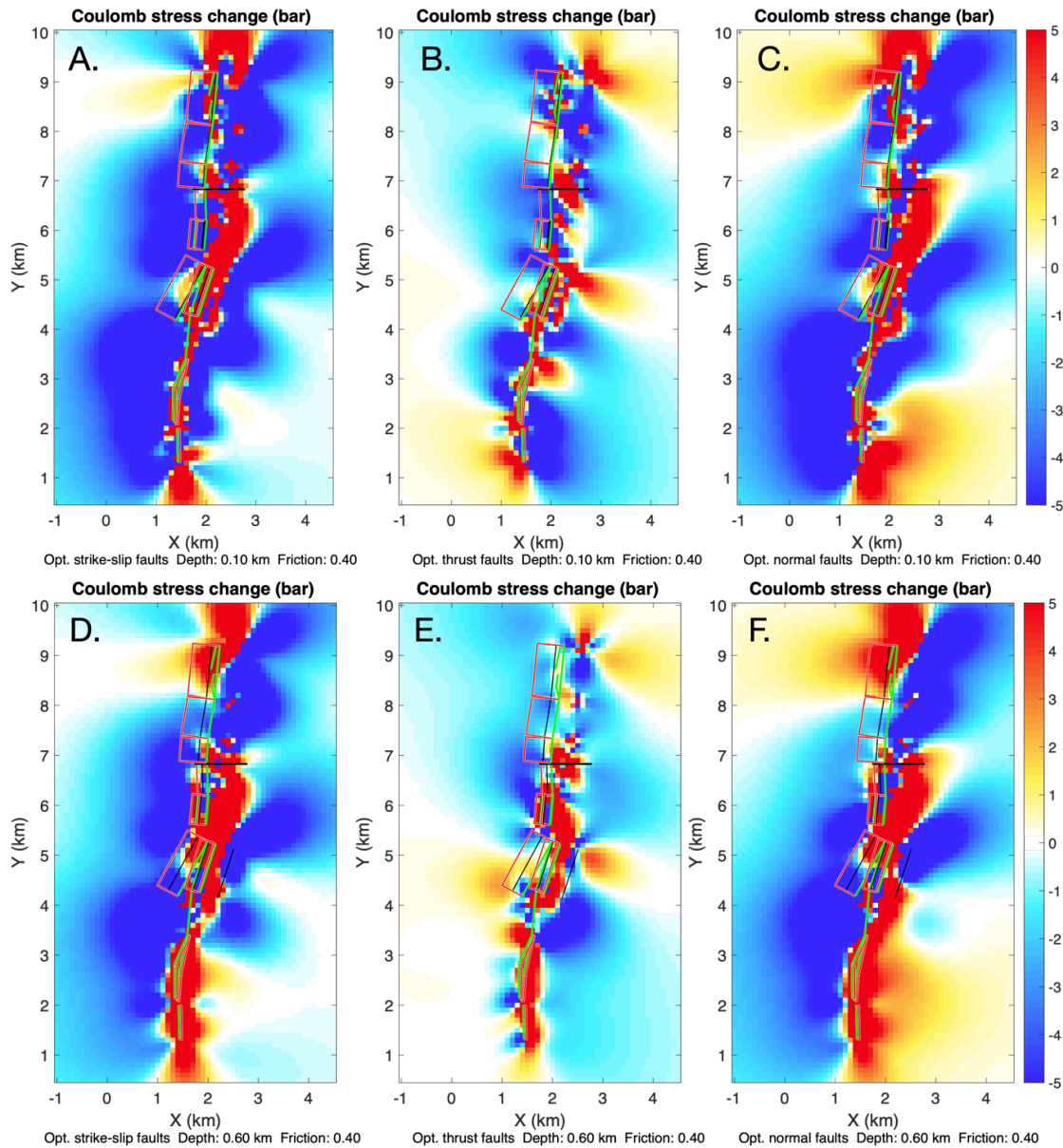
Figure 5.10: Coulomb stress change patterns at 100m (A,B,C) and 600m (D,E,F) depth for 0.1m sinistral strike-slip movement, with a 0.01m reverse component on a variable dip and depth model, including GCS down-dip flexure of the Obuasi fault system, resolved on optimised strike-slip (A,D), thrust (B,E) and normal (C,F) faults.

5.3.4 D2$_{Ob}$ High-Angle Reverse Model (Model 4)

The high-angle reverse model results at 100m depth without any transfer behaviour of the Justice Fault are shown in Figure 5.11.

Figure 5.11: Coulomb stress change patterns at 100m depth for 0.1m reverse movement, on a simplified high-angle reverse fault model of the Obuasi fault system, resolved on optimised strike-slip (A.), thrust (B.) and normal (C.) faults.

The stress patterns calculated in this model are distinctly different to those of the D5$_{Ob}$ models. For Figure 5.11A and C (model 4a) a general, lower intensity positive Coulomb stress is modelled in the hanging wall, and for all three fault types a distinct band of points are shown in the footwall. Positive and negative Coulomb stresses occur on this band, producing alternating lobate structures. This OG east-west band lies ~800m OG south of the fault system and appears to be associated with points of along-strike flexure and stepover points. Where fissures split, such as the 12/74 Fissure and Obuasi, or Obuasi and the F Fissure, positive Coulomb stress transfer is modelled in the space between.

Adding a sinistral movement of 0.1m on the Justice Fault (Model 4b), changes calculated Coulomb stress patterns in a much more dramatic manner than the earlier reverse fault investigations of models 1-3 (Figure 5.12). Additional stresses are recorded proximal to the Justice Fault, but also directly above the Obuasi Fissure in the OG easternmost section. The spatial distribution is similar to that of 4a but modelling transfer movement of the Justice Fault brings positive Coulomb stresses closer to the fault system (Figure 5.12).
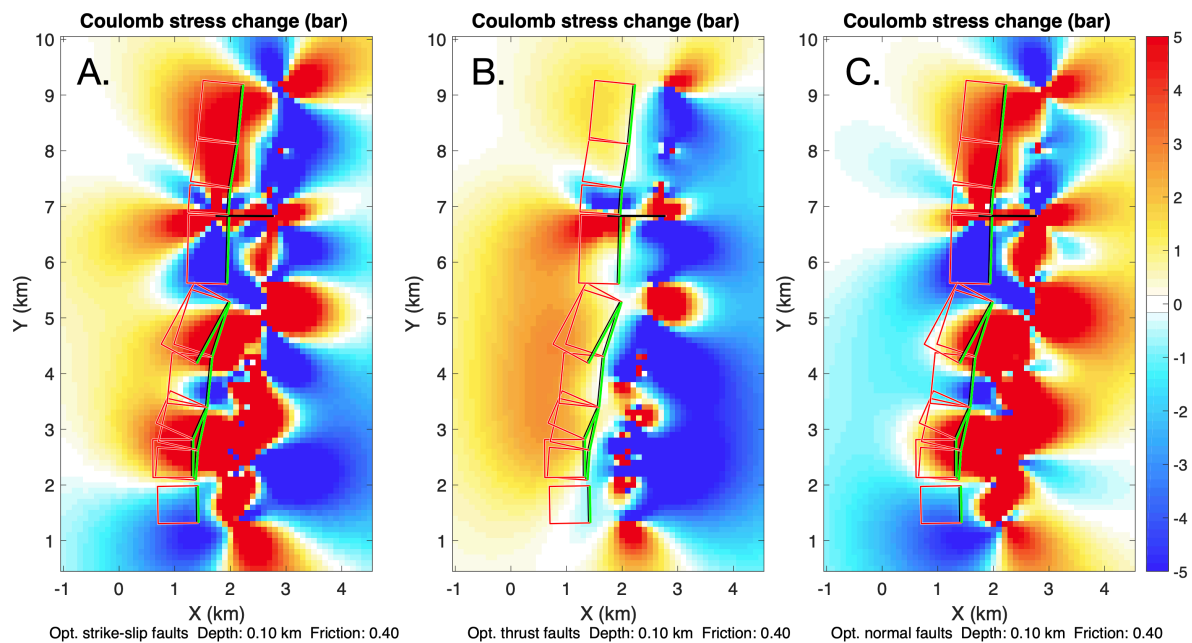
Figure 5.12: Coulomb stress change patterns at 100m depth for 0.1m reverse movement, on a simplified high-angle reverse fault model of the Obuasi fault system, with 0.1m sinistral strike-slip movement on the Justice Fault (black). Stresses resolved on optimised strike-slip (A.), thrust (B.) and normal (C.) faults.

5.3.5 D2$_{Ob}$ Variable Dip Model (Model 5)

As established in the D5$_{Ob}$ models, a model of Obuasi with dips derived from sections produces different patterns of Coulomb stress to those from a model using all estimated dips (models 1 and 4). This transition is much more pronounced for D2$_{Ob}$ than it was in the D5$_{Ob}$ modelling. Calculated under D2$_{Ob}$ regional stress with 0.1m reverse slip, Figure 5.13 shows the Coulomb stresses at 100m, 500m and

1000m depth. Compared to the high-angle reverse fault case (model 4), the band of positive and negative stress nucleation points to the Obuasi Grid south of the fault system have become less pronounced and appear only in the OG east. Changes to Coulomb stress patterns are observed with depth, with generally larger Coulomb stress shadows observed at shallower depths. Positive Coulomb stress is preferentially transferred into the hanging wall of the reverse faults, shown by positive stresses induced Obuasi grid south of the Sansu/Rusty Monkey section of the fault.

Adding transfer behaviour on the Justice Fault (model 5b) creates larger positive static stress regions and equally large stress shadows (Figure 5.14). Greater than kilometre scale lobate positive shadows are produced from each of the stepovers, with the Ashanti ore shoot section exhibiting a similar offset to that observed with all earlier models.
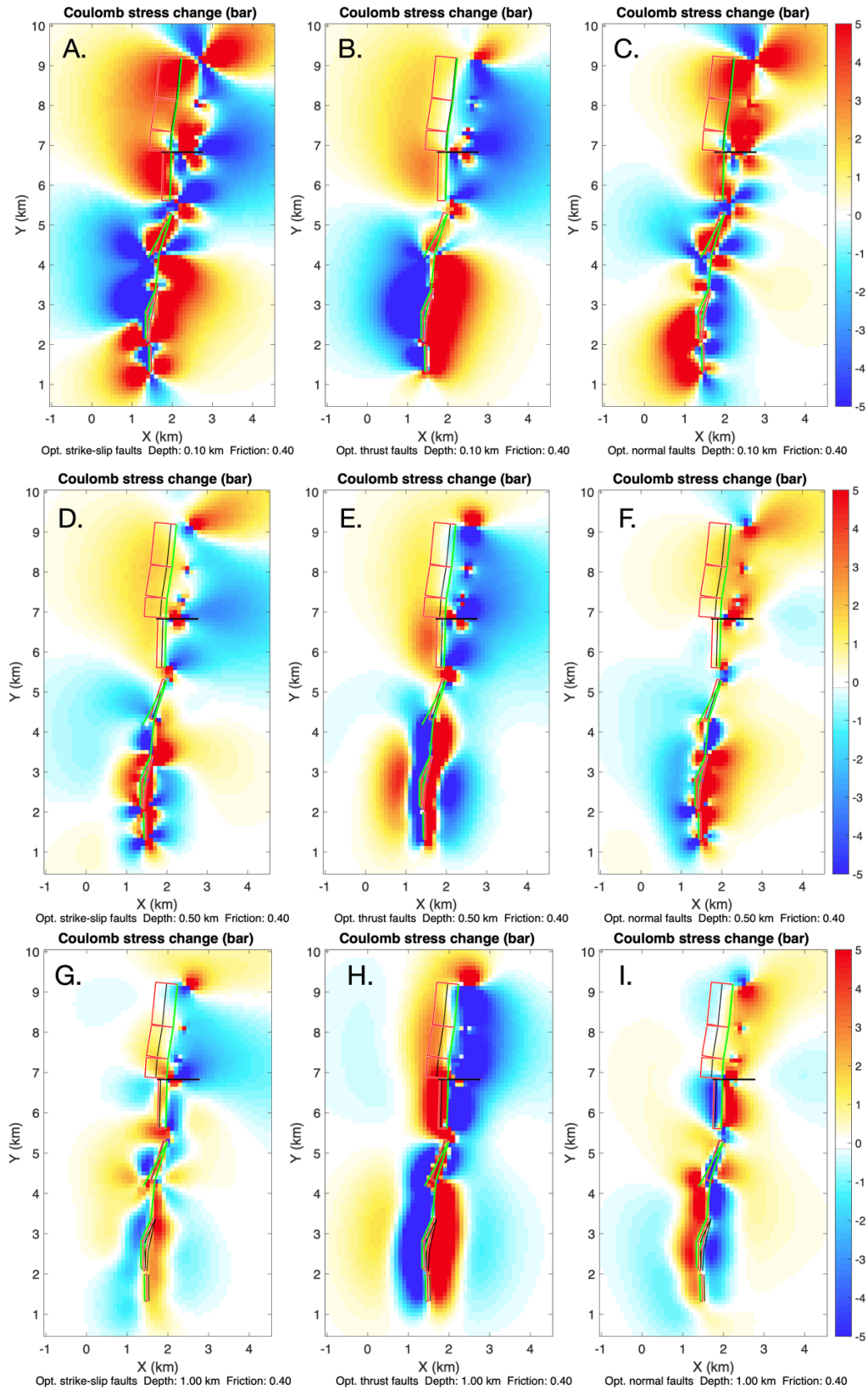
Figure 5.13: Coulomb stress change patterns at 100m (A,B,C), 500m (D,E,F) and 1000m (G,H,I) depth for 0.1m reverse movement on a variable dip and depth model of the Obuasi fault system, resolved on optimised strike-slip (A,D,G), thrust (B,E,H) and normal (C,F,I) faults.
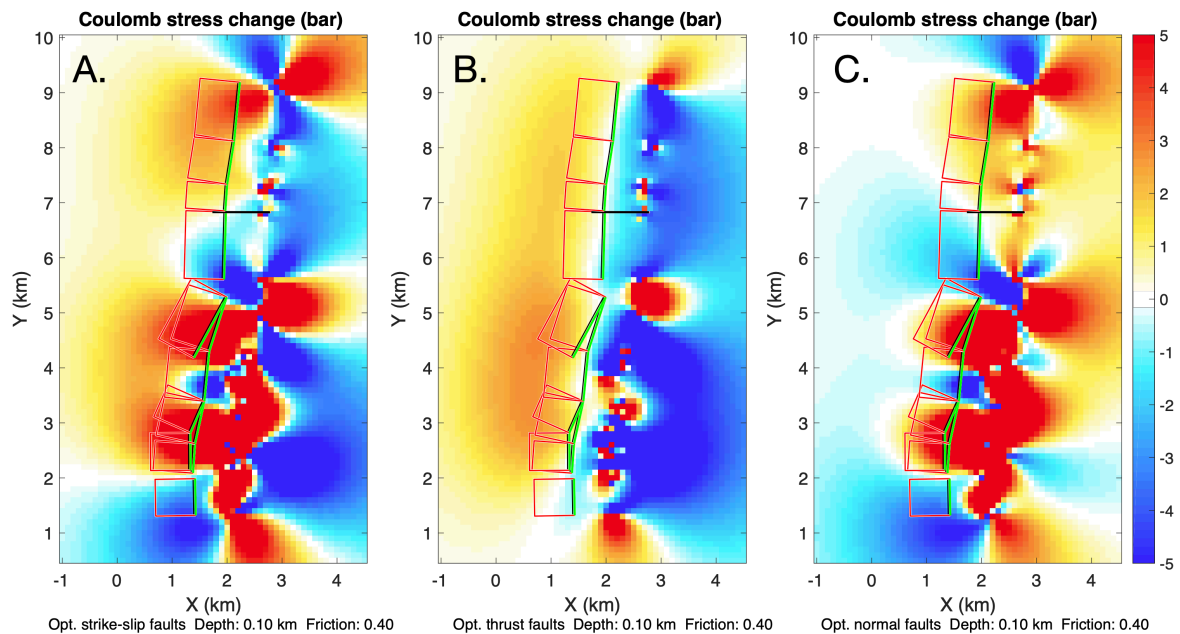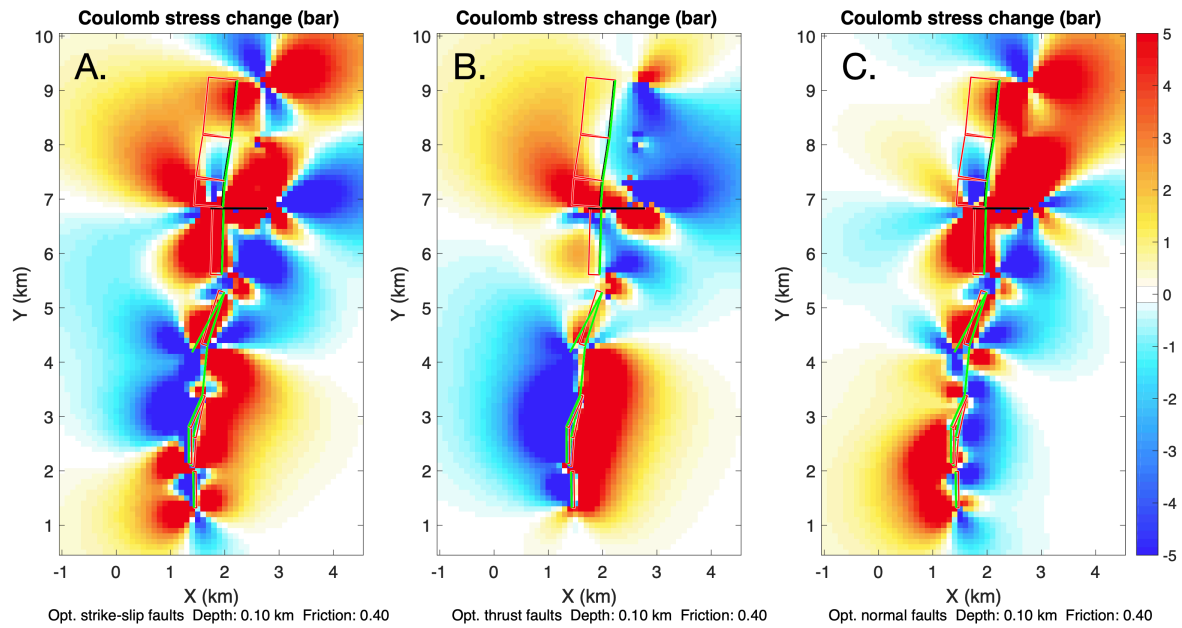
Figure 5.14: Coulomb stress change patterns at 100m depth for 0.1m reverse movement, on a variable dip and depth model of the Obuasi fault system, with 0.1m sinistral strike-slip movement on the Justice Fault (black). Stresses resolved on optimised strike-slip (A.), thrust (B.) and normal (C.) faults.

5.4 Discussion

5.4.1 Stepover Identification

Geometries at Obuasi have been identified using surface trace maps (Allibone et al. 2002; Oliver et al. 2020) and have been represented in the model without hard-linkage on the Ashanti Fissure, GCS flexure and between the Sansu and Rusty Monkey ore shoots, using the methods of (Micklethwaite and Cox 2006). The available maps are a simplified representation of the fault system at Obuasi, and the models applied here are a further simplification on these. The Ashanti Fissure stepover is confidently identified, as it is discussed in Allibone et al. (2002) with a detailed map. The stepovers on the GCS flexure and Sansu/Rusty Monkey have been inferred from fault traces at varying depths (Oliver et al. 2020). These are not

discussed as stepovers in earlier papers. Stepover geometries have been inferred from sections of fissure traces which show short sections which strike obliquely from the northeast-southwest trend of the fault system. It is inferred that under the $D5_{Ob}$ strike-slip slip regime these geometries would have exhibited stepover-like behaviour.

5.4.2 Results for $D5_{Ob}$

A trend of positive Coulomb stresses emanating from the stepovers at Ashanti, GCS and Sansu/Rusty Monkey and from fault curvature represented at Anyinam, Tom Collins and Akuasso Abrasso is shown for each of the $D5_{Ob}$ models, which is present in all three models. Models X, y have simple lobate stress change patterns reminiscent of strike-slip system studies (Micklethwaite and Cox 2004; Micklethwaite and Cox 2006) and patterns originating from fault terminations (e.g. Cox and Ruming 2004). The CST patterns become less lobate as dip variability is increased (model Z). Positive stress changes are calculated proximally to the fault system, in agreement with the disseminated sulphide-associated mineralisation trends reported in Obuasi literature (e.g. Oberthur et al. 1995; Allibone et al. 2002; Oliver et al. 2020).

Three Andersonian fault styles have been applied as receivers (Toda et al. 2011a). $D5_{Ob}$ was a predominantly strike-slip regime (Fougerouse et al. 2017; Oliver et al. 2020), making strike-slip faults the most likely receiver faults for aftershock slip events around the deposit. Regional stress field character has been shown experimentally to be the most important consideration for choosing receiver fault orientations (Steacy et al. 2005b). However, particularly in association with stepovers, $D5_{Ob}$ thrust and normal faults are found at Obuasi (Allibone et al. 2002). Considering that the three idealised fault types occur at Obuasi contemporaneously, results have been included for each. This choice was made because orientations and senses of movement are not available for mineralised small-displacement receiver faults present at Obuasi. There are noticeable differences between the stress patterns calculated on each of these fault types. Calculating on optimised strike slip and normal faults generate results which are much closer to each other

than calculations using optimised thrust faults, which are significantly different when compared to the strike-slip and normal fault examples.

The implication for the impact of static stress on D5$_{Ob}$ gold emplacement is comparable to the conclusions of Micklethwaite and Cox (2004; 2006), where there is strong correlation between small-displacement mineralised faults and areas of static stress change from large-displacement events. This supports the hypothesis that static stress changes exert a first-order control on the distribution of near field, aftershock-driven fracturing and faulting, leading to preferential gold mineralisation due to elevated fluid flux through the aftershock domains. Resource locations greater than one gram per ton from Oliver et al. (2020) are presented as a polygon overlay to model 1 of this study in Figure 5.15. High grade gold ore zonation occurs proximal to the Obuasi fault system and concentrates particularly in the areas of complexity identified in this study. Gold polygons indicating the resource distribution are not assigned to specific mineralisation stages. The resource distribution is shown at the surface level for models run at surface, and at 600m depth for model 3, at the level of the GCS flexure.
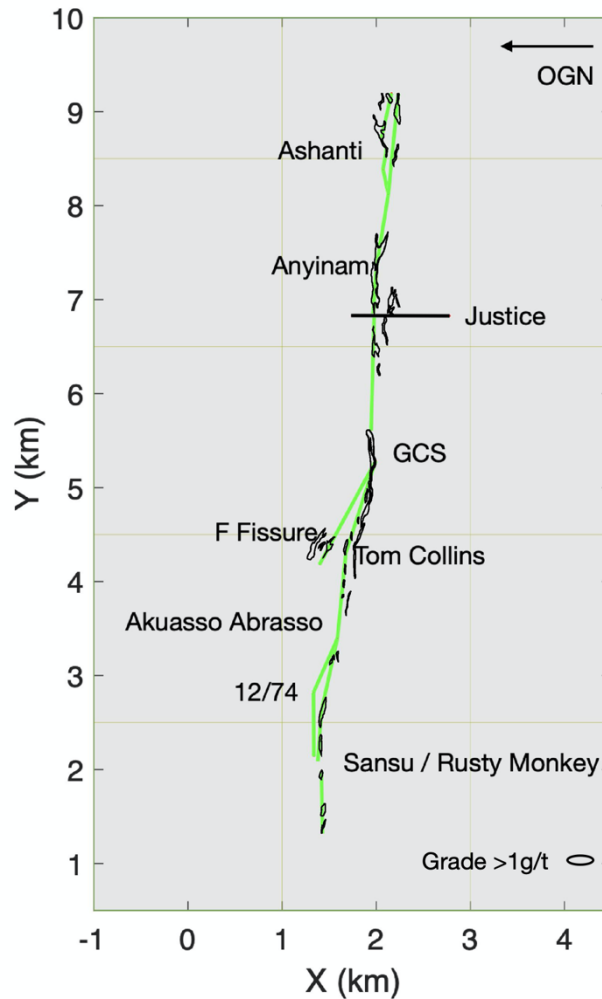
Figure 5.15: A plan view of fault elements in the simplified vertical Obuasi extent, model 1, with polygons representing grades greater than 1 gram per tonne at surface level after Oliver et al. (2020).

5.4.2.1 Model 1

Model 1 of the Obuasi fault system is the most simplified representation of the deposit and its behaviour during gold emplacement, representing an approach that a geologist might take with limited access to data. Model 1 is comparable with those in Micklethwaite and Cox (2006), where vertical faults were used. Lobate positive stress zones and stress shadows are recorded in association with stepover-zone fault terminations and points of curvature. Positive regions appear across the stepovers consistent with mineralising stepover models (e.g. Cox and Ruming 2004;

Micklethwaite and Cox 2004; Micklethwaite and Cox 2006). These regions show some correlation to zones of mineralisation. Mineralisation for grades >1g/t is shown in Figure 1.16, combined with the results from the D5$_{Ob}$ vertical dip model.

Figure 5.16: Mineralisation surface traces >1g/t, shown overlying Coulomb stress change patterns at 100m depth for 0.1m of sinistral strike-slip movement, on a simplified vertical model of the Obuasi fault system, resolved on optimised strike-slip (A.), thrust (B.) and normal (C.) faults.

Grades greater than >1g/t show some correlation to regions of high positive Coulomb stress. This correlation is stronger for optimised strike-slip faults than for those of the normal faults and optimised thrusts. High gold grades are generally associated with positive Coulomb stress changes; however the majority of Coulomb stress zonation is not associated with mapped high gold grade. Especially for the laterally extensive lobe structures emanating from rupture tips, no strong gold mineralisation has been recorded.

The correlation between high gold grade ore shoots and areas of positive stress is best across the GCS stepover, which is strongly mineralised directly across the structure and at the Ashanti Fissure. Mineralisation on the tip of the F Fissure to the

Obuasi grid west, as it diverges from the main Obuasi Fissure, correlates to positive Coulomb stress changes resolved on optimised thrust faults. The large zone of positive static stress calculated from Tom Collins up to GCS contains an extensive section of high gold grade but extends up to 1km away to the Obuasi grid north. The areas surrounding the Sansu/Rusty Monkey stepover and to Obuasi grid west of the Justice Fault are least well linked in this model. This is particularly true for the area around the Justice Fault. The effect of this large oblique fault on seismicity and fluid flow is poorly constrained in the literature.

5.4.2.2 Model 2

The results for model 2 indicate that adding non-vertical dip creates patterns of positive CST which are closer to the fault system and less laterally extensive in lobes. A comparison of high gold grade zones and results calculated at 100m depth is presented in Figure 1.17. The 100m depth calculation has been chosen as gold grade zones are traced from surface and are unlikely to be representative for the entire down dip extent of the deposit.

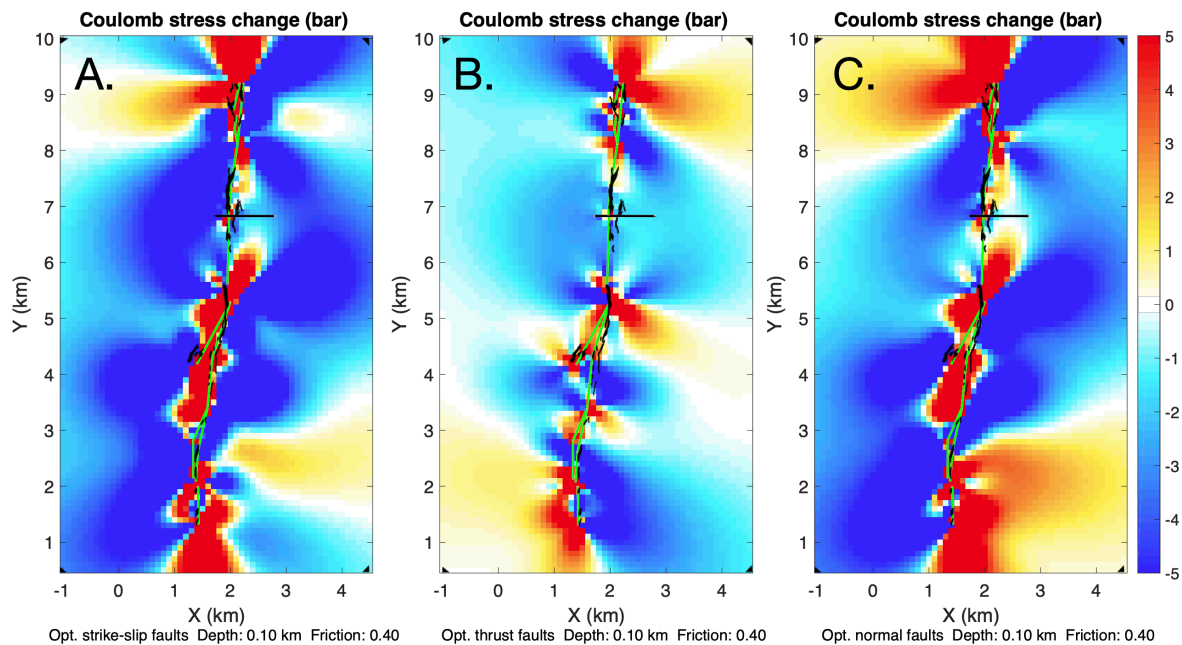*Figure 5.17: Mineralisation surface traces >1g/t, shown overlying Coulomb stress change patterns at 100m depth for 0.1m of sinistral strike-slip movement, on a variable dip model of the Obuasi fault system, resolved on optimised strike-slip (A.), thrust (B.) and normal (C.) faults.*

The correlation between high gold grade and static stress transfer is stronger in this model than model 1, particularly when resolved on strike-slip faults. For the strike-slip model, high grade ore shoots at Ashanti, Anyinam, GCS stepover, and Sansu/Rusty Monkey are directly related to zones of strong positive Coulomb stress. A strong correlation is achieved at Sansu/Rusty Monkey, where the fault dip switches from Obuasi grid north to south. Positive stresses around Akuasso Abrasso neatly contain the observed gold grade at the tip of the F Fissure, which is stronger than model 1, and the GCS, Ashanti, and Sansu/Rusty Monkey stepover structures contain mineralisation as expected.

The Tom Collins section is not contained within positive stress change sections for strike-slip and normal faults. It is however contained within calculations for optimised thrust faults. The gold-containing, variably orientated, small-displacement faults and fractures might therefore be more likely to have reverse senses of motion at this

location. Despite exhibiting oppositely orientated lobate shadows, the thrust-resolved model still exhibits some correlation to mineralisation.

The notable exception across all resolved fault types is the Justice Fault. Although correlation is improved from model 1, a new trend is observed in the stress changes calculated using this model. A curved band of positive Coulomb stress appears from the GCS stepover to the Obuasi grid south section of the Justice Fault. This has no evidence of high grade mineralisation from the polygon source used to generate this figure (Oliver et al. 2020) but might correlate with the Cowsu/Cowsu South open pits which appear in Allibone et al. (2002) (Figure 5.18). When a small reverse component was added to the model, macro-scale distributions of stress were largely unchanged (model 2b). This is interpreted to mean that small components of reverse slip were likely occurring as suggested by Allibone et al. (2002), but this did not affect the distribution of aftershock sequences significantly.

5.4.2.3 Model 3

The addition of GCS down dip flexure creates a closer representation in the model of the geometry at Obuasi. The limited cross-section availability (Oliver et al. 2020) means that this is still a significant simplification. The CST results for this model show an intensification of the curved band of Coulomb stress which appears to correlate with Cowsu South. Allibone et al. (2002) represent this as a small open pit, however it is absent from the high grade zones in Oliver et al. (2020). Good correlation continues to exist in the other parts of the deposit, where the model is like model 2. Figure 5.18 shows the deposit modelled at 100m depth including the down-dip flexure, with the location of Cowsu South and other open pits of Obuasi.
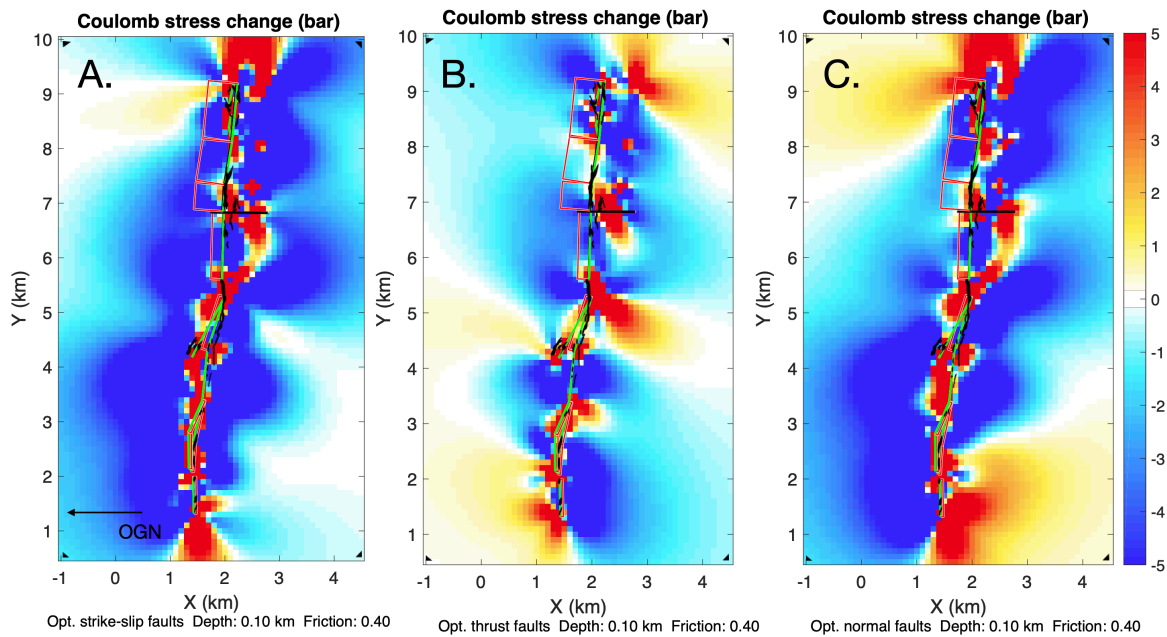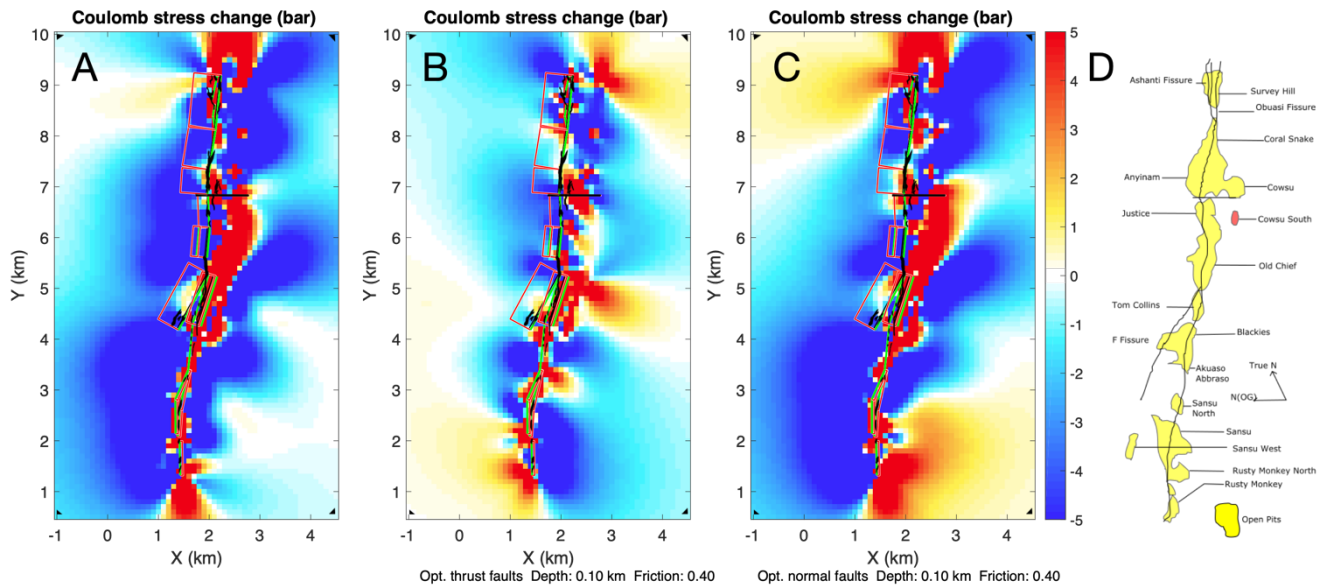
Figure 5.18: Mineralisation surface traces >1g/t, shown overlying Coulomb stress change patterns at 100m depth for 0.1m of sinistral strike-slip movement, on a variable dip model of the Obuasi fault system including the GCS flexure, resolved on optimised strike-slip (A.), thrust (B.) and normal (C.) faults. D. The open pits of Obuasi after Allibone et al. (2002)*.*

The enhanced band of positive stress originating at the GCS region for strike-slip and normal faults does not cover all the mineralisation across the GCS stepover in this model, although the positive zone is within 100m of the high gold grades. The accuracy of down-dip simplification of the GCS flexure may impact these results. There is a much more significant change in Coulomb stress between 100m and 600m depth in model 3 than the change observed between 100m and 500m depth in model 2, because of the dip changes at depth with this model. Grade polygons for ~600m depth, Obuasi level 29 (Oliver et al. 2020) are presented in Figure 5.19. Black lines on fault elements represent calculation depths, which generally align with the fault trace at level 29 but to a lesser degree than the surface trace due to fault

element dips being averaged along strike. The mineralisation map used for this trace extends past the Ashanti Fissure but finishes at Tom Collins.
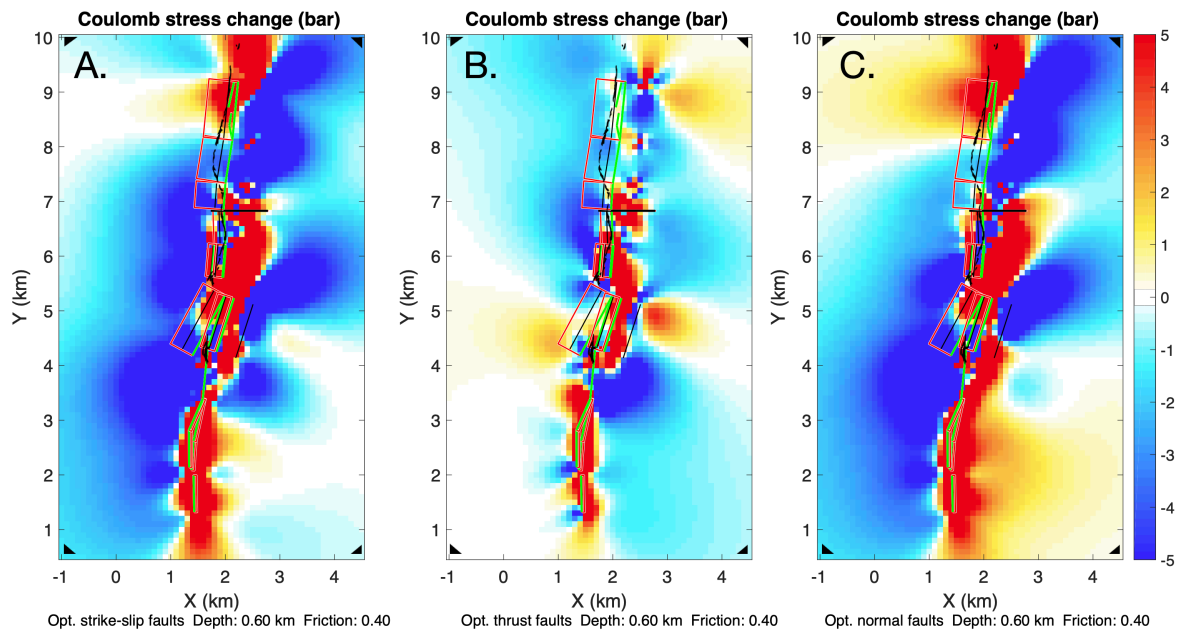
Figure 5.19: Mineralisation traces at 600m depth >1g/t, shown overlying Coulomb stress change patterns at 600m depth for 0.1m of sinistral strike-slip movement, on a variable dip model of the Obuasi fault system including the GCS flexure, resolved on optimised strike-slip (A.), thrust (B.) and normal (C.) faults.

For strike-slip and normal faults, a correlation with positive Coulomb stress change is strong through Ashanti and reasonable below the Justice Fault through to GCS and Tom Collins. Mineralisation between Ashanti and Anyinam is not included in a zone of positive Coulomb stress. This could be associated with a different mineralisation stage, or a process not related to stepover focusing. Correlation is particularly poor for thrust faults at this depth, with only the Obuasi grid east section of the GCS stepover showing any real correlation. The Cowsu South positive stress band is closer to the fault at this depth, suggesting grades might dip to the Obuasi grid north with depth from the Cowsu South pit.

.

When visually compared to gold grades >1g/t after (Oliver et al. 2020), correlation is slightly poorer than that of model 2 and greater than the vertical idealisation of model 1. The geometry of the GCS flexure has a controlling effect on the Cowsu south

positive Coulomb stress band. Improvements made to the flexure geometry within the model from more extensive sections could potentially improve the correlation seen using this model. Geometry down dip impacts the CST distribution, however representing this effectively in Coulomb 3.3 is challenging.

5.4.3 Results for D2$_{Ob}$

D2$_{Ob}$ is interpreted to have been a major gold emplacement event, coeval with the end of basin inversion at Obuasi, in which the disseminated sulphide-hosted ore generation was emplaced into the large-scale shear zones of the Obuasi, F and 12/74 Fissures. The mechanism for this emplacement is inferred to be fault-valve behaviour on high-angle reverse faults and shears after Sibson et al. (1988). Obuasi's major D2$_{Ob}$ shear zones are high-angle shear zones of significant vertical extent, formed under greenschist metamorphic facies.

The cyclical process is not well represented by optimally orientated fault modelling in this case. The CST results of models 4 and 5 contrast with the successful results of models 1-3, showing static stress patterns that might have been produced during D2$_{Ob}$. Confidence in how representative the fault models are is lower for D2$_{Ob}$ than for D5$_{Ob}$, because of the numerous deformation events which altered the faults into their observed geometries in the present.

Although mineralisation timing at Obuasi is debated (Blenkinsop et al. 1994; Oberthur et al. 1995; Oberthür et al. 1998; Allibone et al. 2002; Fougerouse et al. 2016; Fougerouse et al. 2017; Oliver et al. 2020), there is a strong suggestion that the majority of disseminated, arsenopyrite associated mineralisation was emplaced during D2$_{Ob}$, some of which was remobilised during D5$_{Ob}$. The generation of quartz vein-hosted free gold in low displacement faults and fractures is variably attributed to D2$_{Ob}$ (Oberthur et al. 1995; Oliver et al. 2020) and D5$_{Ob}$ (Allibone et al. 2002; Fougerouse et al. 2017). These could have also been reactivated D2$_{Ob}$ structures additionally mineralised during D5$_{Ob}$. The aftershock driven permeability of these low displacement structures has been shown to have been favourable to mineralisation during D5$_{Ob}$, and good correlations using the aftershock theory have been achieved using models 1, 2 and 3. The mechanism of emplacement for disseminated

sulphide-hosted gold is interpreted here to have been a result of fault-valve cycles. This investigation is designed to test whether the gold grade in low displacement fault can be explained as a $D2_{Ob}$-only event using aftershock modelling.

5.4.3.1 Model 4

This model is constructed using idealised high-angle reverse faults, with generalised dips of 70°. Stepover geometries have been retained, as accurate reconstruction is not available. This is an approximate representation of the fault system at the end of basin inversion, although Feybesse et al. (2006) orient the Obuasi fault system similarly to this study at peak gold emplacement. The surface high grade gold distribution from Oliver et al. (2020) has been overlaid on 100m depth results without transfer behaviour from the Justice Fault in Figure 5.20.

Figure 5.20: Mineralisation surface traces >1g/t, shown overlying Coulomb stress change patterns at 100m depth for 0.1m of reverse strike-slip movement on individual fault elements of an idealised high-angle reverse fault model of the Obuasi fault system, resolved on optimised strike-slip (A.), thrust (B.) and normal (C.) faults.

This model exhibits no obvious visual correlation between positive zones of CST and mineralisation. Some association between the resource distribution and positive

Coulomb stress is observable with Model 4a, however whether this is incidental or related is unclear. When compared to the close associations observed for $D5_{Ob}$ it is clearly weak. For optimised strike-slip faults, curved regions of positive Coulomb stress extend from OG south of the Ashanti fissure to Anyinam and from OG south of GCS through to the 12/74 Fissure, which encompasses the majority of high-grade mineralisation. However, large lobate shadows extending OG southward in the footwall of the system and most of the positive stress sections encompassing mineralisation are indicated as poorly mineralised by the grade polygons. Notably, the GCS mineralisation is strongly negatively stressed in this model. Similar patterns are observed for optimised normal faults.

Optimised thrust faults should be the best choice of receiver fault to represent the original conditions given the compressional regional stress regime (Steacy et al. 2005). For model 4 (Figure 5.20), mineralisation sits in a zone of close to net zero stress change, while the hanging wall undergoes low magnitude positive stress change. A band of positive stress spots are observed ~800m to the OG south of the measured resource, which might be interpreted as anomalous consequences of overlap and underlapping fault elements. Overall, patterns observed for this model do not visually correlate enough to observed mineralisation zones to be considered successful in using aftershock modelling to explain the distribution of gold at Obuasi using $D2_{Ob}$ alone. The aftershock distribution was instead likely to have been distributed distally off fault, promoted by positive Coulomb stresses but not focused into structures which control the location of ore shoots, or along propagating the fault itself, where mineralisation is observed in disseminated sulphides.

Transfer behaviour on the Justice Fault was additionally modelled (model 4b). It is clear from this model that transfer movements on the Justice Fault introduce positive stress changes around the Justice Fault, but the spatial trend of Coulomb stress observed in Figure 5.20 is largely unchanged with the introduction of transfer behaviour. Although this was likely to have occurred during $D2_{Ob}$ (Allibone et al. 2002), this was not interpreted to have created a significant fluid pathway.

5.4.3.2 Model 5

Improvements in correlation were made between models 1 and 2 for $D5_{Ob}$. This also occurs between the $D2_{Ob}$ idealised high-angle model (model 4) and the variable dip model presented here in Figure 5.21 (model 5). For optimised thrust faults, correlation is still poor at the Ashanti end of the fault system; however, the Ashanti mineralisation is interpreted as $D5_{Ob}$.

Positive Coulomb stresses calculated in the footwalls of the OG southward dipping fault elements around Sansu/Rusty Monkey directly encompass the mineralised zones. Mineralisation around the F Fissure and GCS is also encompassed by positive Coulomb stresses. Improvement in correlation is also observed for optimised strike-slip and normal receiver faults, particularly as the distal band of lobate shadows is brought much closer to the fault system, within 200m of the fault system along most of its length.

Despite a closer correlation achieved using this model, it is still unclear that the association is indicative of an aftershock-gold relationship during $D2_{Ob}$. The much wider regions of positive Coulomb stress calculated for $D2_{Ob}$ when compared to results for $D5_{Ob}$ make incidental correlation more likely.
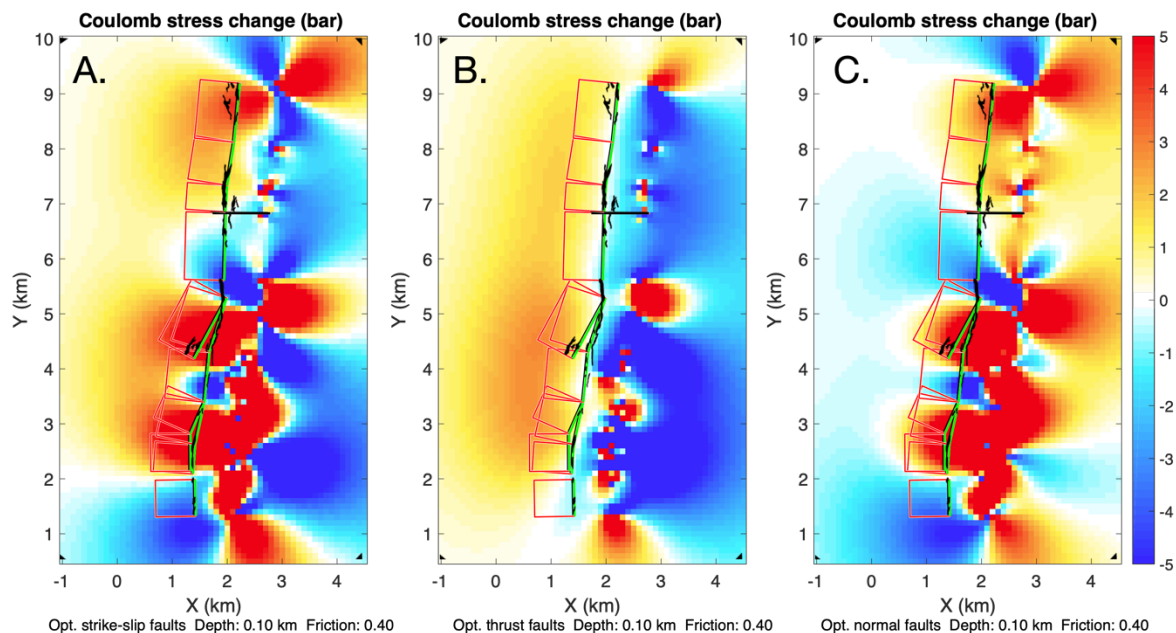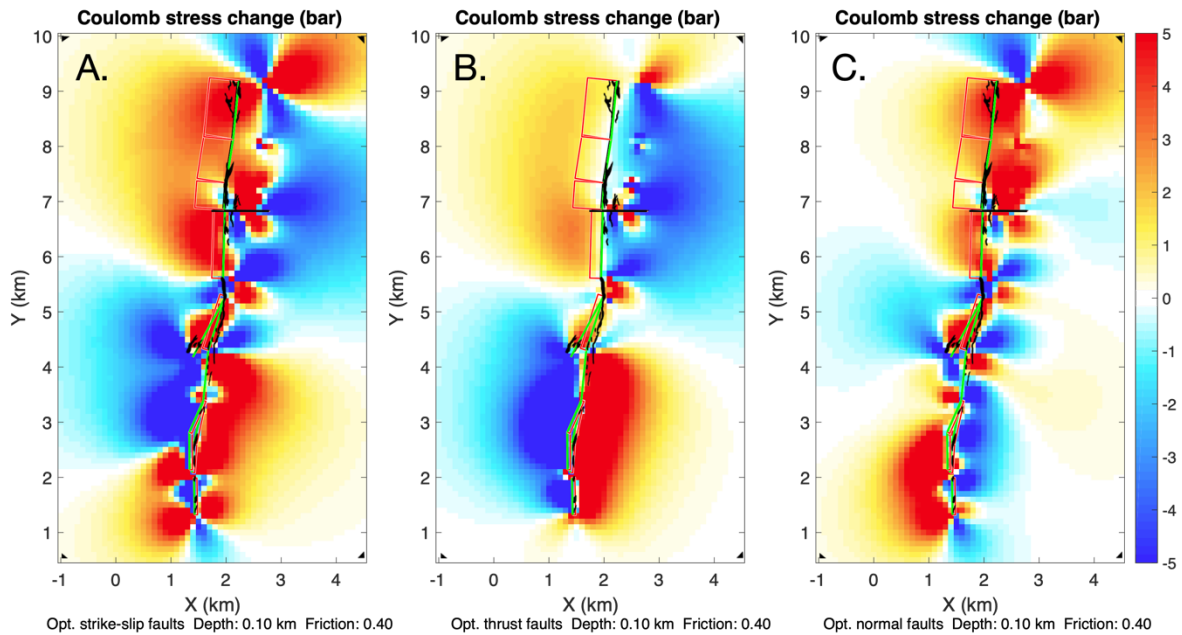
Figure 5.21: Mineralisation surface traces >1g/t, shown overlying Coulomb stress change patterns at 100m depth for 0.1m of reverse strike-slip movement on individual fault elements of variably dipping fault model of the Obuasi fault system, resolved on optimised strike-slip (A.), thrust (B.) and normal (C.) faults.

This remains true with depth, where the stress changes modelled using this model become less intense, reduced to around 2 bars at the Ashanti end of the fault. The calculated stresses for 500m depth are presented with level 29 mineralisation in Figure 5.22. The associations of positive stresses with high grade noted in Figure 5.21 are still present at depth but appear to be a consequence of reverse faulting preferentially stressing the hanging wall rather than focusing because of geometry. As mineralisation at Obuasi is found closely associated to faults, stress correlation appears to be more incidental than the model for D2$_{Ob}$, where, as with model 4 aftershock distributions were more likely to be distal and unfocused or propagating along fault.

Mineralisation at depth is poorly constrained past Tom Collins (Oliver et al. 2020), and no strong direct correlation is observed for high gold grade and positive Coulomb stress for the mineralisation (Figure 5.22). This further supports the conclusion that D2$_{Ob}$ mineralisation was not controlled by aftershock sequences.

This is corroborated by the addition of transfer behaviour which, when added to this model, creates larger lobate stress shadows with no direct correlation to mineralisation. The transfer fault can be interpreted to have formed because of the compressive regime, but likely played no part in focusing any mineralising seismicity.
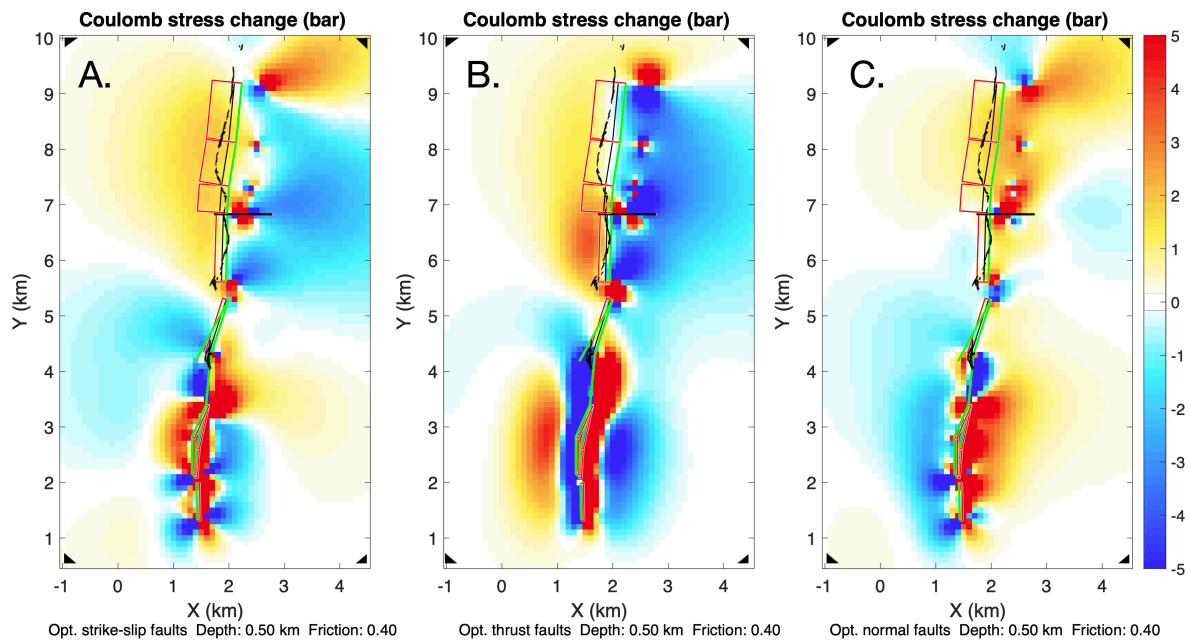
Figure 5.22: Mineralisation surface traces >1g/t, shown overlying Coulomb stress change patterns at 500m depth for 0.1m of reverse strike-slip movement on individual fault elements of variably dipping fault model of the Obuasi fault system, resolved on optimised strike-slip (A.), thrust (B.) and normal (C.) faults.

Neither of the CST results from the D2$_{Ob}$ models show strong correlations between positive static stress transfer and gold mineralisation. Positive Coulomb stresses can be observed to coincide with zones of mineralisation; however, the zones of positive stress are large, upwards of 2km in width in many places, and the zones of mineralisation are small and closely associated with the fault system, which defines the stress change. The lack of a direct spatial association such as those achieved when modelling D5$_{Ob}$ could suggest that any association between positive stress changes and resource grades is coincidental and the aftershock distribution during D2$_{Ob}$ was not a major control on the spatial distribution of gold off-fault.

Several deformation events which occurred between $D2_{Ob}$ and the present, therefore it is possible that the subsequent modification of fault geometries has impacted the accuracy of this study. Model 5 is the closest estimate that can be achieved from the literature available, however a closer estimate could be achieved with targeted study specifically aiming to produce an accurate palinspastic reconstruction. With this data, it is possible that better correlations could be achieved for $D2_{Ob}$.

5.4.4 Remobilisation

There is discussion about the process of gold remobilisation at Obuasi (e.g. Allibone et al. 2002; Fougerouse et al. 2016; Fougerouse et al. 2017). Fougerouse et al. (2016) conclude emphatically from geochemical evidence that a first generation of arsenopyrite-hosted Au ($D2_{Ob}$) interacted with a later generation ($D5_{Ob}$) of low volume, low S2, high NiCl2 fluid, which liberated gold in solution. Later work (Oliver et al. 2020) supports the theory of a multiple stage emplacement of gold at the Obuasi deposit, including the field evidence, particularly with regard to the multiple gold deposition modes, disseminated sulphide-hosted and quartz-vein-hosted native gold being the majority contributors. The suggestion that $D5_{Ob}$ gold was derived from remobilisation of $D2_{Ob}$ sulphide-hosted gold has the merit of aligning with typical mineralisation timings as expected for orogenic deposits after Groves et al. (1998), during the late stages of basin inversion. However, Fougerouse et al. (2017) acknowledge preservation of arsenopyrite zonation observed by Oberthür et al. (1997), suggesting that remobilisation did not occur.

Remobilisation at the Obuasi deposit is suggested to have transported gold in solution distances of the order of tens of metres (Fougerouse et al. 2016). The Coulomb stress-transfer modelling results for this chapter are resolved on $100m^2$ grids. The spatial gold distribution at this scale may not have been greatly affected by remobilisation. Good correlations achieved in areas of positive stress-transfer and the locations of mineralisation for $D5_{Ob}$ would imply that at least some of the Obuasi gold emplaced in this later event may be from a new source and is not simply remobilised from existing $D2_{Ob}$ deposit architecture. This is supported by consistent enrichment around stepover regions and the emplacement of gold in the $D5_{Ob}$

Ashanti Fissure zone, which may be too distant from larger structures to have been formed by pure remobilisation. The distribution of gold during $D2_{Ob}$, assuming fault-valve behaviour, may have been almost exclusively controlled by the distribution of high-angle reverse faults, with minimal aftershock-related permeability control. A potentially newly mineralising and remobilising fluid during $D5_{Ob}$ is therefore proposed to have exploited reactivation of these gold-rich shear zones and, under more brittle rock conditions utilised aftershock-driven permeability to enrich the deposit, particularly in the stepover regions of Ashanti, GCS and Sansu/Rusty Monkey.

5.4.5 Model accuracy

The models in this thesis are based on maps and section publicly available (Oliver et al. 2020), with simplifications made as described in section 5.2 Methods. In the variable dip examples (models 2, 3 and 4), change in CST is observed with depth. Depth extents for faults in this model are also taken from Oliver et al. (2020). The depths provided are closely linked to mineralised extent meaning large portions of unmineralised faults and shears at depth might be omitted from the figure. These models therefore do not likely represent the full depth extent of the faults at Obuasi, particularly in the west (OG), where the mineralised extent is significantly shallower, and the available cross sections are correspondingly shallower. The faults likely extended deeper than those recorded in the paper, but owing to no accurate indication of their geometry, greater depth extents have been omitted from the models. Representing the GCS flexure was particularly challenging using the limited number of sections presented in Oliver et al. (2020). The lateral extent of the model has been defined by the extent of the detailed map in Oliver et al. (2020). Lobate Coulomb stress changes which appear at the fault tips are likely to be spurious, as the faults may extend further than the detailed extents available. This does not impact the results achieved on the targeted stepovers.

The fault geometries which are observable and mapped at Obuasi were produced over an active period of ~30Ma, from metamorphism and inversion of the Kumasi Basin starting ~2115Ma, through a transition to sinistral wrench faulting ending ~2085Ma (Oliver et al. 2020). $D5_{Ob}$ occurred toward the end of this period, and

therefore the modern position of faults can be used with reasonable certainty to represent those of D5$_{Ob}$ faults. With the earlier D2$_{Ob}$ generation, the position of the faults is much less certain. Simplifying the D2$_{Ob}$ generation of high-angle mineralised shear zones to high angle reverse faults after Sibson et al. (1988) is an idealised concept of what these might have looked like. These orientations and extents are less certain than the geometries inferred during D5$_{Ob}$, with the impacts of D3$_{Ob}$ and D4$_{Ob}$ between the current location of faults and their position during D2$_{Ob}$.

5.4.6 Mainshock seismicity choice

The mineralised section of the Obuasi fault system extends for approximately 8km along strike. Using fault scaling relations as reviewed by Torabi and Berg (2011), a typical, moderately sized strike-slip or reverse seismic event for a system of crustal rocks with this lateral extent is between ~0.1 and ~1m, which equates to a seismic moment between 5 and 6 Mw. There is little information available on the total displacement of faults at Obuasi, save for an estimated ~200m of movement on the Ashanti Fissure (Allibone et al. 2002), suggesting that D5$_{Ob}$ stresses induced relatively small displacements on faults. D2$_{Ob}$ is interpreted to have occurred towards the regional, late stage of basin inversion, and so it is possible that the large-scale shear zones underwent significantly larger displacements overall, although the majority was likely pre-mineralisation. The individual displacements chosen for modeling therefore represent moderate size events in the formation of the total displacements, with appropriate reverse components where applicable. The combined-slip approach used here after Micklethwaite and Cox (2006) is intended to represent the average distribution of Coulomb stresses that would be expected over multiple failure events on the fault system.

Because the events which mineralised the deposit may have occurred over many seismic cycles, it is possible that cumulative Coulomb stresses had an effect on distribution (Mildon et al. 2019), however this theory is not well established. Cumulative stresses cannot be modelled for the Obuasi deposit as a contemporary seismic record is required. The seismicity choices applied here represent moderate

size earthquake events which likely occurred thousands to tens of thousands of times to mineralise the system. Stresses will have evolved throughout these events.

5.5 Conclusions

This aim for this chapter was to apply stress-transfer modelling to the entire extent of the Obuasi fault system, to investigate two potentially mineralising events that have been identified in the Obuasi related literature. The stress-transfer technique under the strike-slip regime $D5_{Ob}$ produced strong correlations with locations of high gold grades at the deposit, which suggests that this may have been an independent mineralising event from the $D2_{Ob}$ mineralization with aftershocks exerting a control on the transport and distribution of gold. Stress-transfer modelling of $D2_{Ob}$ did not produce good correlation between mineralisation grades and areas of positive Coulomb stress for Obuasi. This result may be because during $D2_{Ob}$ the aftershock distribution was during reverse fault was distributed between widely spaced off-fault events and along the fault itself in fault-valve overpressure rupture cycles, which are not modelled. The lack of correlation between STM model results and mineralization could also be linked to the impact of geometry modification from post $D2_{Ob}$ deformation events. The lack of correlation achieved here suggests that for applying STM systems to formed under reverse faulting conditions, the mechanics of emplacement and aftershocks should be carefully considered.

Chapter 6.

Fault-Valve Behaviour of the Obuasi Fault System-D2$_{Ob}$ Stress on Faults

6.1 Introduction

Chapter 5 demonstrates that the influence of post-seismic static stress on aftershock-driven permeability, after Cox and Ruming (2004); Micklethwaite and Cox (2004) and Micklethwaite and Cox (2006) does not correlate to the distribution of D2$_{Ob}$ ore shoots. This is inferred to be due to the predominant influence of high angle reverse fault-valve cycles during this mineralising stage (Sibson et al. 1988), which may not have produced focused aftershock distributions controlling ore shoots, but rather a more general pattern of distal aftershocks and propagation along fault. Post D2$_{Ob}$ fault modification may also have impacted the experiment. High angle reverse faults generally refer to reverse faults with dips of around 70°, which are non-Andersonian in character (Anderson 1905). When reverse faults dip greater than ~54°, assuming Coulomb failure criterion style frictional processes in a compressive regime, fluid pressure is a requirement to overcome lithostatic stresses (Sibson et al. 1988). In this chapter, an investigation of possible fault valve behaviour is made using an idealised high-angle reverse fault model for D2$_{Ob}$. The D2$_{Ob}$ shear zones at Obuasi are unfavourably oriented to failure with relation to the D2$_{Ob}$ regional stress field, particularly due to their high angle of dip, which contradicts Andersonian fault mechanics (Sibson 1990). Failure on D2$_{Ob}$ fault zones is therefore interpreted to occur due to cyclic over-pressured fluid build-up, which overcomes lithostatic stress. The process is described by Sibson et al. (1988) as:

Prefailure, where pressure builds to supra-lithostatic in a fluid reservoir at depth.
Seismogenic fault failure, where accumulating shear stress from the pressure triggers fault failure and nucleates an earthquake, which propagates updip promoting fracture permeability.
Postfailure discharge, drainage of the fluid reservoir occurs under the released deviatoric stress, using the now permeable rupture zone and associated fractures.

Mineralisation and precipitation occur, especially because of abrupt drops in fluid pressure. Modern analogues suggest that the aftershock period is particularly favourable to the transportation and deposition of minerals.

Self-sealing, which makes fault-valve behaviour inherently cyclic, occurs where hydrothermal precipitates seal faults and fractures, effectively destroying the seismically induced permeability and potentially stopping pressures from returning to hydrostatic.

The cycle then repeats as the sealed fault allows for fluid pressure build up and eventually induces fault failure.

This chapter uses Coulomb 3.3 modelling of static stress change on user-defined source and receiver fault elements following a slip event (in this model representing a seismogenic fault failure event) to show that Coulomb stresses on high-angle reverse faults post-failure are negative. This indicates that following a rupture event, a high-angle reverse fault is unfavourable to repeated failure, meaning that the faults are likely to seal. This allows for repetition of the cycle. It is also shown that parts of the fault adjacent to an original rupture point undergo a positive static stress change, making them favourable to aftershock propagation or a new mainshock seismogenic fault failure, allowing multiple events to account for the significant endowment of gold at Obuasi along its strike.

This approach does not provide predictions for modern day ore shoot positions, as specific seismic events are not available from the record at Obuasi and the geometrical distribution method of (Micklethwaite and Cox 2006), as seen in Chapter 5, does not apply using this method. Instead, support for fault-valve theory of $D2_{Ob}$ mineralisation is presented here, as a potential explanation for difficulty in modelling $D2_{Ob}$ using stepover-based methods, and as the first application of this hypothesis to the Obuasi deposit. The impact of Coulomb stress on high-angle reverse faults is assessed by Micklethwaite (2008), who concludes that poroelastic load weakening is insufficient to trigger faults with dips >45° and for the Triumph fault, Kalgoorlie WA, an aftershock was a likely trigger. However, this study did not apply any stress-transfer modelling.

6.2 Methods

The idealised high-angle reverse fault model developed in Chapter 5 for optimally orientated receiver faults has been reapplied for this investigation. This model takes present-day surface traces of D2$_{Ob}$ shears from Oliver et al. (2020), simplifies along strike variation and applies 70° dips to all fault elements excluding the Justice Fault. The faults are modelled to a depth of 2km. Rock mechanics properties have been retained from the previous chapters (Young Modulus of 80 GPa, Poisson's Ratio of 0.25, and a coefficient of internal friction of 0.4) to represent fluid-saturated greenschist facies metamorphic rocks. A visualisation of this model is provided in Figure 6.1. Regional stress orientation is not used when calculating stress directly on faults in Coulomb 3.3. Coulomb stress changes are modelled on all fault elements in the model.

A 0.1m reverse slip (consistent with Torabi and Berg (2011)) was applied to all fault elements excluding the Justice Fault, a 1.2m total slip using the terminology of Micklethwaite and Cox (2006). This represents the entire Obuasi fault system undergoing a slip event, similar to the combined-slip method (Micklethwaite and Cox 2006). This illustrates the stress changes which occur post-failure with no receiver faults in the system.
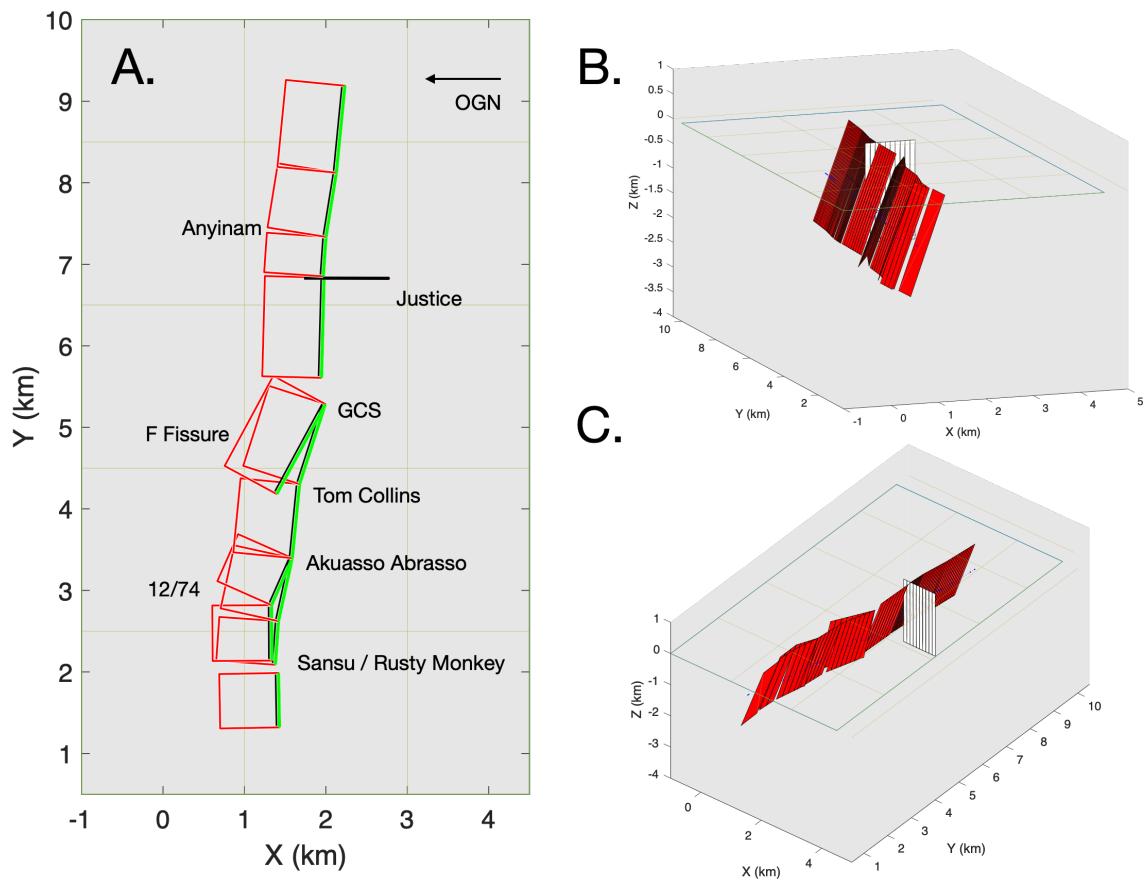
Figure 6.1: Visualising the high-angle reverse model. A. Plan view of high-angle reverse fault elements generalised to 70° B. & C. show 3D renderings of this fault system, viewing (Obuasi Grid) SE and NE respectively. The transpressional Justice Fault is white, while high-angle reverse fault elements are shown in red.

To represent a single source seismic event on the fault system during D2$_{Ob}$, investigating the effect on adjacent sections of the fault which do not slip, individual fault panels have been modelled with 0.5m of reverse slip. This is still within realistic bounds for a reverse fault seismic event as reviewed by Torabi and Berg (2011), and has an equivalent seismic moment of ~5Mw when compared to 0.1m of slip across all of the fault elements. Three hypothetical slips are modelled to illustrate: at the Sansu/Rusty Monkey flexure, on the F Fissure and at Anyinam, directly above the Justice Fault.

6.3 Results
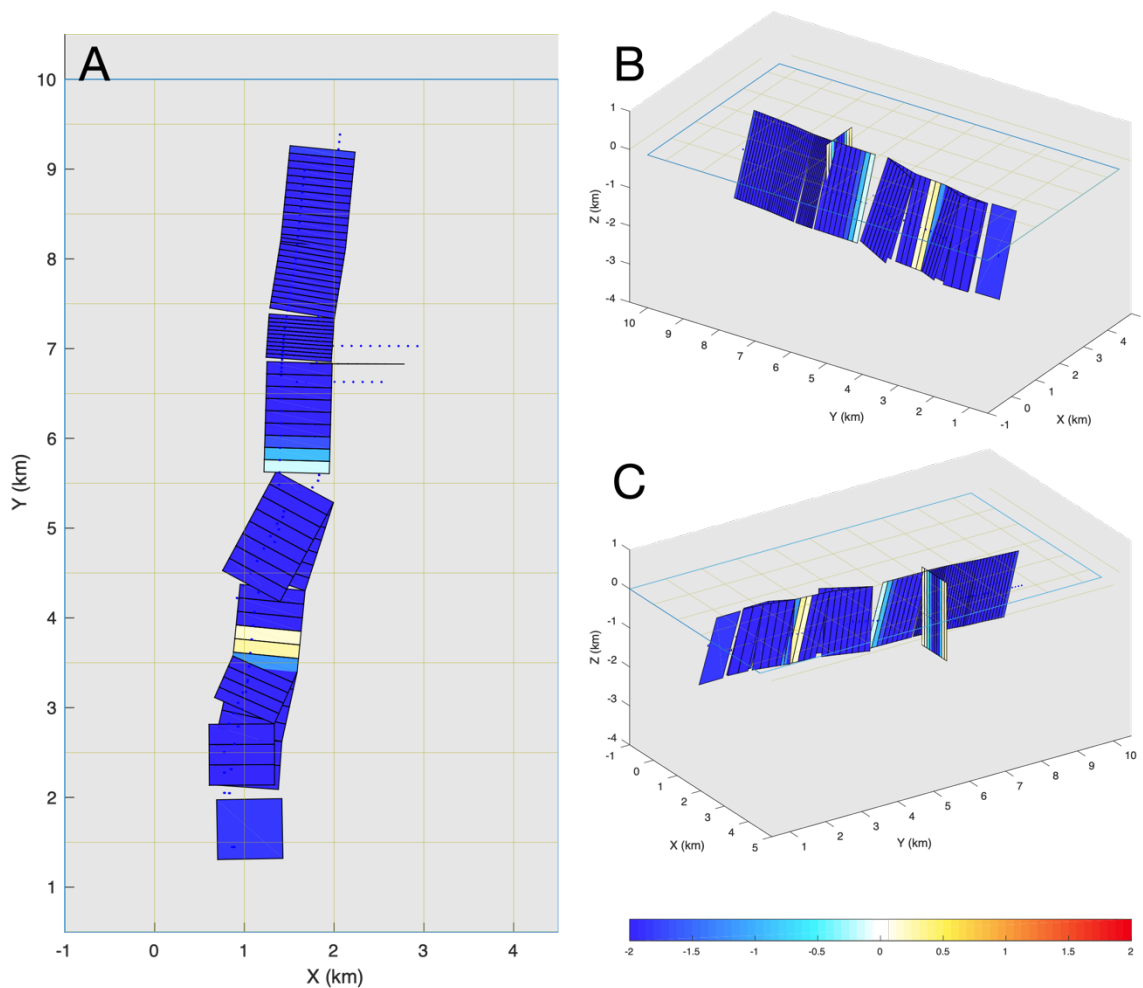
Figure 6.2: Stress changes on the Obuasi fault system following a 1.2m total combined slip (0.1m on each of fault element). Negative Coulomb stresses are calculated for almost all fault elements, with small exceptions around Akuasso Abrasso and GCS where Coulomb stresses for sections of fault elements trend to 0 bars net change and small positive values at Akuasso Abrasso. A. Plan view of high-angle reverse fault elements showing negative Coulomb stresses B. & C. show 3D renderings of the same results, viewing (Obuasi Grid) SE and NW respectively.

The resultant stresses for reverse movement of 1.2m total slip on the entire fault system are presented in Figure 6.2. Negative Coulomb stress change is calculated on the majority of the Obuasi fault system post failure. Exceptions include a small section of no static stress change at GCS and low, unlikely to induce aftershock (King et al. 1994), positive values at Akuasso Abrasso.

Illustrating how seismic events might progress laterally through the Obuasi deposit following a single seismic event, Figures 6.3, 6.4 and 6.5 show Coulomb stress changes following 0.5m of reverse movement on single fault elements at Sansu/Rusty Monkey, the F Fissure and Anyinam respectively.
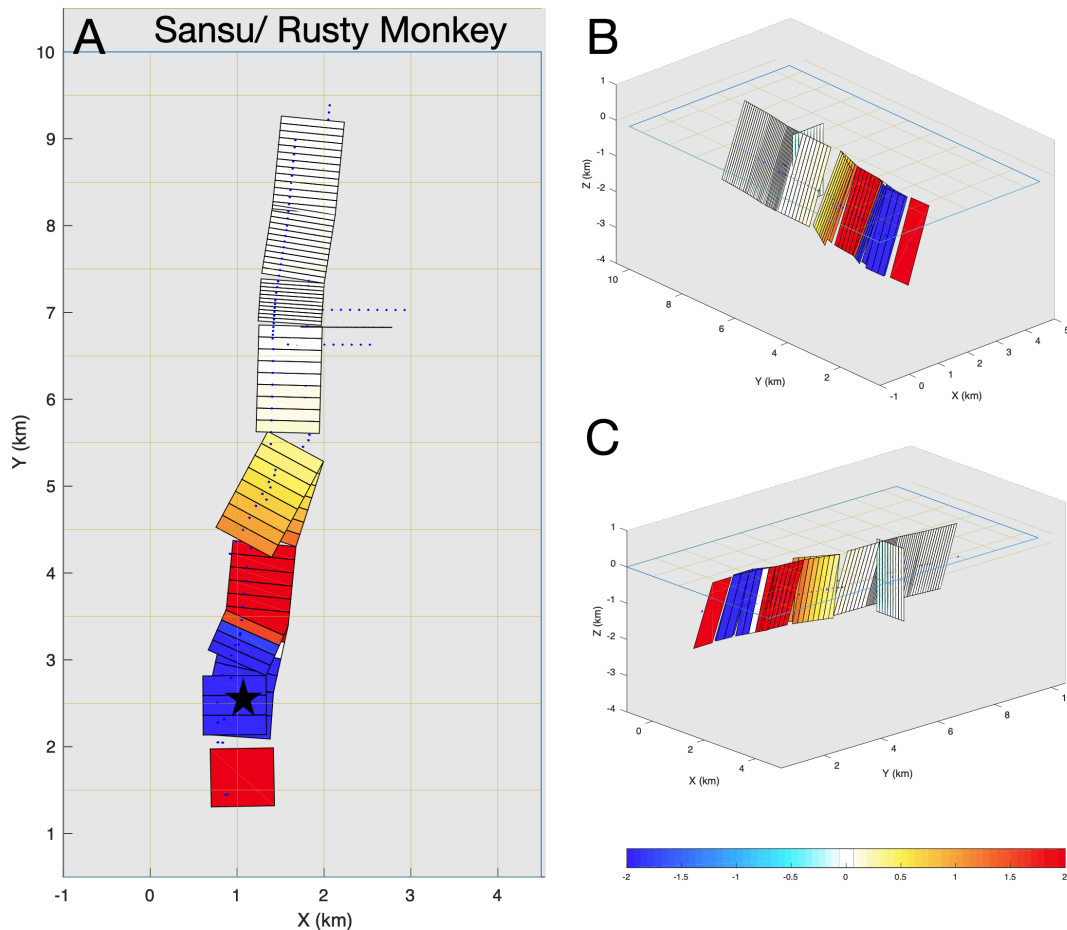
Figure 6.3: Stress changes on the Obuasi fault system following a 0.5m slip on the Sansu/Rusty Monkey ore shoot zone. Negative Coulomb stresses are calculated on the slipping fault element and those directly adjacent. Next to the negative values, high positive values are recorded, which gradually trend to 0 bars at distance. A. Plan view of high-angle reverse fault elements showing positive and negative Coulomb stresses. Seismic source fault is indicated with a star. B. & C. show 3D renderings of the same results, viewing (Obuasi Grid) SE and NW respectively.

For all cases, negative Coulomb stresses are recorded on the fault element which slips and those directly adjacent. These are then bounded by high positive stress, which gradually trends to net zero stress change.
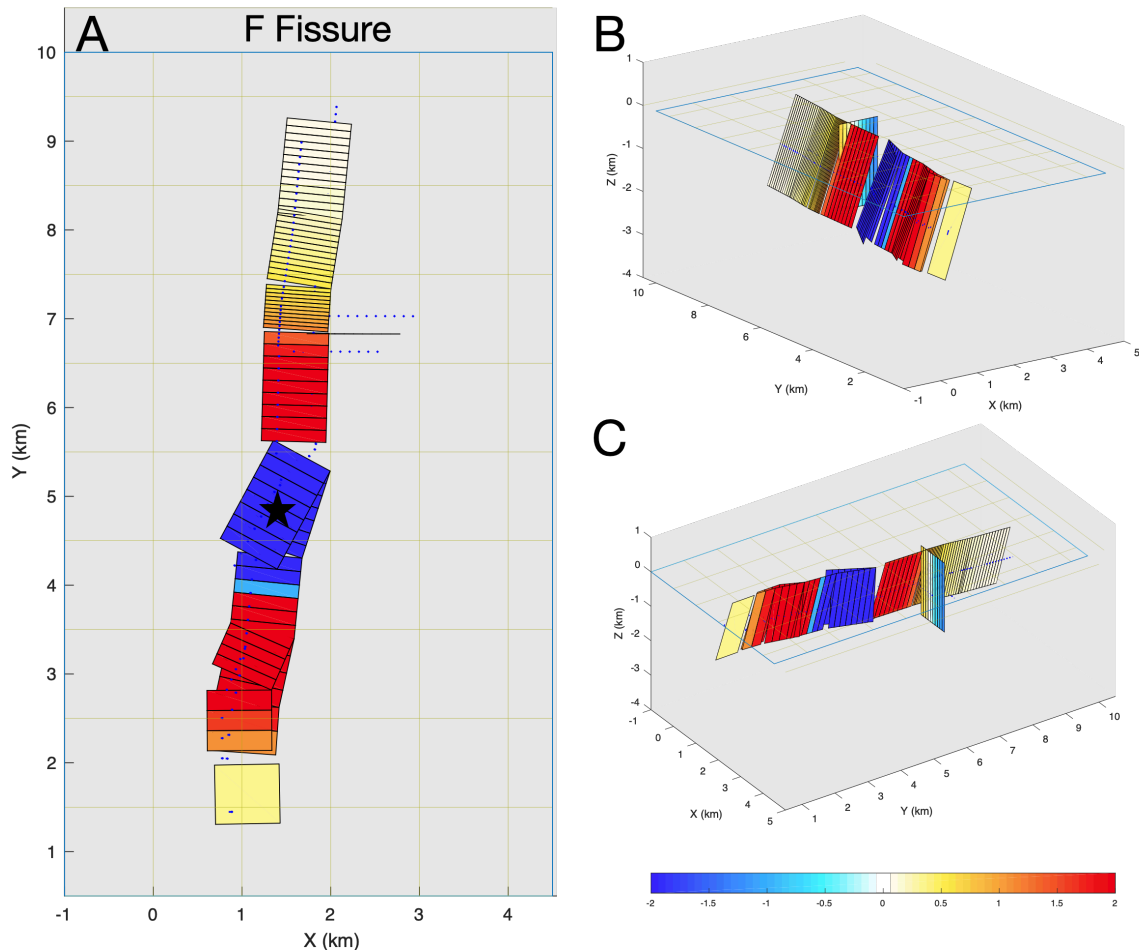
Figure 6.4: Stress changes on the Obuasi fault system following a 0.5m slip on the F Fissure. Negative Coulomb stresses are calculated on the slipping F Fissure and the section of the Obuasi Fissure directly adjacent to the F Fissure. Next to the negative values, high positive values are recorded, which gradually trend to 0 bars both Obuasi Grid east and west. A. Plan view of high-angle reverse fault elements showing positive and negative Coulomb stresses. A star indicates the seismic source fault. B. & C. show 3D renderings of the same results, viewing (Obuasi Grid) SE and NW respectively.

The relatively central position of the F Fissure failure modelled in Figure 6.4 shows that positive Coulomb stresses extend laterally equally either side of the failure.

From Figure 6.4, it can be seen that positive Coulomb stresses trend to 0 bars ~4km from the source fault for a relatively large seismic event (Torabi and Berg 2011).
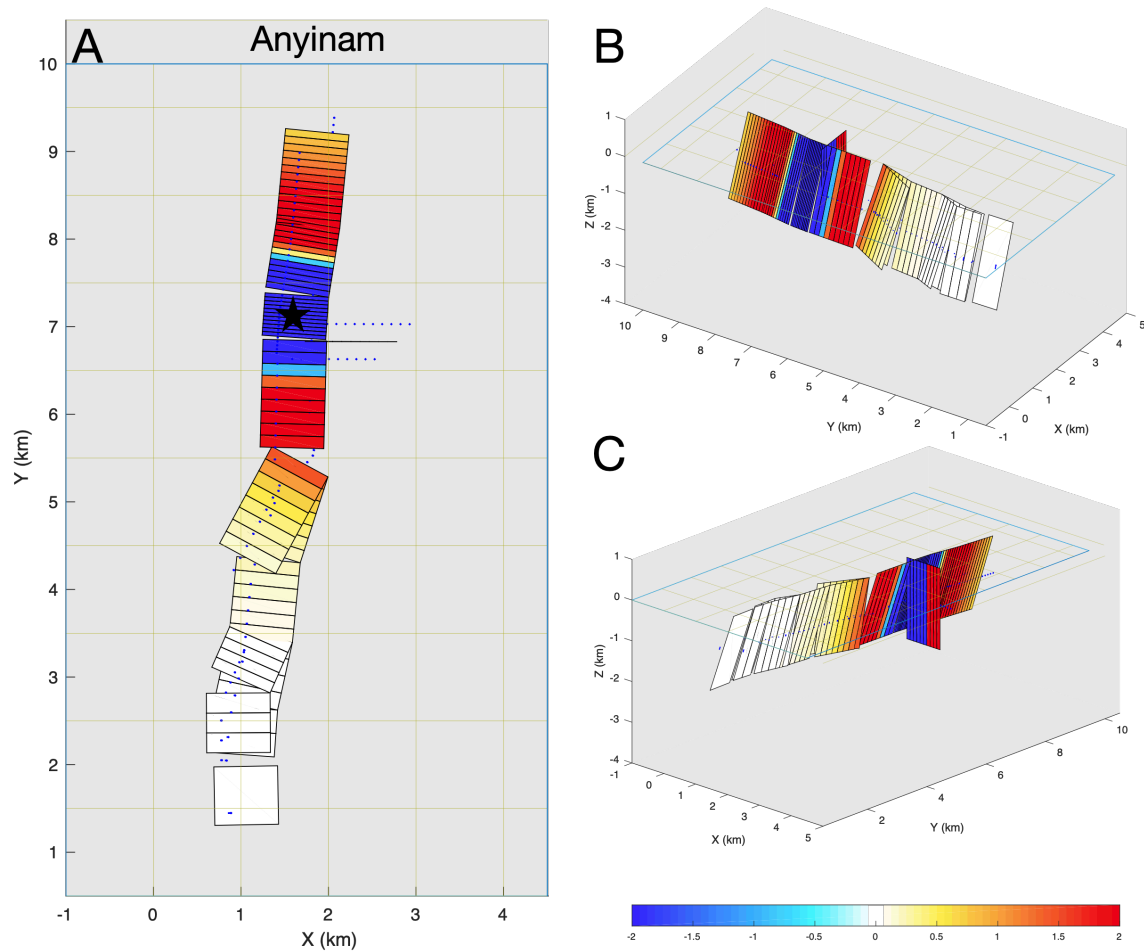
Figure 6.5: Stress changes on the Obuasi fault system following a 0.5m slip on the Obuasi Fissure by the Anyinam ore shoot, east (OG) of the Justice Fault. Negative Coulomb stresses are calculated on the slipping Obuasi Fissure and the sections of the Obuasi Fissure directly adjacent. Next to the negative values, as with Figures 3 and 4, high positive values are recorded, which gradually trend to 0 bars both Obuasi Grid east and west. A. Plan view of high-angle reverse fault elements showing positive and negative Coulomb stresses, seismic source indicated with a star. B. & C. show 3D renderings of the same results, viewing (Obuasi Grid) SE and NW respectively.

The transferred stress from a hypothetical D2$_{Ob}$ reverse slip event at Anyinam, shown in Figure 6.5 produces results along the length of the Obuasi fault system consistent with those at the F Fissure and Sansu/Rusty Monkey.

6.4 Discussion

The model used for this chapter is an approximation of conditions at Obuasi taken from present day geometries and idealised using typical dip characteristics of high-angle reverse faults (e.g. Sibson et al. 1988; Sibson 1990). Following D2$_{Ob}$, up to three distinct deformation events have been identified at Obuasi (Oliver et al. 2020), introducing generations of folds, faults and reactivations which will have changed the geometry of the fissures. Using an idealised model illustrates the effect of fault-valve seismicity in the context of Obuasi without a detailed fault reconstruction, which may explain the lack of correlation found in Chapter 5. Moment magnitudes of the seismicity applied to produce Figures 6.2-6.5 are ~5Mw. From modern analogues and fault scaling, these are realistic slips which illustrate fault behaviour well.

Shown in Figure 6.2, a combined-slip modelling approach has been applied to show the effect of a general reverse movement on the Obuasi fault system, which results in a negative Coulomb stress change on the majority of the system, with the exception of small, elevated values detailed above. The occurrence of low positive and zero bar stress transfer values is likely due to the variable strike geometry of the system as a whole and the addition of offshoots such as the F and 12/74 Fissures. A zero-bar stress change is recorded opposite the obliquely oriented F Fissure, while a small positive value is recorded close to the oblique intersection of the 12/74 Fissure. This is not positive enough to have impacted mineralisation patterns over time as it is not likely to have increased Coulomb stress enough to induce failure (King et al. 1994). The majority of the deposit is negatively Coulomb stressed by at least -2 bars, which makes the fault unfavourable to reactivation by overcoming friction (King et al. 1995). This likely represents the 'post-failure discharge' to 'self-sealing' stages of fault-valve behaviour, where the fault system has been returned to lithostatic stress conditions with low fluid pressure and becomes unfavourable to seismicity.

Figures 6.3, 6.4 and 6.5 show the calculated Coulomb stresses for more localised reverse slip events. The fault elements chosen to slip are selected to represent movements in three different locations in the deposit, however any of the fault elements in the model could have been used and would show similar impacts on the surrounding fault. As demonstrated in the results shown in Figure 6.2, source fault elements which experience reverse slip are calculated to have strong negative stress values. This is not limited to the source fault, but also those immediately adjacent. This indicates that a smaller source can impart negative stresses to its receiver fault neighbours, and a source reverse slip is not required to induce a negative static stress change. Immediately next to the negatively stressed fault elements, ~1km from the source fault for this magnitude of movement, are elements exhibiting strong positive Coulomb stresses, at least 2 bars. This is sufficient to form favourable failure conditions (King et al. 1995). This zone of elevated static stress would help fluid overpressure to overcome frictional resistance.

The results from these models suggest that fault-valve behaviour at Obuasi could have migrated laterally along the fault system, with fluid flux and therefore gold emplacement occurring in in small bursts in different sections. With a series of discrete fault-valve cycles occurring in different locations the extent of the deposit becomes mineralised over time. This is consistent with the distribution of gold along the entire extent of the deposit (Oliver et al. 2020) and the relatively brief, intense periods of cyclical fluid flux interpreted to have formed the sulphide-hosted phase of the Ashanti goldfields (Oberthür et al. 1997; Oberthür et al. 1998). Repeated seismic cycles are necessary to produce the fluid flux to endow an orogenic gold field with their measured resources (Cox 1999). The locations of ore shoots and gold endowment from the fluid cycles and aftershocks are defined by deposit-scale structural architecture as reviewed by Hronsky (2019). Evidence for remobilisation and redistribution during later deformational processes (e.g. Oberthur et al. 1995; Oberthür et al. 1997; Fougerouse et al. 2016) suggests that fault-valve behaviour during D2$_{Ob}$ did not determine the final locations of Au ore shoots in the deposit, but would explain the extremely large endowment.

6.5 Conclusions

Fault-valve behaviour on high angle shear-zones and faults is generally accepted as a major process for emplacement of gold in orogenic settings (Groves et al. 2019). The key stages in fault-valve behaviour are fluid-pressure build up, rupture, discharge and sealing, which resets conditions for a repeat of the cycle. The effects of pore-fluid pressure cannot be directly modelled in Coulomb 3.3. Instead, post-rupture conditions have been modelled, demonstrating that slipping Obuasi fault sections become negatively Coulomb stressed, becoming unfavourable to failure. This is interpreted to represent the discharge and sealing phase of fault-valve behaviour. Modelling slip events limited to a smaller section of the fault system, it is shown that sections of the fault system adjacent to those which slip become positively stressed, which provide zones of the fault system favourable to aftershocks or new mainshocks propagating along fault which are critical in introducing enough fluid into the rocks to create a world-class supergiant deposit.

Fault-valve behaviour was likely during $D2_{Ob}$, from observations of mineralisation style and $D2_{Ob}$ shear zone geometry, and these stress investigations corroborate the mechanism. However, ore shoot locations and predictions cannot be deduced using this method, making the modelling of fault-valve driven CST during mineralisation a poor exploration tool when compared to strike-slip systems such as $D5_{Ob}$.

Chapter 7.
Conclusions

7.1 Conclusions

Modelling suggests that fault slip events during late stage strike-slip faulting (D5$_{Ob}$) at Obuasi created regions of positive static stress which encompass the mineralised sections of the Obuasi fault system. Mineralization is most prominent across fault stepover structures, identified from fault traces and literature (Allibone et al. 2002; Oliver et al. 2020). This result is interpreted to show that repeated triggering of aftershocks in these regions of high positive CST enabled high fluid flux during D5$_{Ob}$ and controlled the distribution of new fluid input and remobilisation during this period. Gold mineralization on the D5$_{Ob}$ Ashanti Fissure is interpreted to as an input of new gold during D5$_{Ob}$.

The applicability of Coulomb 3.3 as a tool for the exploration geologist has been assessed in this thesis, as static stress modelling is recommended in literature (Micklethwaite and Cox 2004; Micklethwaite and Cox 2006) as a powerful tool for exploration and investigation of mineralising systems. In Chapter 2, it is established that in Coulomb 3.3-based literature there is a general lack of clarity regarding the model design used. This is easily rectified by including the input files used as a supplementary file. Benchmarking was achieved against results from Micklethwaite and Cox (2006) and an analysis of the limitations of Coulomb 3.3 highlights the importance of simplifying fault geometries to a justifiable extent, without underrepresenting the fault system. Because fault bends and terminations are critical in controlling the distribution of CST post-failure, these must be represented and not removed by oversimplification.

Chapter 3 investigates the different 'Kode' methods of modelling available in Coulomb 3.3. It is shown that using automatic tapered slip panels creates the most representative CST results for simple fault systems, but this is not possible for the types of complex fault systems encountered in gold resource geology such as

Obuasi, because Coulomb 3.3 cannot calculate tapered slip for multiple fault elements. In this context, modelling using Kode 100 whole fault slip in the combined-slip method (Micklethwaite and Cox 2006) is more representative than using point-sources. This contradicts the advice provided in the Coulomb 3.3 user guide (Toda et al. 2011a).

In Chapter 4, a small section of the Obuasi fault system containing the $D5_{Ob}$ only Ashanti and Insintsium Fissures is modelled using the combined slip method. The CST calculated after a strike-slip failure is positive across the stepovers where high grade mineralisation is observed (Oliver et al. 2020), which is interpreted to indicate high aftershock permeability in these regions, as established in Sibson (1987).

Chapter 5 compares static stress modelling for typical fault slips during the two major stages of gold mineralisation identified in literature (Allibone et al. 2002; Fougerouse et al. 2016; Fougerouse et al. 2017; Oliver et al. 2020). Regions of positive CST following strike-slip reactivation of $D2_{Ob}$ faults in $D5_{Ob}$ correlate well with the distribution of mineralisation at Obuasi, particularly across the stepover geometries identified from maps. This result indicates that aftershock-enhanced permeability was a controlling factor in the emplacement of gold during $D5_{Ob}$.

The importance of appropriately representing the geometry of fault systems was demonstrated again in Chapter 5. Model 1 represents an oversimplification which might be made if a geologist did not have access to enough data on subsurface fault geometries in early stage exploration and was relying on surface traces and strike-slip kinematics data. In comparison to Models 2 and 3, simplifying the dipping $D2_{Ob}$ faults reactivated during $D5_{Ob}$ to vertical geometries resulted in poorer correlation to mineralisation. Incorporating the GCS flexure into Model 3 demonstrated that down-dip geometry impacts CST at depth, but Coulomb 3.3 has limitations in modelling this.

The modelling was repeated for $D2_{Ob}$ reverse faulting. No significant correlation between positive CST and mineralization was found for this stage, indicating that static stress influenced aftershock processes did not control fluid flux during this period. Instead it is interpreted that high-angle reverse fault cycles after Sibson et al.

(1988) were the dominant process, with static stress being released on the fault plane following a seismic event enabling fault sealing and fluid recharge. Aftershocks are interpreted to have occurred in isolated distal events and on the fault itself. Although no significant correlation with mineralisation was found, there is an appreciable difference between the outputs of Model 4, in which all faults are simplified to dip at 70°, and Model 5, which is based on sections showing true dips, further demonstrating the importance of choosing appropriate Coulomb models.

Chapter 6 investigates whole fault movement (combined slip) and slip localised to one of ten fault segments for $D2_{Ob}$. The sections of the fault which experience no slip become positively Coulomb stressed and therefore more likely to fail, which suggests the possibility of multiple events occurring along the length of the Obuasi fault system, triggered by stress build up from failure elsewhere on the fault. The fault system at Obuasi contains an anomalously high gold resource, which requires numerous repeated gold fluid influx events, distributed along the length of the system, consistent with this process.

The success of correlating $D5_{Ob}$ CST to mineralisation shows that Coulomb stress transfer modelling can be regarded a useful tool for improving our understanding of a hydrothermal deposit and has potential to inform exploration targeting in strike-slip dominant seismogenic gold deposits and should be considered for other deposit types where aftershock sequences may have controlled fluid flow. Although no correlation was found between CST and resource distribution for $D2_{Ob}$, the technique still provided useful insights into the dynamics of the deposit during this stage and could potentially be applied with success to other deposits with reverse faults. Understanding the impact of aftershocks on deposit formation is clearly still applicable to modern exploration efforts, and this can be achieved using inexpensive and accessible tools.

7.2 Recommendations

A detailed comparison with the Obuasi mine resource model should be made to comprehensively compare the link between CST and resource distribution. Access to the Obuasi resource block model was planned in this work, however this was not possible due to time limitations. With input from the full block model, the three-dimensional impact of CST can be investigated, and the correlations achieved here corroborated with much greater accuracy and confidence. Use of full 3D models of fault planes at Obuasi is a further area for development. Modelling CST using complex geological fault surfaces is an emerging field in seismic hazard studies (Hughes et al. 2020). Developing this technique for application in an economic context should be a priority and could be combined with mapped 3D fault surfaces to tackle the issue of representing faults accurately in Coulomb 3.3.

For application at new deposits, detailed structural mapping of both mineralised and non-mineralised structures is essential, particularly for the construction of model fault elements and for choosing appropriate stress conditions. Therefore, for early stages of exploration, attention should be given to identifying the geometry of structures from drilling, mapping, and geophysical methods. When applying CST modelling, it is important to incorporate as much fault geometry as is available, aiming to create a representative model. Further study into the impact of representing dip changes with depth on economic deposits needs to be made.

Lastly, CST modelling should be extended along strike to other Birimian deposits of the WAC, such as Ayanfuri or Bogosu. These deposits have similarities to Obuasi and could benefit from an investigation of the stress conditions during this time. For hydrothermal mineral deposits where stepovers have been identified, investigations into CST are recommended as they are quick, inexpensive and have the potential to inform targeting efforts.

References

Abràmoff, M.D. et al. 2006. Image Processing with ImageJ. In: *Optical Imaging Techniques in Cell Biology*. CRC Press, pp. 249–258. Available at: http://www.crcnetbase.com/doi/10.1201/9781420005615.ax4.

Aki, K. and Richards, P.G. 1980. *Quantitative Seismology, Theory and Methods Volume I and Volume II*. doi: 10.1121/1.385057.

Allibone, A.H. et al. 2002. Structural Controls on Gold Mineralization at the Ashanti Deposit, Obuasi, Ghana. Goldfarb, R. J. and Nielsen, R. L. eds. *Integrated Methods for Discovery: Global Exploration in the Twenty-First Century* 9, p. 0. Available at: https://doi.org/10.5382/SP.09.04.

Amasa, S.K. 1975. Arsenic pollution at Obuasi Goldmine, town, and surrounding countryside. *Environmental Health Perspectives* Vol.12(December), pp. 131–135. doi: 10.1289/ehp.7512131.

Anderson, E.M. 1905. The dynamics of faulting. *Transactions of the Edinburgh Geological Society* . doi: 10.1144/transed.8.3.387.

AngloGold Ashanti 2020a. *Commemorating the First Gold Pour*.

AngloGold Ashanti 2020b. futureofobuasi.com.

Bie, L. and Ryder, I. 2014. Recent seismic and aseismic activity in the Ashikule stepover zone, NW Tibet. *Geophysical Journal International* 198(3), pp. 1632–1643. Available at: http://academic.oup.com/gji/article/198/3/1632/590470/Recent-seismic-and-aseismic-activity-in-the.

Blenkinsop, T. et al. 1994. Structural geology of the Ashanti gold mine. *Geologisches Jahrbuch D* D 100, pp. 131–153. Available at: http://scholar.google.com/scholar?hl=en&btnG=Search&q=intitle:Structural+Geology+of+the+Ashanti+Gold+Mine#0.

Bosl, W.J. and Nur, A. 2002. Aftershocks and pore fluid diffusion following the 1992 Landers earthquake. *Journal of Geophysical Research: Solid Earth* 107(B12), p. ESE 17-1-ESE 17-12. doi: 10.1029/2001jb000155.

Byerlee, J. 1978. Friction of rocks. *Pure and Applied Geophysics PAGEOPH* 116(4–5), pp. 615–626. doi: 10.1007/BF00876528.

Chinnery, M.A. 1963. THE STRESS CHANGES THAT ACCOMPANY STRIKE-SLIP FAULTING. *Bulletin of the Seismological Society of America* 53(5), pp. 921–932.

Cox, S.F. 1999. Deformational controls on the dynamics of fluid flow in mesothermal gold systems. *Geological Society Special Publication* 155, pp. 123–140. Available at: http://sp.lyellcollection.org/ [Accessed: 16 October 2019].

Cox, S.F. 2005. Coupling between Deformation, Fluid Pressures, and Fluid Flow in Ore-Producing Hydrothermal Systems at Depth in the Crust., pp. 39–75.

Cox, S.F. and Ruming, K. 2004. The St Ives mesothermal gold system, Western Australia - A case of golden aftershocks? *Journal of Structural Geology* 26(6–7), pp. 1109–1125. doi: 10.1016/j.jsg.2003.11.025.

Dabo, M. et al. 2016. Gold mineralization paragenesis to tectonic structures in the Birimian of the eastern Dialé-Daléma Supergroup, Kédougou-Kéniéba Inlier, Senegal, West African Craton. *International Geology Review* 58(7), pp. 807–825. Available at: http://dx.doi.org/10.1080/00206814.2015.1123121.

Daneva, M. 1996. The role of benchmarking in information system development. In: Constantopoulos, P. et al. eds. *Advanced Information Systems Engineering*. Berlin, Heidelberg: Springer Berlin Heidelberg, pp. 421–431.

Das, S. and Scholz, C.H. 1981. Off-fault aftershock clusters caused by shear stress increase? *Bulletin of the Seismological Society of America* 71(5), pp. 1669–1675. Available at: http://www.bssaonline.org/content/71/5/1669.short.

Eisenlohr, B.N. et al. 1989. Crustal-scale shear zones and their significance to Archaean gold mineralization in Western Australia. *Mineralium Deposita* 24(1), pp. 1–8. doi: 10.1007/BF00206714.

Eisenlohr, B.N. and Hirdes, W. 1992. The structural development of the early Proterozoic Birimian and tarkwaian rocks of southwest Ghana, West Africa. *Journal of African Earth Sciences* 14(3), pp. 313–325. doi: 10.1016/0899-5362(92)90035-B.

Fagereng, Å. 2013. Fault segmentation, deep rift earthquakes and crustal rheology: Insights from the 2009 Karonga sequence and seismicity in the Rukwa-Malawi rift zone. *Tectonophysics* 601, pp. 216–225. doi: 10.1016/j.tecto.2013.05.012.

Feybesse, J.L. et al. 2006. The paleoproterozoic Ghanaian province: Geodynamic model and ore controls, including regional stress modeling. *Precambrian Research* 149(3–4), pp. 149–196. doi: 10.1016/j.precamres.2006.06.003.

Fougerouse, D. et al. 2016. Gold remobilisation and formation of high grade ore shoots driven by dissolution-reprecipitation replacement and Ni substitution into auriferous arsenopyrite. *Geochimica et Cosmochimica Acta* 178, pp. 143–159. doi: 10.1016/j.gca.2016.01.040.

Fougerouse, D. et al. 2017. Evidence for two stages of mineralization in West Africa's largest gold deposit: Obuasi, Ghana. *Economic Geology* 112(1), pp. 3–22. doi: 10.2113/econgeo.112.1.3.

Freed, A.M. 2005. Earthquake Triggering by Static, Dynamic, and Postseismic Stress Transfer. *Annual Review of Earth and Planetary Sciences* 33(1), pp. 335–367. Available at: http://www.annualreviews.org/doi/10.1146/annurev.earth.33.092203.122505 [Accessed: 16 December 2019].

Gaboury, D. 2019. Parameters for the formation of orogenic gold deposits. *Applied Earth Science: Transactions of the Institute of Mining and Metallurgy* 128(3), pp. 124–133. Available at: https://doi.org/10.1080/25726838.2019.1583310.

Gebre-Mariam, M. et al. 1995. A classification scheme for epigenetic Archaean lode-gold deposits. *Mineralium Deposita* 30(5), pp. 408–410. doi: 10.1007/BF00202283.

Goldfarb, R.J. et al. 2001. Orogenic gold and geologic time: A global synthesis. *Ore Geology Reviews* 18(1–2), pp. 1–75. doi: 10.1016/S0169-1368(01)00016-6.

Goldfarb, R.J. and Groves, D.I. 2015. Orogenic gold: Common or evolving fluid and metal sources through time. *Lithos* 233, pp. 2–26. doi: 10.1016/j.lithos.2015.07.011.

Groves, D.I. 1993. The crustal continuum model for late-Archaean lode-gold deposits of the Yilgarn Block, Western Australia. *Mineralium Deposita* 28(6), pp. 366–374. doi: 10.1007/BF02431596.

Groves, D.I. et al. 1998. Orogenic gold deposits: a proposed classification in the context of their crustal distribution and relationship to other gold deposit types. *Ore Geology Reviews* 13(1–5), pp. 7–27. doi: 10.1016/S0169-1368(97)00012-7.

Groves, D.I. et al. 2016. The conjunction of factors that lead to formation of giant gold provinces and deposits in non-arc settings. *Geoscience Frontiers* 7(3), pp. 303–314. doi: 10.1016/j.gsf.2015.07.001.

Groves, D.I. et al. 2018. Structural geometry of orogenic gold deposits: Implications for exploration of world-class and giant deposits. *Geoscience Frontiers* 9(4), pp. 1163–1177. Available at: https://linkinghub.elsevier.com/retrieve/pii/S1674987118300409 [Accessed: 20 January 2020].

Groves, D.I. et al. 2019. A holistic model for the origin of orogenic gold deposits and its implications for exploration. *Mineralium Deposita* 55(2), pp. 275–292. Available at: https://doi.org/10.1007/s00126-019-00877-5 [Accessed: 10 December 2019].

Groves, D.I. and Santosh, M. 2016. The giant Jiaodong gold province: The key to a unified model for orogenic gold deposits? *Geoscience Frontiers* 7(3), pp. 409–417. doi: 10.1016/j.gsf.2015.08.002.

Gueye, M. et al. 2013. Structural control, fluid inclusions and cathodoluminescence studies of birimian gold-bearing quartz vein systems in the paleoproterozoic mako belt, southeastern Senegal. *South African Journal of Geology* 116(2), pp. 199–218. doi: 10.2113/gssajg.116.2.199.

Harris, R.A. 1998. Introduction to Special Section: Stress Triggers, Stress Shadows, and Implications for Seismic Hazard. *Journal of Geophysical Research: Solid Earth* 103(B10), pp. 24347–24358. doi: 10.1029/98jb01576.

Hodge, M. et al. 2018. The Role of Coseismic Coulomb Stress Changes in Shaping the Hard Link Between Normal Fault Segments. *Journal of Geophysical Research: Solid Earth* 123(1), pp. 797–814. Available at: http://doi.wiley.com/10.1002/2017JB014927 [Accessed: 8 December 2019].

Hronsky, J.M.A. 2019. Deposit-scale structural controls on orogenic gold deposits: an integrated, physical process–based hypothesis and practical targeting implications. *Mineralium Deposita* (1993). doi: 10.1007/s00126-019-00918-z.

Hughes, A. et al. 2020. Three-Dimensional Structure, Ground Rupture Hazards, and Static Stress Models for Complex Nonplanar Thrust Faults in the Ventura Basin, Southern California. *Journal of Geophysical Research: Solid Earth* 125(7). doi: 10.1029/2020JB019539.

Jaeger, J.C. et al. 1979. *Fundamentals of rock mechanics - Fourth edition*. doi: 10.1016/0040-1951(77)90223-2.

Junner, N.R. 1932. The geology of the Obuasi goldfield. *Memoir of Gold Coast Geological Survey* , p. 2:43pp.

Kerrich, R. and Wyman, D. 1990. Geodynamic setting of mesothermal gold deposits: an association with accretionary tectonic regimes. *Geology* 18(9), pp. 882–885. doi: 10.1130/0091-7613(1990)018<0882:GSOMGD>2.3.CO;2.

King, G.C.P. et al. 1994. Static stress changes and the triggering of earthquakes. *Bulletin - Seismological Society of America* 84(3), pp. 935–953. doi: 10.1016/0148-9062(95)94484-2.

King, G.C.P. et al. 1995. Static stress changes and the triggering of earthquakes. *International Journal of Rock Mechanics and Mining Sciences & Geomechanics Abstracts* 32(2), pp. A50–A51. Available at:

https://linkinghub.elsevier.com/retrieve/pii/0148906295944842.

Kozłowska, M. et al. 2015. Nanoseismicity and picoseismicity rate changes from static stress triggering caused by a M w 2.2 earthquake in Mponeng gold mine, South Africa. *Journal of Geophysical Research: Solid Earth* 120(1), pp. 290–307. Available at: http://doi.wiley.com/10.1002/2014JB011410.

Lin, J. and Stein, R.S. 2004. Stress triggering in thrust and subduction earthquakes and stress interaction between the southern San Andreas and nearby thrust and strike-slip faults. *Journal of Geophysical Research: Solid Earth* 109(B2). Available at: http://doi.wiley.com/10.1029/2003JB002607 [Accessed: 12 November 2019].

Manga, M. et al. 2009. Earthquake triggering of mud volcanoes. *Marine and Petroleum Geology* 26(9), pp. 1785–1798. Available at: http://dx.doi.org/10.1016/j.marpetgeo.2009.01.019.

Markwitz, V. et al. 2016. Compilation of West African mineral deposits: Spatial distribution and mineral endowment. *Precambrian Research* 274(January 2019), pp. 61–81. Available at: http://dx.doi.org/10.1016/j.precamres.2015.05.028.

McCuaig, T.C. et al. 1993. The nature and dimensions of regional and local gold-related hydrothermal alteration in tholeiitic metabasalts in the Norseman goldfields: the missing link in a crustal continuum of gold deposits? *Mineralium Deposita* 28(6), pp. 420–435. doi: 10.1007/BF02431600.

McFarlane, H.B. et al. 2019. Episodic collisional orogenesis and lower crust exhumation during the Palaeoproterozoic Eburnean Orogeny: Evidence from the Sefwi Greenstone Belt, West African Craton. *Precambrian Research* 325(March), pp. 88–110. Available at: https://doi.org/10.1016/j.precamres.2019.02.012.

Meade, B.J. 2007. Algorithms for the calculation of exact displacements, strains, and stresses for triangular dislocation elements in a uniform elastic half space. *Computers and Geosciences* . doi: 10.1016/j.cageo.2006.12.003.

Micklethwaite, S. 2008. Optimally oriented 'fault-valve' thrusts: Evidence for aftershock-related fluid pressure pulses? *Geochemistry, Geophysics, Geosystems* 9(4). doi: 10.1029/2007GC001916.

Micklethwaite, S. 2013. Fault stepovers and gold mineralisation. Available at: https://www.researchgate.net/publication/260073141_Fault_stepovers_and_gold_mineralisation [Accessed: 21 October 2019].

Micklethwaite, S. et al. 2016. Transient permeability in fault stepovers and rapid rates of orogenic gold deposit formation. In: *Crustal Permeability*., pp. 249–259. doi:

10.1002/9781119166573.ch20.

Micklethwaite, S. and Cox, S.F. 2004. Fault-segment rupture, aftershock-zone fluid flow, and mineralization. *Geology* 32(9), pp. 813–816. Available at: https://pubs.geoscienceworld.org/gsa/geology/article-pdf/32/9/813/3529165/i0091-7613-32-9-813.pdf [Accessed: 11 October 2019].

Micklethwaite, S. and Cox, S.F. 2006. Progressive fault triggering and fluid flow in aftershock domains: Examples from mineralized Archaean fault systems. *Earth and Planetary Science Letters* 250(1–2), pp. 318–330. Available at: https://linkinghub.elsevier.com/retrieve/pii/S0012821X06005589.

Mildon, Z.K. et al. 2016. Evaluating models of Coulomb stress transfer: Is variable fault geometry important? *Geophysical Research Letters* 43(24), pp. 12,407-12,414. Available at: http://doi.wiley.com/10.1002/2016GL071128 [Accessed: 16 December 2019].

Mildon, Z.K. et al. 2019. Coulomb pre-stress and fault bends are ignored yet vital factors for earthquake triggering and hazard. *Nature Communications* 10(1), pp. 1–9. Available at: http://dx.doi.org/10.1038/s41467-019-10520-6.

Nostro, C. et al. 2005. Coulomb stress changes caused by repeated normal faulting earthquakes during the 1997 Umbria-Marche (central Italy) seismic sequence. *Journal of Geophysical Research: Solid Earth* 110(5), pp. 1–19. doi: 10.1029/2004JB003386.

Nude, P.M. et al. 2016. Arsenic intensity risk assessment at AngloGold Obuasi goldmine, Ghana, West Africa: Using sorption and geotechnical factors. *West African Journal of Applied Ecology* 24(2), pp. 1–17.

Oberthur, T. et al. 1995. A review of gold mineralisation in the Ashanti Belt of Ghana and its relation to the crustal evolution of the terrane. *Communications - Geological Survey of Namibia*

Oberthür, T. et al. 1997. Mineralogical siting and distribution of gold in quartz veins and sulfide ores of the Ashanti mine and other deposits in the Ashanti belt of Ghana: Genetic implications. *Mineralium Deposita* 32(1), pp. 2–15. doi: 10.1007/s001260050068.

Oberthür, T. et al. 1998. Age constraints on gold mineralization and Paleoproterozoic crustal evolution in the Ashanti belt of southern Ghana. *Precambrian Research* 89(3–4), pp. 129–143. doi: 10.1016/s0301-9268(97)00075-2.

Okada, Y. 1992. Internal deformation due to shear and tensile faults in a half-space.

Bulletin - Seismological Society of America 82(2), pp. 1018–1040. Available at: https://pubs.geoscienceworld.org/ssa/bssa/article-pdf/82/2/1018/2707430/BSSA0820021018.pdf [Accessed: 11 October 2019].

Oliver, N. et al. 2020. The super-giant, high grade, Paleoproterozoic metasediment- and shear-vein-hosted Obuasi (Ashanti) gold deposit, Ghana, West Africa. In: *Geology of the World's Major Gold Deposits and Provinces.*, p. pp.121-140.

Orlecka-Sikora, B. 2010. The role of static stress transfer in mining induced seismic events occurrence, a case study of the Rudna mine in the Legnica-Glogow Copper District in Poland. *Geophysical Journal International* 182(2), pp. 1087–1095. doi: 10.1111/j.1365-246X.2010.04672.x.

Parsons, T. et al. 1999. Stress sensitivity of fault seismicity: A comparison between limited-offset oblique and major strike-slip faults. *Journal of Geophysical Research: Solid Earth* . doi: 10.1029/1999jb900056.

Perrouty, S. 2012. *Structural Evolution of the Gold-rich Ashanti Belt, SW Ghana*. Available at: https://tel.archives-ouvertes.fr/tel-00772832 [Accessed: 23 January 2020].

Peucat, J.J. et al. 2005. The Eglab massif in the West African Craton (Algeria), an original segment of the Eburnean orogenic belt: Petrology, geochemistry and geochronology. *Precambrian Research* 136(3–4), pp. 309–352. doi: 10.1016/j.precamres.2004.12.002.

Phillips, G.N. and Powell, R. 2010. Formation of gold deposits: A metamorphic devolatilization model. *Journal of Metamorphic Geology* 28(6), pp. 689–718. Available at: http://doi.wiley.com/10.1111/j.1525-1314.2010.00887.x [Accessed: 10 December 2019].

Pitcairn, I.K. et al. 2006. Sources of metals and fluids in orogenic gold deposits: Insights from the Otago and Alpine schists, New Zealand. *Economic Geology* 101(8), pp. 1525–1546. doi: 10.2113/gsecongeo.101.8.1525.

Potma, W. et al. 2008. Predictive targeting in Australian orogenic-gold systems at the deposit to district scale using numerical modelling. *Australian Journal of Earth Sciences* 55(1), pp. 101–122. doi: 10.1080/08120090701673328.

Rasband, W. 2015. ImageJ [Software]. *U. S. National Institutes of Health, Bethesda, Maryland, USA*

Scholz, C.H. and Lawler, T.M. 2004. Slip tapers at the tips of faults and earthquake ruptures. *Geophysical Research Letters* 31(21), pp. 1–4. doi:

10.1029/2004GL021030.

Schwartz, M.O. et al. 1992. Fluid inclusion re-equilibration and P-T-X constraints on fluid evolution in the Ashanti gold deposit, Ghana. *European Journal of Mineralogy* 4(5), pp. 1017–1034. doi: 10.1127/ejm/4/5/1017.

Sibson, R.H. 1981. Fluid Flow Accompanying Faulting: Field Evidence and Models. In: *Earthquake Prediction*. American Geophysical Union (AGU), pp. 593–603. Available at: https://agupubs.onlinelibrary.wiley.com/doi/abs/10.1029/ME004p0593.

Sibson, R.H. 1987. Earthquake rupturing as a mineralizing agent in hydrothermal systems. *Geology* 15(8), pp. 701–704. Available at: https://pubs.geoscienceworld.org/gsa/geology/article-pdf/15/8/701/3509933/i0091-7613-15-8-701.pdf [Accessed: 10 October 2019].

Sibson, R.H. et al. 1988. High-angle reverse faults, fluid-pressure cycling, and mesothermal gold-quartz deposits. *Geology* 16(6), p. 551. Available at: https://pubs.geoscienceworld.org/geology/article/16/6/551-555/190624.

Sibson, R.H. 1990. Conditions for fault-valve behaviour. (54), pp. 15–28.

Sibson, R.H. 1996. Structural permeability of fluid-driven fault-fracture meshes. *Journal of Structural Geology* 18(8), pp. 1031–1042. Available at: https://linkinghub.elsevier.com/retrieve/pii/0191814196000326 [Accessed: 20 January 2020].

Steacy, S. et al. 2005a. Introduction to special section: Stress transfer, earthquake triggering, and time-dependent seismic hazard. *Journal of Geophysical Research: Solid Earth* 110(5), pp. 1–12. doi: 10.1029/2005JB003692.

Steacy, S. et al. 2005b. Onto what planes should Coulomb stress perturbations be resolved? *Journal of Geophysical Research: Solid Earth* 110(5), pp. 1–14. doi: 10.1029/2004JB003356.

Stein, R.S. 1999. The role of stress transfer in earthquake occurrence. *Nature* 402(6762), pp. 605–609. doi: 10.1038/45144.

Stein, R.S. and Lisowski, M. 1983. The 1979 Homestead Valley earthquake sequence, California: control of aftershocks and postseismic deformation. *Journal of Geophysical Research* 88(B8), pp. 6477–6490. doi: 10.1029/JB088iB08p06477.

Toda, S. et al. 2002. Evidence from the AD 2000 Izu islands earthquake swarm that stressing rate governs seismicity. *Nature* 419(6902), pp. 58–61. doi: 10.1038/nature00997.

Toda, S. et al. 2005. Forecasting the evolution of seismicity in southern California:

Animations built on earthquake stress transfer. *Journal of Geophysical Research: Solid Earth* 110(5), pp. 1–17. Available at: http://doi.wiley.com/10.1029/2004JB003415 [Accessed: 12 November 2019].

Toda, S. et al. 2008. 12 May 2008 M = 7.9 Wenchuan, China, earthquake calculated to increase failure stress and seismicity rate on three major fault systems. *Geophysical Research Letters* 35(17), p. L17305. Available at: http://doi.wiley.com/10.1029/2008GL034903 [Accessed: 13 January 2020].

Toda, S. et al. 2011a. Coulomb 3.3: Graphic-rich deformation & stress-change software for earthquake, tectonic, and volcano research & teaching., pp. 1–65.

Toda, S. et al. 2011b. Using the 2011 Mw 9.0 off the Pacific coast of Tohoku Earthquake to test the Coulomb stress triggering hypothesis and to calculate faults brought closer to failure. *Earth, Planets and Space* 63(7), pp. 725–730. doi: 10.5047/eps.2011.05.010.

Toda, S. et al. 2012. Aftershocks halted by static stress shadows. *Nature Geoscience* 5(6), pp. 410–413. doi: 10.1038/ngeo1465.

Tomkins, A.G. 2013. On the source of orogenic gold. *Geology* 41(12), pp. 1255–1256. Available at: http://pubs.geoscienceworld.org/geology/article/41/12/1255/131116/On-the-source-of-orogenic-gold.

Torabi, A. and Berg, S.S. 2011. Scaling of fault attributes: A review. *Marine and Petroleum Geology* 28(8), pp. 1444–1460. Available at: http://dx.doi.org/10.1016/j.marpetgeo.2011.04.003.

Vearncombe, J. and Zelic, M. 2015. Structural paradigms for gold: Do they help us find and mine? *Transactions of the Institutions of Mining and Metallurgy, Section B: Applied Earth Science* 124(1), pp. 2–19. Available at: https://www.tandfonline.com/action/journalInformation?journalCode=yaes21 [Accessed: 6 November 2019].

Vidal, M. and Alric, G. 1994. The palaeoproterozoic (Birimian) of Haute-Comoé in the West African craton, Ivory Coast: a transtensional back-arc basin. *Precambrian Research* 65(1–4), pp. 207–229. doi: 10.1016/0301-9268(94)90106-6.

Vielreicher, N.M. et al. 2007. Timing of gold mineralization at Kalgoorlie, Western Australia. *Digging Deeper, Vols 1 and 2* , pp. 341–344.

Appendix I

All input files used for this thesis are available in supplementary .inp files. These can be read using MATLAB running Coulomb 3.3 and are available included with this work or directly from the author.